University of Alberta
Department of Civil &
Environmental Engineering

Structural Engineering Report No. 276

Combined Bending and Torsion of Steel I-Shaped Beams

by

Bruce G. Estabrooks

and

Gilbert Y. Grondin

January, 2008

Combined Bending and Torsion of Steel I-Shaped Beams

by

Bruce E. Estabrooks

and

Gilbert Y. Grondin

Structural Engineering Report 276

Department of Civil & Environmental Engineering
University of Alberta
Edmonton, Alberta

January, 2008

Abstract

Tests were conducted on six simply supported wide flange beams of Class 1 and 2 sections. The primary experimental variables included class of section, bending moment to torque ratio, and the inclusion or omission of a central brace. The end restraint and loading conditions were designed to simulate simply supported conditions at both end supports and a concentrated force and moment at midspan. Initial bending moment to torque ratio varied from 5:1 to 20:1.

A finite element model was developed using the finite element software ABAQUS. Although the initial linear response was predicted accurately by the finite element analysis, the ultimate capacity was underestimates.

A comparison of the test results with the design approach proposed by Driver and Kennedy (1989) indicated that this approach is potentially non-conservative and should not be used for ultimate limit state design. A design approach proposed by Pi and Trahair (1993) was found to be a suitable approach for ultimate limit states design.

Acknowledgements

This research project was funded by the Steel Structures Education Foundation and the National Research Council of Canada.

The test program was conducted in the I.F. Morrison Laboratory at the University of Alberta. The great efforts that Mr. Richard Helfrich has put in the design and erection of the test frame were invaluable to the success of the test program.

Feedbacks and comments provided by Dr. Robert Driver of the University of Alberta at the early stage of this project are acknowledged with thanks.

Table of Contents

List of Tables

List of Figures

List of Symbols

A	=	vertical displacement of bottom flange due to end rotation
B	=	horizontal displacement of bottom flange due to end rotation
b	=	flange width
b_i	=	width of i^{th} plate element
C	=	vertical displacement of top flange due to end rotation
C_w	=	warping constant
D	=	horizontal displacement of top flange due to end rotation
d	=	beam depth
E	=	modulus of elasticity
e	=	eccentricity
G	=	elastic shear modulus
h	=	distance between flange centroids
J	=	torsional constant
L	=	length, span
L_{bf}	=	final length of the LVDT cable attached to the bottom flange at the end of the specimen. Measured after the specimen has been deformed.
L_{bi}	=	initial length of the LVDT cable attached to the bottom flange at the end of the specimen. Measured prior to loading the specimen.
L_i	=	initial length of cable
L_{tf}	=	final length of the LVDT cable attached to the top flange at the end of the specimen measured after the specimen has been deformed
L_{ti}	=	initial length of the LVDT cable attached to the top flange at the end of the specimen measured prior to loading the specimen.
L_w	=	corrected distance measurement between the flange tip and LVDT
l	=	length, span
l_h	=	the shortest distance between the center of rotation at an end support to the end of the specimen
M	=	bending moment
M_{fp}	=	flange plastic moment

M_p	=	plastic bending moment
M_{px}	=	major axis plastic bending moment
M_{yz}	=	lateral-torsional buckling moment capacity
M_r	=	bending moment design capacity
P	=	point load
P_1	=	force applied by the central jack
P_2	=	force applied by the primary torque jacks
q	=	initial horizontal distance from the centroid of the cross-section to the primary torque clevis
R_{TBN}	=	is the reaction force at the bottom north flange tip
R_{TBS}	=	is the reaction force at the bottom south flange tip
R_{TFN}	=	is the reaction force at the top north flange tip
R_{TFS}	=	is the reaction force at the top south flange tip
r	=	initial vertical distance from the top flange of the specimen to the primary torque clevis
S_w	=	warping statical moment
s	=	initial vertical distance from the bottom flange of the specimen to the central clevis
T	=	torsional resistance, torque
$T_{applied}$	=	the torque applied to the specimen using the hydraulic jacks
T_p	=	plastic torque capacity
T_r	=	torsional design capacity
$T_{resisted}$	=	the torque calculated from the bearing reactions at the end supports
T_{sv}	=	St. Venant torsional resistance
T_{up}	=	uniform plastic torque
T_w	=	warping torsional resistance
T_y	=	design torsion capacity based on a first yield elastic analysis
t	=	flange thickness
t_i	=	thickness of i^{th} plate element
t_{max}	=	maximum plate thickness
W_n	=	normalized unit warping

w	=	web thickness, uniformly distributed load
X	=	is the measured lateral deflection
Y	=	vertical deflection of the beam at midspan
z	=	the distance between the outer surface of the bottom flange to the center of rotation of the knife-edge
α	=	the angle between a line extending from the center of rotation to the LVDT and a second line extending from the center of rotation to the flange tip using the undeformed end geometry of the specimen (see Figure 4.10)
β	=	the angle between a line extending from the center of rotation to the LVDT and a second line extending from the center of rotation to the flange tip using the deformed end geometry of the specimen (see Figure 4.10)
ΔL_{br}	=	change in length of the bottom flange LVDT cable due to end rotation
ΔL_{tr}	=	change in length of the top flange LVDT cable due to end rotation
$\Delta L_{meas.}$	=	measured change in length of cable
$\Delta L_{support}$	=	change in cable length due to the displacement of the vertical support
$\Delta L_{rot.}$	=	change in cable length due to end rotation
ϕ	=	angle of twist, performance factor
ϕ_{flange}	=	flange end rotation due to warping
$\phi_{tflange}$	=	end rotation of top flange due to warping
$\phi_{bflange}$	=	end rotation of bottom flange due to warping
ϕ'	=	first derivative of the angle of twist with respect to the distance along the axis of the beam
ϕ''	=	second derivative of the angle of twist with respect to the distance along the axis of the beam
ϕ'''	=	third derivative of the angle of twist with respect to the distance along the axis of the beam
γ_x	=	modification factor
γ_z	=	modification factor

λ = slenderness

λ_{ip} = in-plane bending plastic collapse load factor

λ_{tp} = torsion plastic collapse load factor

λ_{up} = uniform torsion plastic collapse load factor

λ_{wp} = warping torsion plastic collapse load factor

θ = end rotation

θ_t = angle of twist at midspan

θ_w = warping angle

σ_y = yield stress

$(\tau_{sv})_{max}$ = maximum shear stress due to uniform torsion

τ_w = warping shear stress

1. Introduction

1.1 General

I-shaped steel beams are widely used as structural elements because of their flexural efficiency about the strong axis. However, in many applications beams are eccentrically loaded and as a result experience torsional loads in combination with bending. Like all open sections, I-shaped steel beams are very inefficient at resisting torsion and the interaction effects due to torsion acting in combination with bending can significantly reduce the capacity of the beam. Many design methods have been developed to deal with combined bending and torsion, but none have been universally adopted by design standards. Presently, the Canadian code does not provide clear guidance for combined bending and torsion design and the need exists for a simple design equation.

1.2 Objectives and Scope

A finite element model was developed to analyze the behavior of I-shaped steel beams subjected to combined bending and torsion. Combined bending and torsion tests performed on six simply supported I-shaped steel beams were used to validate the finite element model. The primary objective of this research was to use the test results and finite element model to assess the validity of existing combined bending and torsion design methods.

A simple interaction equation, which conservatively predicts the capacity of the tested steel beams, is proposed to deal with the problem of combined bending and torsion. A complete parametric study, however, confirming its applicability for other slenderness ratios, loading conditions and end conditions is beyond the scope of this study and is required before this equation can be confidently used for combined bending and torsion design.

2. Literature Review

2.1 General

Both the Canadian and American Institutes of Steel Construction require that an elastic analysis be used to determine the maximum combined normal stress in beams subjected to combined bending and torsion (CSA, 2001; AISC, 2005). Clause 14.10.4 of CSA S16-01 requires that the maximum combined normal stress due to the specified loads does not exceed F_y. Section H2 of the AISC LRFD standard requires that the combined normal stress for the factored loads does not exceed $0.9F_y$. Several researchers have developed approximate methods, which facilitate the first yield design required by the codes (Lin (1977), Johnston (1982) and, Heins and Seaburg (1963)).

However, more recent studies have suggested that first yield designs based on an elastic analysis are most suitable for serviceability design. Many researchers have suggested that strength designs based on first yield are often overly conservative because they do not account for the spread of plasticity across the critical sections or the redistribution of stresses. Several inelastic design techniques have been proposed to deal with combined bending and torsion, which may be more suitable for ultimate limit states design check. These methods are also reviewed in the following. Although CSA S16-01 Clause 14.10.2 specifies that the factored resistance of a beam subjected to the combined effect of bending and torsion may be determined from bending-torque interaction diagrams, no such diagram is provided. Limit states design methods based on an inelastic analysis have yet to be adopted by the steel design standards.

2.2 Elastic Torsion Theory

The present day elastic theory of torsion is well established and has been extensively discussed by many researchers (Timoshenko and Goodier, 1970; Heins and Seaburg, 1963; Galambos, 1968; Heins, 1975; Salmon and Johnson, 1997; and Trahair and Bradford, 1991). Based on the classical approach developed by Saint-Venant in 1853 (Salmon and Johnson, 1996) this theory divides torsional resistance into two

distinct mechanisms. The two mechanisms are known as St. Venant torsion (also called pure, or uniform, torsion) and warping, or nonuniform, torsion.

St. Venant torsion induces shear stresses over the cross-section of the member. Figure 2.1 shows the shear stress distribution due to St. Venant torsion for an I-shaped section. For open cross-sections made up of thin-walled (b >> t) rectangular plates, such as the I-section, the maximum shear stress due to uniform torsion can be expressed as (Galambos, 1968):

$$\left(\tau_{sv}\right)_{max} = t_{max} G\phi' \qquad [2.1]$$

where, t_{max} is the maximum thickness of an individual plate element, G is the shear modulus of elasticity, and ϕ' is the first derivative of the angle of twist with respect to the distance along the axis of the member.

The total St.Venant torsional resistance is:

$$T_{sv} = GJ\phi' \qquad [2.2]$$

where J is the torsional constant for the cross-section, which can be approximated as:

$$J = \frac{1}{3}\sum_{i=1}^{i=n} b_i t_i^{\,3} \qquad [2.3]$$

In general, a torque applied to a member distorts originally plane sections into warped surfaces. Exceptions to the rule include solid or tubular circular sections and thin-walled sections in which all elements intersect at a point. These sections do not warp significantly under torsion (Galambos, 1968). All open cross-sections, such as the I-shape, do warp and therefore experience warping torsion. If warping is restricted, longitudinal stresses and shear stresses will be induced over the cross-section. The shear stresses resulting from restrained warping deformations provide a torsional restraining moment (Heins, 1975). This is referred to as the warping component of torsional resistance. For an I-shaped section the warping component of torsional resistance is the result of an internal couple created by the warping shears in the flanges as shown in

Figure 2.2. Figure 2.3 illustrates the longitudinal stresses induced by restrained warping for an I-shaped section.

The warping shear stress can be calculated from the following expression (Heins and Seaburg, 1963):

$$\tau_w = -ES_w\phi''' \qquad [2.4]$$

where E is the modulus of elasticity, S_w is the warping statical moment, and ϕ''' is the third derivative of the angle of twist with respect to the distance z, measured along the length of the member. The warping normal stress is calculated as:

$$\sigma_w = -EW_n\phi'' \qquad [2.5]$$

where W_n is the normalized unit warping and ϕ'' is the second derivative of the angle of twist with respect to z. The total warping torsional resistance is:

$$T_w = -EC_w\phi''' \qquad [2.6]$$

where C_w is the warping constant of the cross-section. The total torsional resistance is equal to the sum of the St. Venant and the warping components and can be expressed as:

$$T = GJ\phi' - EC_w\phi''' \qquad [2.7]$$

2.3 Steel Beams Subjected to Torsion Only

Several researchers have investigated the response of I-shaped steel beams to torsional loads. Boulton (1962) tested I-shaped beams under torsional loads and observed that the beams carried torques beyond the theoretical full plastic torque capacity of the cross-section. Farwell and Galambos (1969) tested five I-shaped specimens under torsion only loads and also observed torque capacities beyond those theoretically required to form a plastic collapse mechanism. Pi and Trahair (1993b) studied the behaviour of steel I-beams subjected to nonuniform torsion using a finite element procedure. Their

models indicated failure of the member at large twist rotations by fracture of the flanges rather than by the formation of a plastic collapse mechanism.

The increased torque resistance is due in part to the effects of strain hardening, but is primarily the result of tensile forces in the flanges caused by large angles of twist. At large rotations, the tension forces in the flanges have a component normal to the axis of the beam that resists the applied torque. This phenomenon is known as the helix effect or Wagner effect (Trahair, 1993).

Pi and Trahair (1994a) developed a method to analyze the plastic collapse of a member in torsion. In this method, the plastic collapse load factors of the member are determined independently for both uniform torsion and warping torsion. The actual plastic collapse load factor is approximated as the sum of the uniform torsion and warping torsion load factors. As given by (Pi and Trahair, 1994a):

$$\lambda_{tp} = \lambda_{up} + \lambda_{wp} \qquad [2.8]$$

The torsional strength of the member is considered to be adequate to carry the applied torque if:

$$1 \le \phi\, \lambda_{tp} \qquad [2.9]$$

where, ϕ is the performance factor for torsion design, taken as 0.9.

The uniform torsion plastic collapse load factor is dependent on the collapse mechanism. It is a function of the uniform plastic torque, T_{up}, and the applied torque, T. The uniform plastic torque for an I-section can be expressed as (Pi and Trahair, 1995a):

$$T_{up} = \tau_y \left[b\, t^2 \left(1 - \frac{t}{3b} \right) + \frac{h\, w^2}{2} + \frac{w^3}{6} \right] \qquad [2.10]$$

where, τ_y is the shear yield strength of the material, b and t are the width and thickness of the flanges, respectively, w is the web thickness, and h is the clear distance between the flanges.

For an I-section, the warping torsion plastic collapse load factor is determined from the flexural plastic collapse loads for the flanges. This load factor is a function of the flange plastic moment, M_{fp}, the distance between the flange centroids, *(d-t)*, the applied torque, *T*, and the span of the beam, *L*. The flange plastic moment for an I-section is givenby:

$$M_{fp} = \frac{\sigma_y b^2 t}{4} \qquad [2.11]$$

where σ_y is the normal stress at yield.

The equation used to determine the actual plastic collapse load factor, λ_{tp}, is not strictly correct and does not consider any interaction between uniform and warping torsion. However, Pi and Trahair (1994a) claim that any unsafe error due to the lack of interaction consideration is more than compensated for by the conservatism of ignoring the combined effects of strain hardening and Wagner stresses. They claim that comparisons with available experimental results show that this method conservatively predicts the torsional strength of I-shaped members, while avoiding the excessive conservatism of first yield designs based on an elastic analysis. This method is, however, only applicable for Class 1 sections subjected to torsion loads only. Pi and Trahair (1995b) have proposed other analysis methods to deal with Class 2 and Class 3 sections under torsional loads. For Class 2 sections, a first yield design based on an elastic analysis is proposed, while a local buckling torsion design is proposed for Class 3 sections.

2.4 Elastic Design Method for Combined Bending and Torsion

Perhaps, the most common method of dealing with combined bending and torsion is the superposition of stresses. The Bethlehem Steel Corporation (Heins and Seaburg, 1963) has published a classical design manual for combined bending and torsion. The solution of the governing differential equations presented in Section 2.2 has been presented in graphical form for various boundary and loading conditions. Torsion stresses and plane bending stresses are computed independently and can then be combined to determine the total normal and shear stresses at any point. Heins and

Seaburg (1963) proposed that the total combined stresses at the most heavily stressed point of the member be limited to the yield strength of the material in what is termed a first yield design. Similar graphical design aids have been developed by Johnston (1982) to facilitate first yield design.

Chu and Johnson (1974) considered the stability of unbraced beams subjected to combined flexure and torsion. They showed that in cases where lateral displacement and rotation are not restrained at the loading point the stresses due to warping are increased as the beam approaches its lateral-torsional buckling strength. For these cases they suggested that the warping normal stresses and minor-axis bending stresses be multiplied by an amplification factor prior to the superposition of stresses.

A flexural analogy is commonly used to approximate the torsional behaviour of an I-shaped beam. This approach converts an applied torque into a force couple as shown in Figure 2.4. The lateral load F, acting on the flanges of the beam, is equal to the applied torque divided by the distance between the flange centroids, (d-t). In the flexural analogy it is essentially assumed that the entire applied torque is resisted by the warping shear stresses. Since the additional contribution from the St. Venant component of torsional resistance is ignored, the flexural analogy overestimates the component of warping torsion and the corresponding warping stresses. Typically, in design situations where torsional stresses are considered, it is the normal compressive stress due to warping torsion that is most important (Salmon and Johnson, 1996). Overestimates of this normal stress by using the flexural analogy can result in overly conservative designs.

Lin (1977) proposed a method to improve the accuracy of the shear distribution assumed by the flexural analogy. In this approach the assumed shear distribution is multiplied by a hyperbolic function, which is dependent upon the loading and the end conditions, as well as the length and section properties of the beam. The value of the hyperbolic function for common situations has been expressed as a reduction factor, β, and tabulated. The normal stresses due to warping torsion can be calculated using the β factor. Warping normal stresses are combined with the normal bending stresses and the maximum combined stress is limited to the yield strength of the material.

The design aids developed by Heins and Seaburg (1963), Lin (1977) and Johnston (1982) assume torsional restraints are either pinned or fixed. Typical structural

connections, however, provide a level of torsional restraint that is somewhere between these two extremes. Therefore, the applicability of these aids is limited in many practical situations (Krayterman and Krayterman, 1987). Also, elastic design methods do not take into account any yielding interaction between normal and shear stresses (Pi and Trahair, 1994c). They also fail to take into account the possibility of local buckling of highly slender members. On the other hand, for Class 1 sections first yield designs will be conservative because of the significant difference between first yield and full plasticity of a cross-section (Pi and Trahair, 1994b).

2.5 Inelastic Design Methods for Combined Bending and Torsion

Hodge (1959) used a plastic analysis to develop a lower bound interaction equation for the case of combined bending and uniform torsion. He proposed that members that do not warp can resist applied bending moments and torques that lie within the circular interaction curve given by:

$$\left(\frac{M}{M_p}\right)^2 + \left(\frac{T}{T_p}\right)^2 = 1 \qquad [2.12]$$

where M and T are the applied moment and torque respectively, M_p is the full plastic moment and T_p is the full plastic torque capacity of the section, which is equal to the St. Venant plastic torque.

Boulton (1962) developed an approximate lower bound solution for I-beams torsionally fixed at both ends. Boulton's approach is also based on the assumption that the cross-section of the member can reach full plasticity. This assumption may be valid for Class 1 sections, but beams with high slenderness ratios typically fail due to either torsional or flexural-torsional buckling long before the section has reached full plasticity (Pi and Trahair, 1993a).

Dinno and Merchant (1965) extended the lower bound interaction equation developed by Hodge (1959) to the case of combined bending and nonuniform torsion.

Dinno and Merchant proposed that the warping component of torsional resistance could be accounted for by setting the term T_p in Hodge's equation to:

$$T_p = T_{up} + \frac{M_{fp}\,(d-t)}{l} \qquad [2.13]$$

where, T_{up} is the uniform torsion plastic collapse torque, *(d-t)* is the distance between flange centroids, l is the length of a cantilever beam and half the length of a beam restrained against warping at both ends, and M_{fp} is the full plastic moment of a flange given by Equation 2.11

However, Driver and Kennedy (1987) claim that the Dinno and Merchant equation fails to take into account the additional normal stresses due to warping and is invalid for I-shaped sections. Pi and Trahair (1993a) have shown that this equation overestimates the strength of slender beams.

Razzaq and Galambos (1979a) investigated the behavior of biaxially loaded beams with or without torsion and presented an elastic and inelastic analysis method. This method requires the solution of three simultaneous differential equations to predict the strength of the beam. The effects of torsion on beams subjected to several different ratios of major to minor axis bending including uniaxial bending about the major axis were investigated. Razzaq and Galambos (1979b) also performed a series of tests and their experimental results were in good agreement with the solutions obtained from the differential equations. The analysis method presented by Razzaq and Galambos (1979a) is complex and has not been adopted by design standards.

Driver and Kennedy (1987) conducted a series of tests on four cantilever beams loaded in combined flexure and torsion. An idealized fully plastic stress distribution, which approximated the experimental stress distribution, was used to develop an interaction model for Class 1 sections. The original interaction diagram was restricted to Class 1 sections, because the idealized normal stress distribution assumed that the ultimate stress could be developed at the flange tips. Driver and Kennedy (1989) later proposed interaction diagrams for Class 2 and Class 3 sections. However, the viability of these interaction diagrams has not been experimentally proven. Instability effects were not considered.

Pi and Trahair (1993a) performed a non-linear elastic-plastic analysis for combined bending, flexural torsional buckling and torsion of steel I-shaped members. A finite element procedure was used to investigate the interaction effects. It was formulated to account for the effects of large deformations, material inelasticity, and initial conditions of residual stresses and geometric imperfections. Three cases of combined bending and torsion were analyzed. In the first case, the beams were free to twist, but continuously braced along the shear center of the beam. In the second case, the beams were free to twist, but centrally braced (also at the shear center). In the third case the beams were free to twist and unbraced. All of the finite element models were subjected to an eccentrically applied vertical load at midspan. Pi and Trahair (1993a) analyzed three beams for each case, each with a different slenderness, where slenderness was defined as:

$$\lambda = \sqrt{\frac{M_{px}}{M_{yz}}} \qquad [2.14]$$

where, M_{px} is the major axis plastic bending moment and M_{yz} is the moment resistance of the member based on the lateral-torsional buckling capacity of the beam. They determined that the maximum bending moment and torque at midspan were functions of the slenderness of the beam, the ratio of the applied bending moment to the torque, and the lateral bracing. The interaction between bending and torsion is complex and it was not possible to develop a single interaction model that would produce accurate results for all load cases and restraining conditions investigated. Therefore, Pi and Trahair (1993a) proposed the following lower bound interaction equation:

$$\left(\frac{PL}{4M_r}\right)^{\gamma x} + \left(\frac{Pe}{2T_p}\right)^{\gamma z} = 1 \qquad [2.15]$$

where, P is the applied vertical load, L is the length of the beam, M_r is the bending moment design capacity, e is the eccentricity of the load, T_p is the maximum internal torque at plastic collapse, given as:

$$T_p = T_{up} + T_{wp} \qquad [2.16]$$

where, T_{up} is obtained from Equation 2.10 and T_{wp} is given as:

$$T_{wp} = \frac{2\, M_{fp}\, h}{L} \qquad [2.17]$$

and the values of γ_x and γ_z are 2.0, and 1.0, respectively, for continuously braced beams, and $\gamma_x = \gamma_z = 1.0$ for centrally braced beams.

Pi and Trahair (1997) also extended their torsion only analysis techniques to deal with the combined bending and torsion for I-shaped members. They proposed that Class 1 sections should be analyzed plastically and should satisfy the circular interaction equation given as (Trahair and Pi, 1997):

$$\lambda_{ip}^{\ 2} + \lambda_{tp}^{\ 2} \le \phi^2 \qquad [2.18]$$

where, λ_{ip} is the plastic collapse load factor for in-plane bending and λ_{tp} is the plastic collapse load factor for torsion.

For Class 2 and Class 3 sections they have proposed that an elastic analysis be performed. According to Pi and Trahair (1994b) these sections should satisfy the linear interaction equation given as:

$$\frac{M}{\phi\, M_r} + \frac{T}{\phi\, T_y} \le 1 \qquad [2.19]$$

where, M and T are the applied moment and torque, respectively, M_r is the design moment capacity, which takes into account lateral buckling, and T_y is the design torsion capacity based on a first yield elastic analysis for Class 2 sections and a local buckling analysis for Class 3 sections.

These interaction equations are based on the results of the finite element analysis performed by Pi and Trahair (1993a). It is unclear if the soundness of these equations has been verified by experimental results.

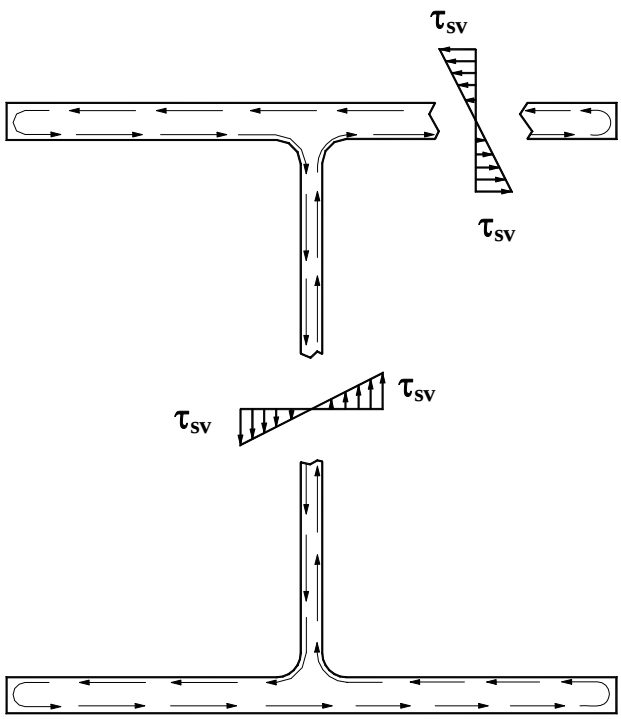

Figure 2.1 Shear stress distribution due to St. Venant torsion

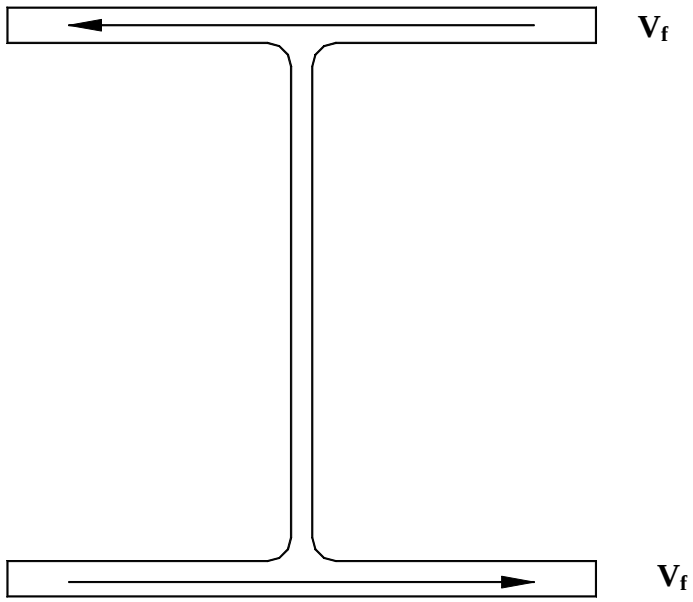

Figure 2.2 Flange shears due to warping torsion

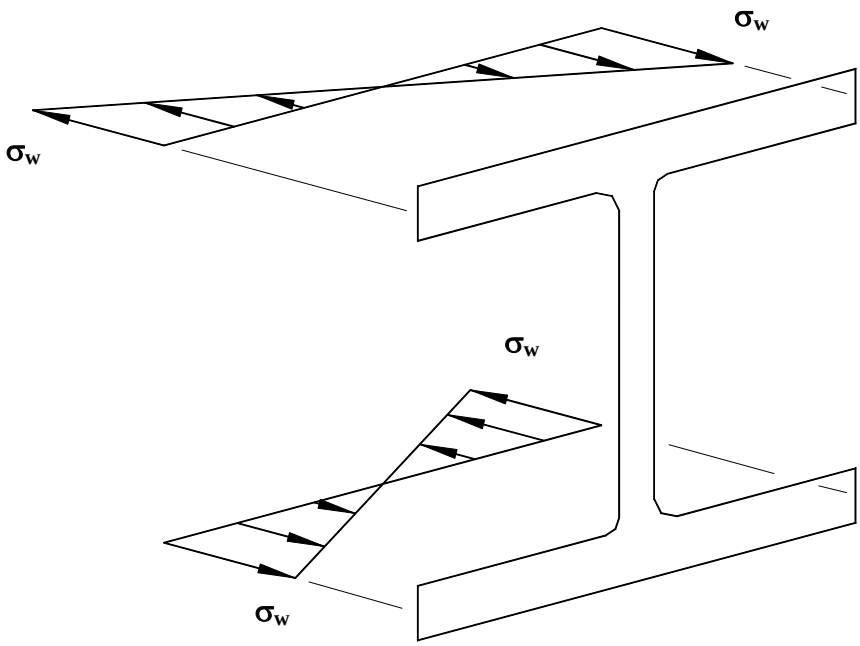

Figure 2.3 Normal stress distribution due to warping torsion

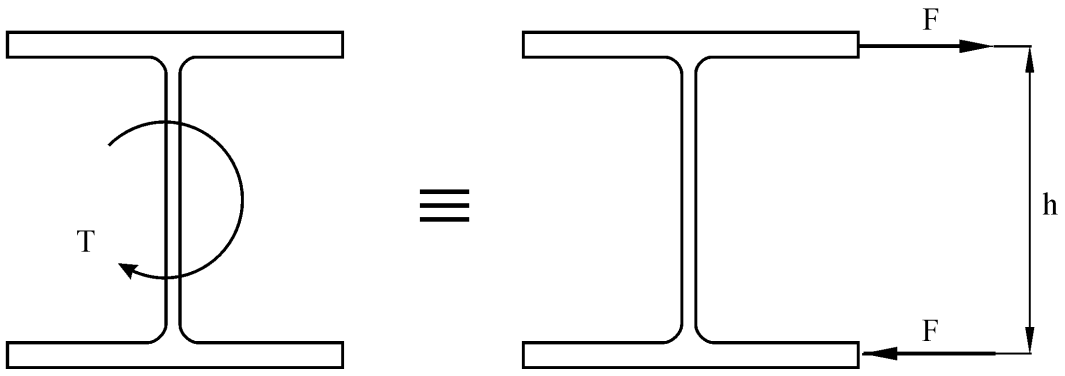

Figure 2.4 Flexural analogy

3. Experimental Program

3.1 Test Program Objectives

Limited testing has been performed on I-shaped steel beams to determine the interaction effects of combined flexural and torsional loadings. Much of the experimental work that has dealt with this loading condition has been performed on cantilever beams with the results being extended to other end conditions. The lack of published experimental data for simply supported I-shaped steel beams provided the motivation for the test program presented following.

The test program was designed to investigate the influence of a limited number of parameters on the capacity of I-shaped steel beams subjected to combined bending and torsion. The primary experimental variables included: the class of section, the ratio of bending moment to applied torque, and the inclusion or omission of a central brace. All beams were pinned in both torsion and flexure at the end supports and all loads were applied at mid-span. The experiments were conducted in the I. F. Morrison Structural Engineering Laboratory at the University of Alberta. The testing program is outlined in Table 3.1. Class 1 and Class 2 beams were tested with an initial bending moment (B.M.) to torque ratio varying from 5:1 to 20:1. All specimens had a clear span of 4.0 m and all were braced laterally at midspan except Specimen 6, which was unbraced.

3.2 Material Tests

The three Class 1 test specimens were cut from one 18 m W250X67 section. Similarly, the three Class 2 specimens were cut from one 18 m W250X73. Since all specimens were from the same source material, only three coupons were obtained from each source. In total, six tension coupons were tested in accordance with the requirements of the American Society for Testing and Materials [ASTM, 2007].

The tension tests were conducted to determine the basic material properties of the steel. The material properties were used to convert the strain gauge readings taken during

the beam tests to normal and shear stresses. The material properties were also incorporated into the finite element model.

3.3 Test Set-Up and Procedure

The desired combined bending and torsional loading in combination with a free warping restraint condition presented several challenges during the design and construction of the test set-up. Achieving solutions to these desired conditions resulted in a test set-up that contained an assortment of complex configurations of rollers, knife-edges, and bearings as evidenced from Figure 3.1 and Figure 3.2. This section will describe the various components of the test set-up that were required to model both the combined bending and torsion loading condition and the free warping end restraint condition.

3.3.1 End Conditions

In practice, it is common to approximate a bolted shear connection as a torsionally-pinned connection. For this test program, however, an end condition that more closely approximated an ideal torsionally-pinned connection was desired. To achieve this ideal end condition it is required that the flanges are free to warp while the beam is restrained from twisting. Free warping at the ends of the beam prevents the development of warping stresses, thereby eliminating the warping component of torsional resistance at the support location. As a result, testing with this ideal connection provides the lower bound capacity of the beam.

Modelling the desired torsional restraint was further complicated by the fact that a flexurally-pinned end condition was also desired. Typically, a flexurally-pinned end condition is achieved by simply providing a knife-edge to allow free bending about the strong axis and a roller to allow free translation along the length of the beam. Indeed, the vertical reactions used in this test set-up included these two devices. However, the torsional restraints now not only needed to resist twisting while allowing free warping of

the flanges, but they also had to be able to accommodate the strong axis end rotation and the beam translation along its axis required for a flexurally-pinned connection.

The end supports used to model the flexurally and torsionally-pinned end condition during the experimental program are shown in Figure 3.3 and Figure 3.4. The torsional restraint was provided by supporting two flange tips at both ends of the beam with large semi-circular rockers (part 1 in Figure 3.3) that were clamped to the flange of the beam. The rockers were aligned so that their point of rotation coincided with the beam shear center, which permitted free warping of the flanges about this point (see Figure 3.5). The circular side of the rocker rested on two rollers housed in a steel box (part 2 in Figure 3.3) to allow their rotation without translation.

A series of rollers and thrust bearings were used at the torsional restraints to accommodate the strong axis bending and along-the-beam translation. A 127-mm diameter thrust bearing (part 3 in Figure 3.3) was sandwiched between the steel roller-box (part 2 in Figure 3.3) and a 6.4-mm thick steel plate (part 4 in Figure 3.3). This thrust bearing was held in place by a bolt (part 8 in Figure 3.3) that passed through the steel plate and threaded into the backside of the steel roller-box. The head of the bolt bore against a 25.4-mm diameter thrust bearing (part 7 in Figure 3.3), which was located inside a hole drilled through a spacer plate (part 5 in Figure 3.3). The thrust bearings permitted the steel roller-box and 6.4-mm thick steel plate to swivel about the bolt.

A steel collar (part 6 in Figure 3.3) was welded to the spacer plate (part 5 in Figure 3.3) and then fitted over the head of a load cell (part 9 in Figure 3.3) used to measure the horizontal reaction force at the flange tip. The base of the load cell was attached to one side of another 6.4-mm thick steel plate (part 10 in Figure 3.3). A hardened steel plate (part 11 in Figure 3.3) was secured to the opposite face of the 6.4-mm thick steel plate (part 10 in Figure 3.3). The vertical set of rollers (part 12 in Figure 3.3) rested against the face of the hardened steel plate and was held in place by two guides (parts 13 and 14 in Figure 3.3) that were attached to the hardened plate with four set-bolts (part 15 in Figure 3.3). These bolts could be tightened to lock the rollers in place. Small aluminum strips (part 16 in Figure 3.3) were used to prevent the rollers from sliding out of the two guides during testing. Similarly, two guides containing a set of horizontal rollers were attached to a second hardened steel plate (part 19 in Figure

3.3). This plate was attached to a spacer (part 20 in Figure 3.3), which extended out from the reaction column (part 21 in Figure 3.3). A shared hardened plate (part 18 in Figure 3.3) was placed between the two sets of rollers to complete the torsion reaction.

The set of horizontal rollers was attached to the reaction column and the rocker was clamped to the specimen. The remaining components of the torsion reaction (namely, the steel roller-box, thrust bearings, load cell, and vertical roller) were suspended by a counter weight and pulley assembly (parts 27 and 22, respectively, in Figure 3.3). The counter weights provided the necessary support to the reaction components while allowing them to freely translate in the horizontal and vertical directions to accommodate end rotations and translation.

The vertical end reactions consisted of a spherical bearing (part 23 in Figure 3.3), to permit rotation about the strong and the weak axes, and a roller to allow translation along the beam axis (part 26 in Figure 3.3). A second roller was also included in the lateral direction (part 25 in Figure 3.3) to ensure that all of the lateral forces were transferred to the torsion reactions at the flange tips and that none were lost due to friction at the base. A load cell used to measure the vertical end reaction (part 24 in Figure 3.3) was also incorporated into the vertical end support.

The spherical bearings used at the vertical end reactions consisted of two hardened plates each with a small spherical recess in their centers in which a one-inch diameter ball bearing rested. The contact surfaces between the two plates and ball bearing were well lubricated and the top plate was free to rotate about all three orthogonal axes. This was necessary to accommodate the warping deformation of the bottom flange.

3.3.2 Loading of the Test Specimens

The load delivery system used during the experimental program is shown in Figure 3.6 and Figure 3.7. Three hydraulic jacks mounted in gravity load simulators delivered the loads to the specimens. The gravity load simulators ensured that the jack loads were kept vertical throughout the tests. All jacks acted in tension and had tensile capacities of 420 kN.

A loading bracket was attached to the specimen at midspan and the jacks were connected to the bracket at two locations as shown in Figure 3.6. One jack was attached to a clevis on the bottom beam of the loading bracket. This clevis was initially located in line with the shear center of the beam and the load delivered by this jack caused most of the bending moment. The other two jacks were attached to the top beam of the loading bracket using a stiff distributing beam and were used primarily to apply the torque in the beam.

All three jacks were operated from the same pump and manifold, but valves were used so that the individual jack pressures could be separately controlled. Independent jack control was necessary for two reasons: (1) to permit loading at a constant moment-to-torque ratio; and (2) to ensure that the distributing beam, used to attach two jacks to the top beam of the loading bracket, remained horizontal. As the beam rotated the center jack, which initially only caused strong-axis bending, created a resisting torque. At the same time the lever arm of the primary torque jacks decreased. This meant that, during testing, pressure would have to be released from the center jack and increased in the primary torque jacks to maintain the same moment-to-torque ratio. However, it was not possible to continuously adjust the jack pressures so that the moment-to-torque ratio was constant at every instant throughout the loading history. Rather, the jack pressures were only fine-tuned to the desired moment-to-torque ratio at the recorded data points. Therefore, although the data may indicate that the specimens were loaded at a constant moment-to-torque ratio, this was only approximately obtainable.

3.3.3 Lateral Bracing System

In practice, the function of bracing on a beam subjected to torsion is to limit the beam's ability to twist. This experimental program was, however, investigating the torsional resistance of an I-shaped steel beam and, therefore, a different type of bracing was required. The objective of the bracing was to prevent lateral deflections while allowing the torsional rotation and vertical deflection of the beam at the loading point. Lateral-torsional buckling of beams under combined bending and torsion was not the main focus of the test program. The capacity of an unbraced beam subjected to combined

bending and torsion is, however, of practical interest and this case was also investigated during the testing program.

In order to permit free torsional rotation, the beam was braced at its shear center. At the midspan of each test specimen a rectangular section 152.4 mm high by 101.6 mm wide was cut out of the web to attach the lateral support. A steel plate and pin assembly as shown in Figure 3.8 was used to reinforce the web at the cutout and attach the lateral support to the beam.

The geometry of the brace-to-pin connection was designed to maximize the amount of torsional rotation the system could accommodate. This connection was constructed from two identical parts that passed through the hole in the web and were bolted together around the high strength pin as shown Figure 3.8. The system was designed so that the flange closest to the brace-to-pin connection would rotate away from the connection during testing (see Figure 3.9). In this way, the bracing would not interfere with the rotation of the beam until the flange furthest from the connection had rotated to a point of contact with the brace, namely, approximately 45°. The bracing itself consisted of four tension rods that attached to the brace-to-pin connection (see Figures 3.8 and 3.9). The bracing system was designed so that, as the specimen rotated, the loading bracket could pass between the tension braces.

The lateral bracing reaction frame shown in Figure 3.10 prevented midspan lateral deflections. The far ends of the braces were secured to gliders mounted to the column of the lateral brace reaction frame. Counter-weights were used to pick up the weight of the gliders so that the far end of the brace was free to move vertically to accommodate the beam's vertical deflection. As shown in Figure 3.11, the gliders consisted of six 76.2-mm diameter rollers located inside a steel jacket (the glider box). The rollers were free to roll against a channel-shaped track, which was bolted to the lateral brace reaction frame. The four tension braces were equally pre-tensioned before the start of each test and throughout the test the position of the gliders was adjusted to keep the tension braces horizontal.

3.4 Instrumentation and Data Acquisition

Electrical resistance strain gauges were used to measure strains at the locations shown in Figure 3.12. Longitudinal strains on both flanges and web were measured with linear gauges, which had a gauge length of 5-mm. Strain rosettes with a 2-mm gauge length were used to measure strains at 0, 45, and 90 degrees from the longitudinal axis.

Warping deformation at the beam's ends was measured using linear variable displacement transformers (LVDTs). Five LVDTs were located at each end of the beam. Four LVDTs were used to monitor the warping deflections of each flange tip of the specimen and the fifth LVDT was used to measure the horizontal displacement of the vertical support. The LVDTs in combination with the measured end rotations were used to determine the warping angle at the ends of the specimen. Figure 3.13 shows the location of the LVDTs at the end of the beam.

The vertical deflection at midspan was measured with two cable transducers. The cable transducers were mounted to the lateral brace reaction frame directly over the midspan of the specimens and initially the two cables were attached to the loading bracket (see Figure 3.14). These measurements had to be corrected for the effect of beam twisting and for small lateral displacements between the beam and reaction frame. For the fifth test the cable transducers were moved to the lateral brace to eliminate the need to correct the readings for the effect of twist in the beam. The location of the cable transducers for Test 5 is shown in Figure 3.15.

Although the specimen was braced against out-of-plane deflections, the lateral brace reaction frame was not infinitely rigid and small out-of-plane deflections were observed. The sway of the lateral restraint frame was measured with a cable transducer mounted to a fixed column outside the test set-up. A second cable transducer mounted to another fixed point outside the test set-up with the cable attached to the lateral brace provided direct lateral displacement measurements of the specimen for tests 4 and 5. The out-of-plane deflections, in combination with the measured strain in the brace, were used to calculate a spring stiffness for the lateral restraint, which will be used in the finite element analysis of the test specimens.

During the tests, electronic clinometers were used to monitor the end rotations of the beams as well as the midspan twist. The clinometers at the ends of the beam were mounted to the center of the specimen's web. The midspan twist was measured with two clinometers mounted to the loading bracket. One clinometer was mounted to the web of the top beam of the loading bracket, while the second was mounted to the web of the loading bracket's bottom beam. The two clinometers at midspan provided one level of redundancy for the twist measurement. The locations of the clinometers are shown in Figure 3.14 and Figure 3.15.

Several load cells were used to monitor the applied loads and all reaction forces during the tests. The applied vertical load from the center jack was measured with a 445 kN load cell located between the clevis and the jack. A 220 kN load cell mounted between the torque arm and distributing beam was used to measure the load applied by the two torque jacks. The vertical reaction forces were monitored with 445 kN load cells at each support location. The vertical loads applied during the tests were considerably less than the capacity of the load cells. It was therefore necessary to recalibrate the load cells for the range of loading to be used during the test.

Four 90 kN load cells were integrated with the torsion reactions described in Section 3.3.1 to measure these lateral forces. The lateral force in the bracing system was monitored with strain gauges attached to the tension rods. The strains in the tension rods were then monitored during the tests and converted to a lateral load using a pre-determined calibration factor. The longitudinal strains in the tension rods did not exceed the elastic limit during any of the tests.

A Fluke 2400 data acquisition system was used to supply a 10-volt pulse to the strain gauges. The Fluke also powered the cable transducers and load cells with pulses of 20 and 10 volts, respectively. A 25V power supply provided an excitation of 12 volts to the clinometers and a 10V power supply provided an excitation voltage of 6 volts to the LVDTs. All electronic data were recorded using the Fluke 2400. A total of 71 data acquisition channels were used: 41 to monitor strain gauges, 12 for the load cells, 10 for the LVDTs, 4 for the cable transducers, and 4 for the clinometer measurements. Three additional channels were used to calculate the applied moment, torque, and moment-to-

torque ratio during the tests. Data were recorded at regular intervals with sufficient frequency to provide an adequate record of the specimen's behaviour.

Table 3.1 Test program

Specimen	Beam Size	Class	Initial B.M./Torque	Span	Braced/Unbraced
1	W250X67	1	5:1	4 m	Braced
2	W250X67	1	10:1	4 m	Braced
3	W250X67	1	20:1	4 m	Braced
4	W250X73	2	5:1	4 m	Braced
5	W250X73	2	10:1	4 m	Braced
6	W250X73	2	10:1	4 m	Unbraced

Figure 3.1 Test set-up

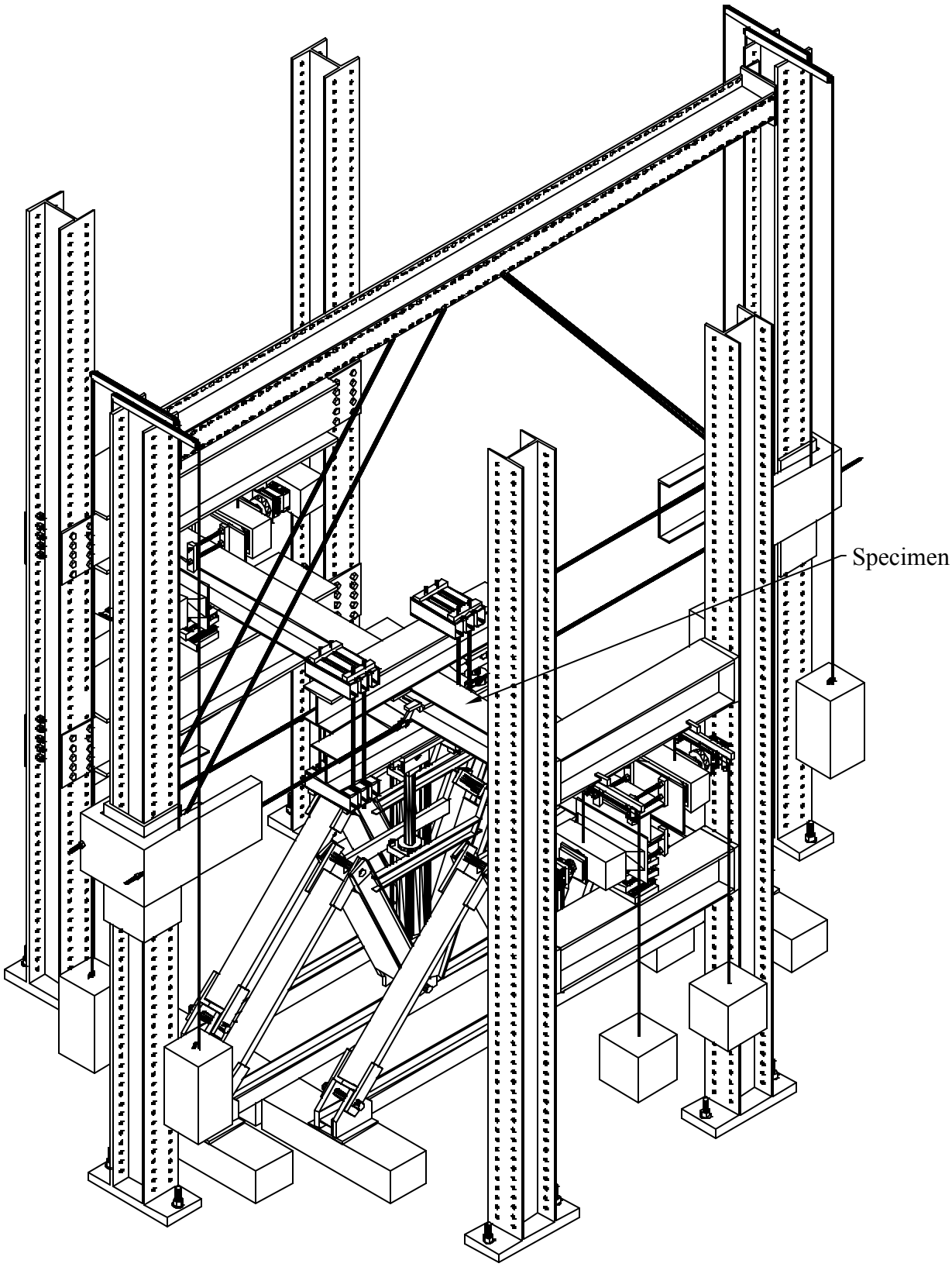

Figure 3.2 Isometric view of test set-up

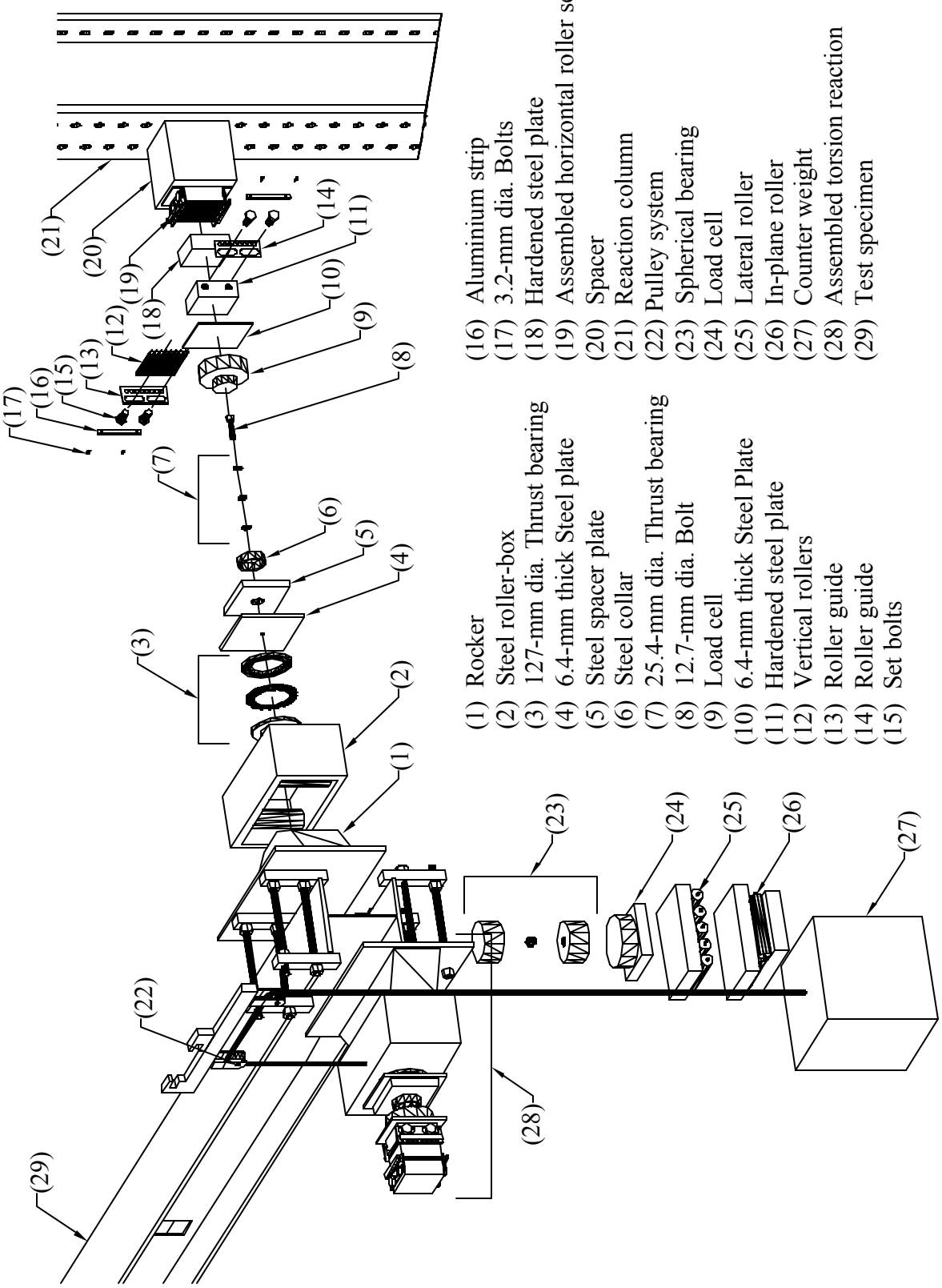

Figure 3.3 End support components

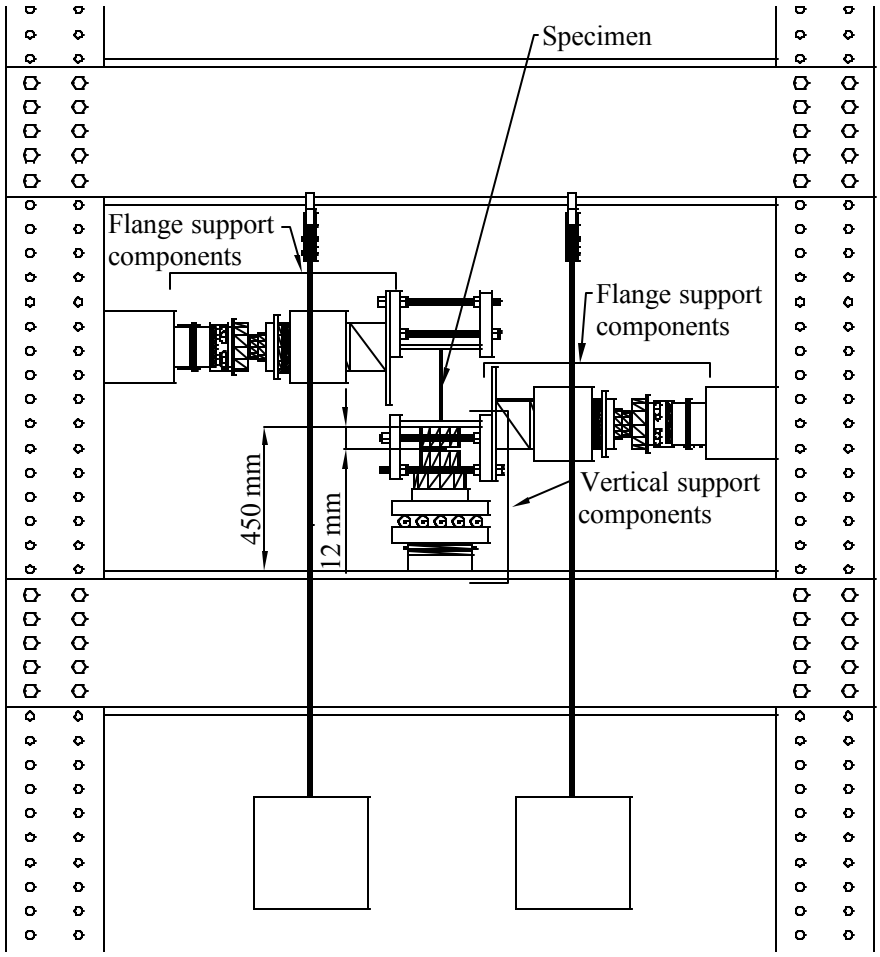

Figure 3.4 Elevation view of end support

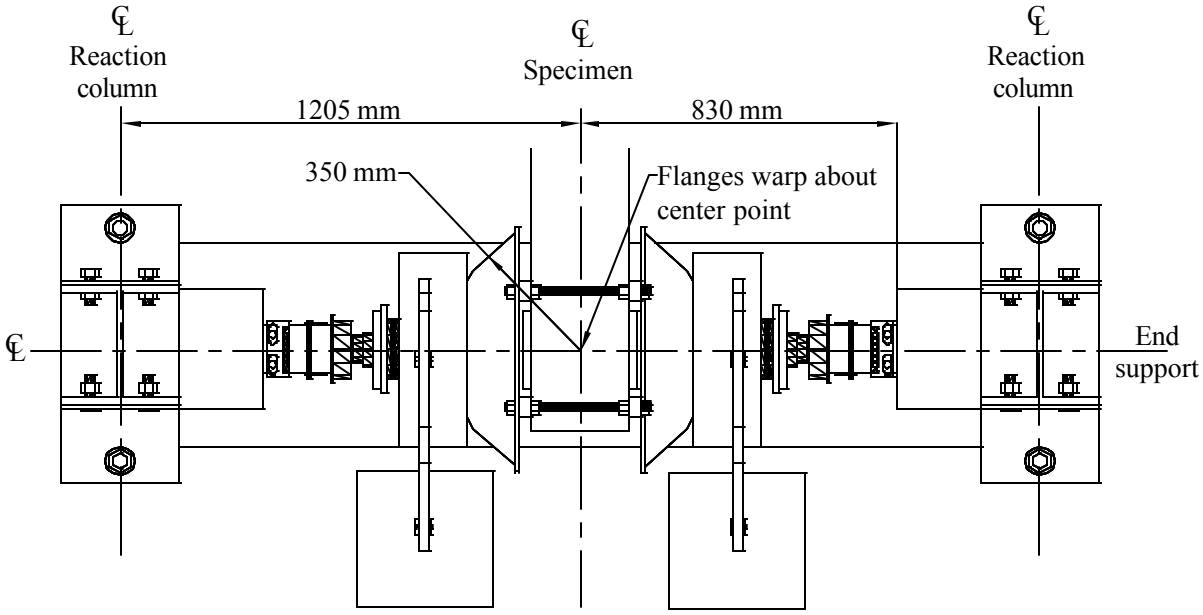

Figure 3.5 Plan view of end support

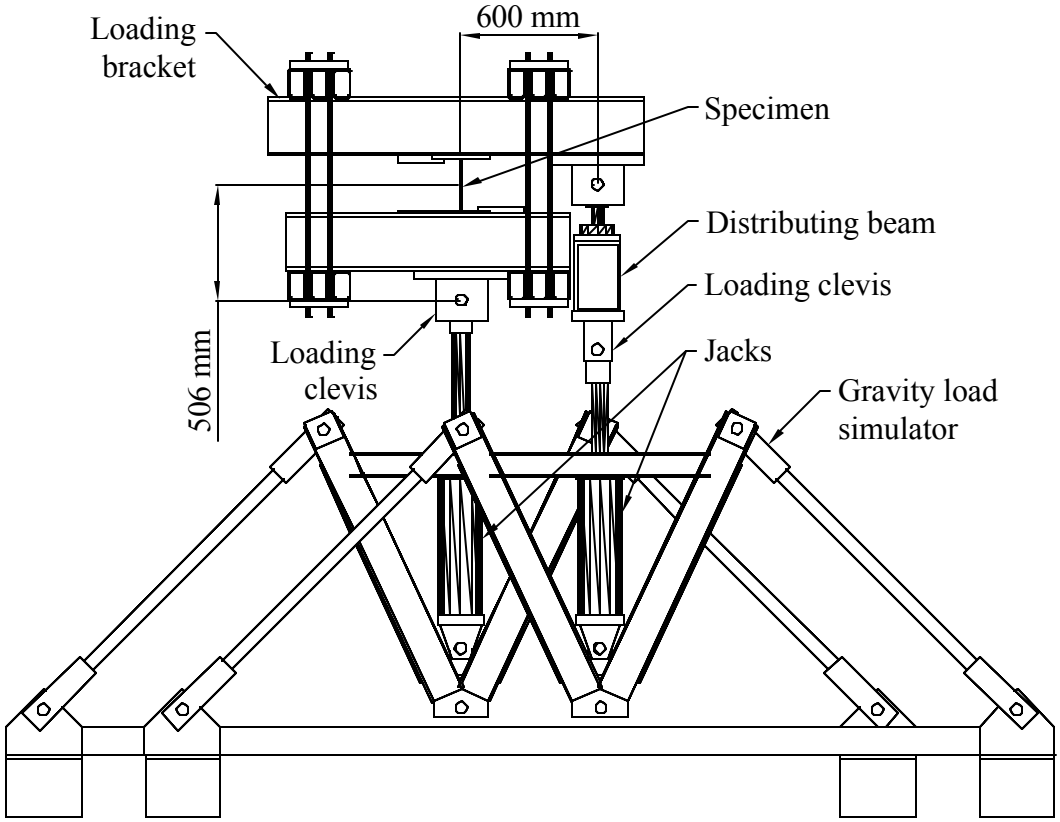

Figure 3.6 Elevation view of loading system

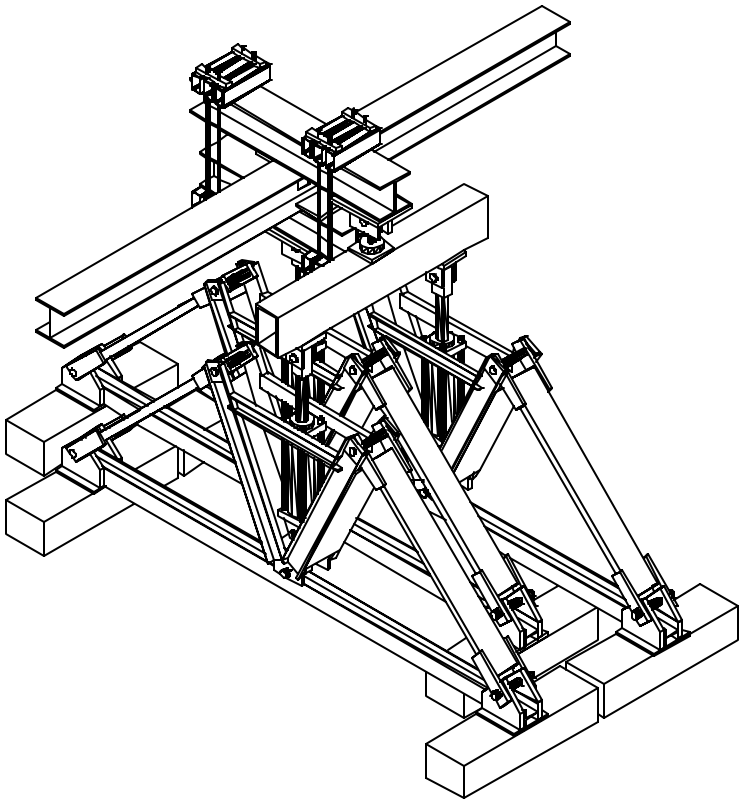

Figure 3.7 Isometric view of loading system

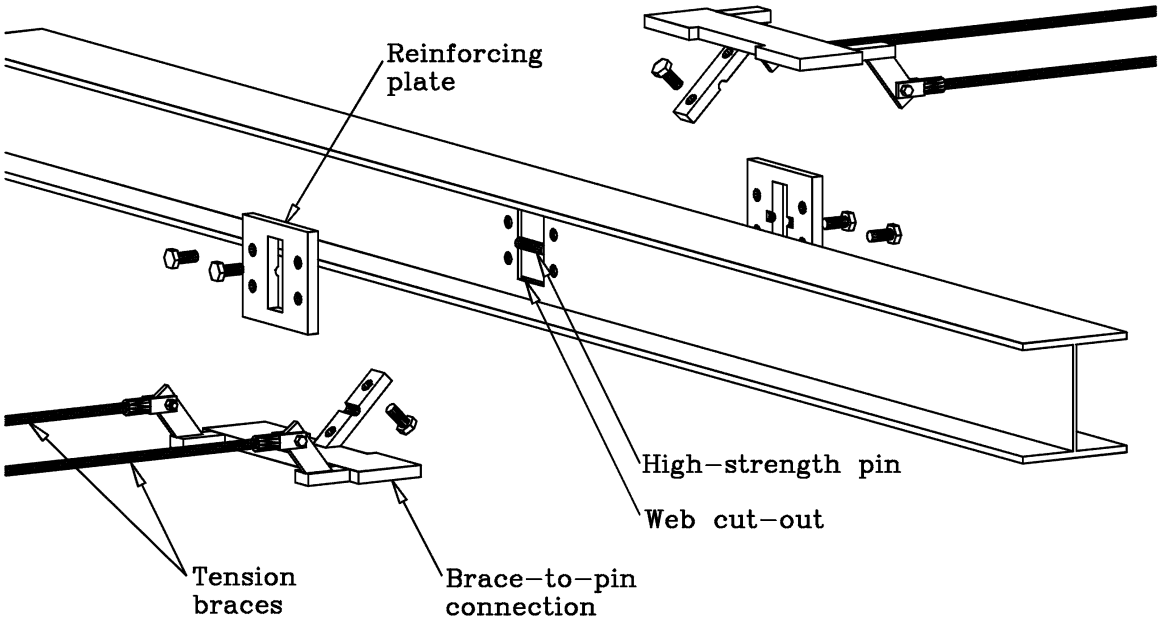

Figure 3.8 Brace-to-pin connection assembly

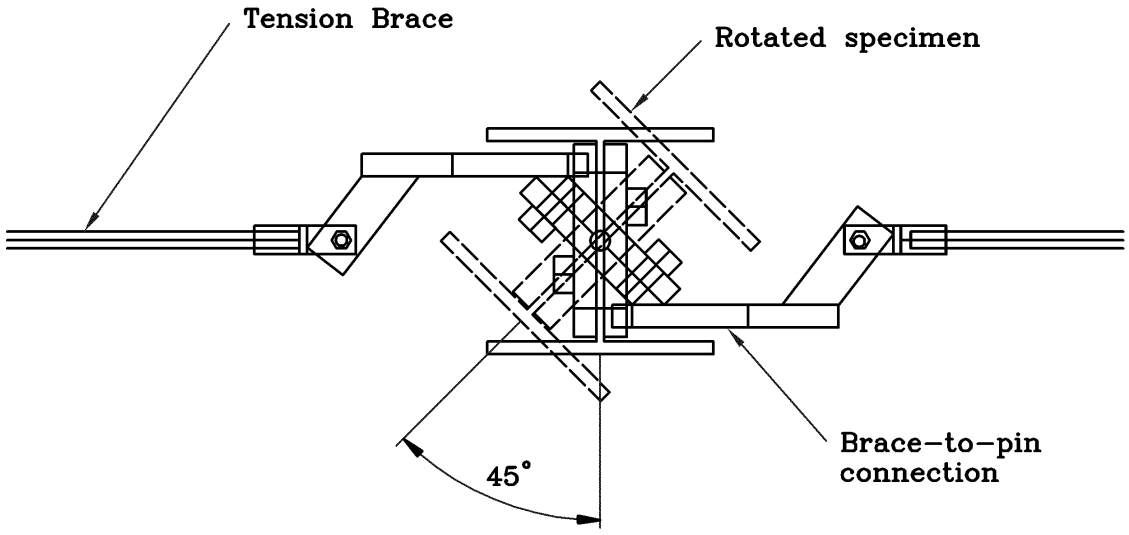

Figure 3.9 Rotation capacity of brace-to-pin connection

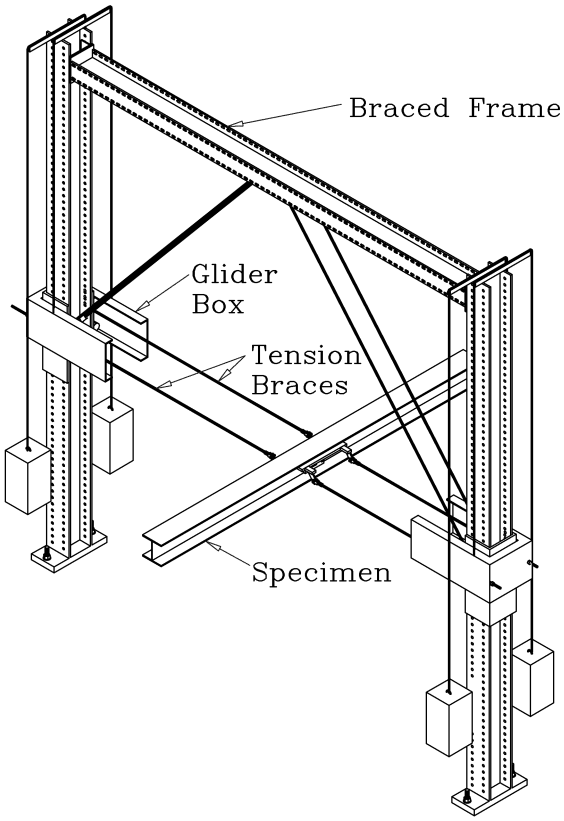

Figure 3.10 Lateral bracing frame

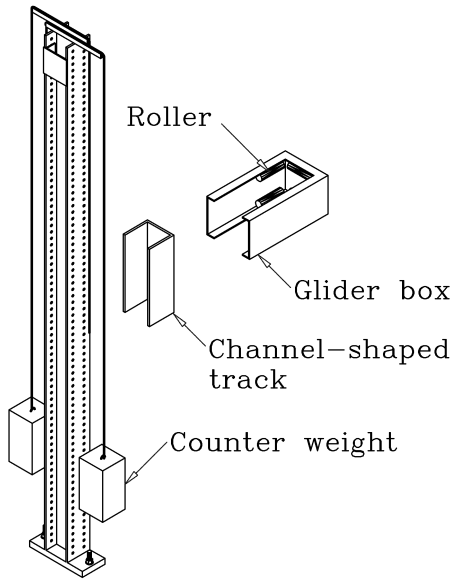

Figure 3.11 Glider box assembly detail

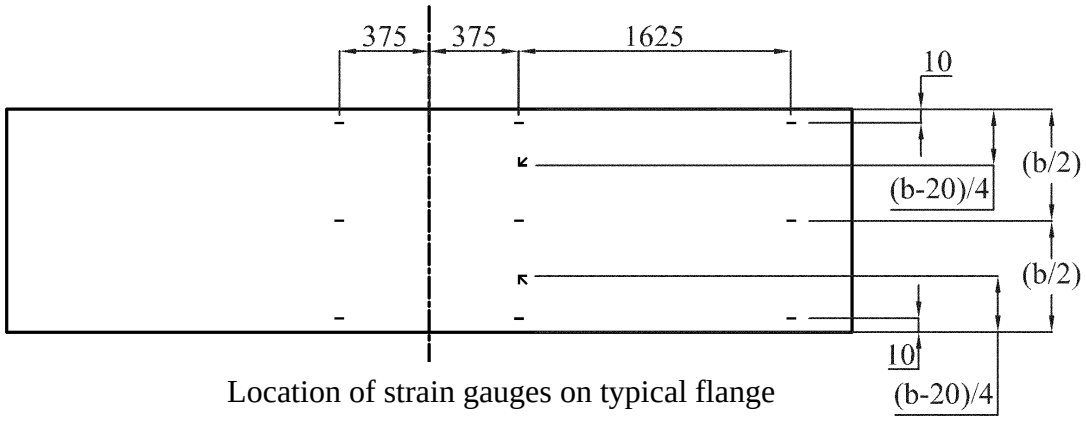

Location of strain gauges on typical flange

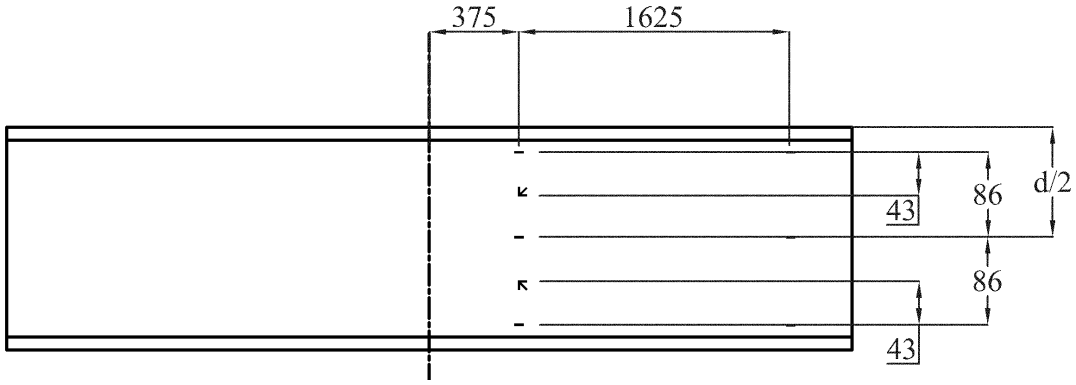

Location of strain gauges on typical web

Figure 3.12 Strain gauge and rosette locations

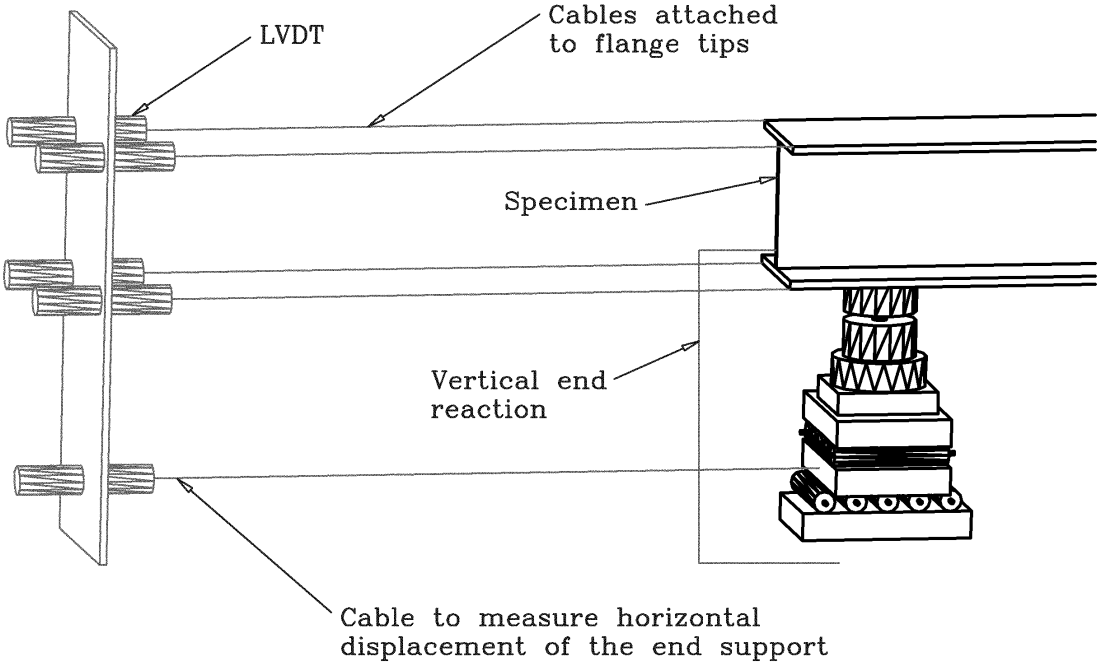

Figure 3.13 LVDTs measuring warping deformations at beam ends

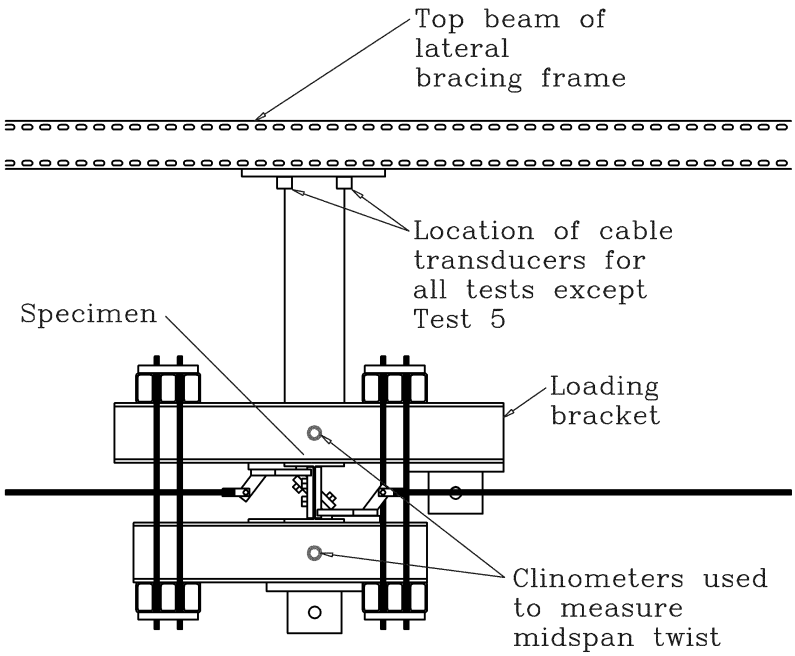

Figure 3.14 Location of instrumentation at midspan of specimen

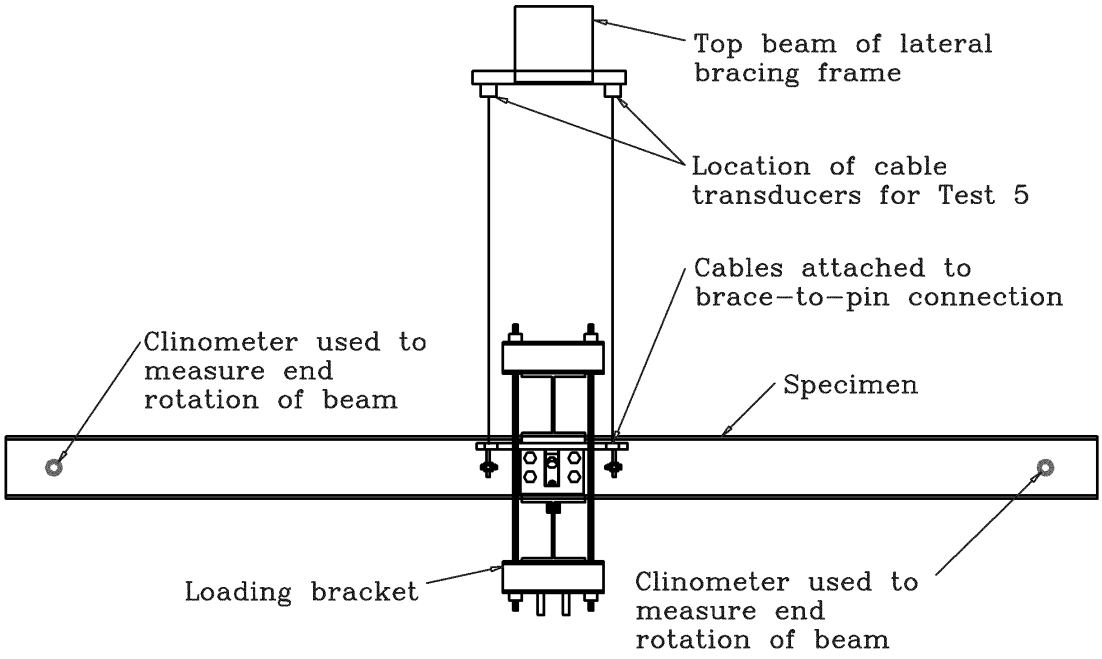

Figure 3.15 Side elevation of specimen showing location of instrumentation

4. Experimental Results

4.1 General

Quasi-static tests were performed on six I-shaped steel beams as outlined in Chapter 3. This chapter reports the collected numerical data and the observations made during the tests. The problems encountered during testing and the necessary refinements made to the testing procedure to overcome these obstacles are also discussed.

4.2 Material Properties

Table 4.1 presents the material properties obtained from tension coupons cut from the six specimens. Since all the test specimens for the same Class of section were obtained from the same section length, one coupon from the top flange of each specimen, for a total of three coupons for each section, was tested. The mean values of elastic modulus, static yield stress and static ultimate stress are listed for both sections in the table. Appendix A shows the material properties obtained from individual coupon tests.

4.3 Pre-Test Measurements

The cross-sectional dimensions of all six specimens were measured prior to testing. Cross-sections were measured at four locations along the length of the beam and multiple measurements of flange thickness (t), web thickness (w), depth (d and d_1), width (b) and fillet radius (R and R_1) were taken at each location (see Figure 4.1). The average cross-sectional dimensions for each specimen are listed in Table 4.2. The complete cross-sectional measurements of each specimen are contained in Appendix B.

The measured dimensions were used to calculate the cross-sectional properties of the tested specimens. The average cross-sectional properties for the Class 1 and Class 2 sections are listed in Table 4.3. The cross-sectional properties of each specimen are given in Appendix B.

4.4 Test Data and Observations

The information collected during the testing program is presented in this section. The discussion of the experimental results is presented in Chapter 6.

4.4.1 Vertical Deflection Measurements

Cable transducers were used to measure the vertical deflection of the beams at midspan. For tests 1, 2, 3, 4 and 6, the cable transducers used to measure vertical deflection were attached to the top of the loading bracket as shown in Figure 3.14. For these tests, the cable transducer readings had to be corrected for midspan twist and lateral deflections. The effects of midspan twist on the vertical deflection measurements are illustrated in Figure 4.2, while Figure 4.3 illustrates the influence of lateral deflections. For the fifth test the cable transducers were moved from the top of the loading bracket to the lateral brace (see Figure 3.15). This eliminated the effects of midspan twist and for this test the flange tip measurements only had to be corrected for lateral deflections. Referring to Figure 4.2:

$$A = (d/2 + 255) - (d/2 + 255)\cdot\cos\theta + (b/2\cdot\sin\theta) \quad [4.1]$$

$$B = (b/2\cdot\cos\theta) + (d/2 + 255\cdot\sin\theta) - (b/2) \quad [4.2]$$

$$C = (b/2\cdot\cos\theta) - (d/2 + 255) - (d/2 + 255)\cdot\cos\theta \quad [4.3]$$

$$D = (b/2) - (b/2\cdot\cos\theta) - (d/2 + 255)\cdot\sin\theta \quad [4.4]$$

$$L_{eft} = \sqrt{(L_{ei} + A)^2 + (B)^2} \quad [4.5]$$

$$L_{wft} = \sqrt{(L_{wi} + C)^2 + (D)^2} \quad [4.6]$$

$$\Delta L_{et} = L_{eft} - L_{ei} \quad [4.7]$$

$$\Delta L_{wt} = L_{wft} - L_{wi} \quad [4.8]$$

where, b and d are the flange width and depth of the tested specimen, respectively,

L_{ei} and L_{wi} are the initial lengths of the east and west cables, respectively,

L_{eft} and L_{wft} are the final lengths of the east and west cables after twist,

and ΔL_{et} and ΔL_{wt} are the change in length of east and west cables due to twist.

Referring to Figure 4.3:

$$L_{efo} = \sqrt{L_{ei}^{\,2} + X^{2}} \qquad [4.9]$$

$$L_{wfo} = \sqrt{L_{wi}^{\,2} + X^{2}} \qquad [4.10]$$

$$\Delta L_{eo} = L_{ef} - L_{ei} \qquad [4.11]$$

$$\Delta L_{wo} = L_{wfo} - L_{wio} \qquad [4.12]$$

where, X is the measured out-of-plane displacement,

L_{ei} and L_{wi} are the initial lengths of the east and west cables, respectively,

L_{efo} and L_{wfo} are the final lengths of the east and west cables after lateral displacement,

and ΔL_{eo} and ΔL_{wo} are the change in length of east and west cables due to lateral displacement.

The initial length of the cables was required in order to make the corrections and was measured with a tape measure to within ± 1 mm. The moment versus vertical deflection relationships for the Class 1 sections (tests 1, 2, and 3) are plotted in Figure 4.4, while Figure 4.5 shows the moment versus deflection relationships for the Class 2 sections (tests 4, 5, and 6).

Figure 4.4 shows an initially linear relationship between the applied bending moment and vertical deflection for the Class 1 sections. A short transition zone leading to a plateau, where large deflections occur with no additional increase in moment, follows the linear portion of the moment-deflection curve. However, for each specimen the plateau is reached before the full plastic moment of the cross-section is developed. As should be expected, Specimen 3, which was subjected to the largest bending moment-to-torque ratio, is able to carry the largest moment, while Specimen 1, which was subjected to the smallest bending moment-to-torque ratio, carries the smallest moment of the three test specimens. The moment-to-torque ratios for the Class 1 and Class 2 specimens are shown in Figure 4.16 and Figure 4.17, respectively. (Since the primary torque actuators ran out of stroke before any reduction in the moment carrying capacity of the beams was observed and it is not known if any further increase in strength due to

strain hardening or the Wagner effect would have occurred, excessive deflection was used as the failure criteria).

Figure 4.5 shows that the vertical deflection measurement is quite erratic during tests 4. The variability in vertical deflection measurements for Test 4 is more pronounced at small deflections (1-2 mm). At these small deflections the effects of misaligned cable transducer wires on the vertical deflection measurements would be more visible and this may be the reason for the apparent erratic vertical deflection behaviour. Figure 4.5 shows that Specimen 4, which was subjected to the smallest moment-to-torque ratio, carried the smallest moment. The increased bending moment capacity of Specimen 5 over the unbraced Specimen 6 is also shown in Figure 4.5. A comparison between Figure 4.4 and Figure 4.5 reveal that, for a given moment-to-torque ratio, the Class 1 members are able to resist a larger percentage of the plastic moment.

4.4.2 Lateral Displacement Measurements

The bracing system described in Chapter 3 provided lateral restraint to five of the six specimens with only Specimen 6 being unbraced. However, the frame that resisted the bracing forces was not infinitely rigid and even the braced specimens experienced some lateral displacement at midspan.

No direct measurements of midspan lateral displacement were taken during the tests of the Class 1 sections. However, cable transducers did record the sway of the bracing reaction frame. Since lateral forces from the test specimens caused the frame sway there was a direct relationship between the sway of the bracing reaction frame and the midspan lateral displacement of the test specimens. The sway measurements of the bracing reaction frame were multiplied by the following ratio to approximate the lateral displacement of the Class 1 test specimens.

$$\Delta_{beam} = \Delta_{sway} \frac{h_{beam}}{h_{frame}} \qquad [4.13]$$

where, Δ_{beam} is the lateral displacement of the beam at midspan,

Δ_{sway} is the measured sway at the top of the bracing reaction frame,

h_{beam} is the height of the beam above the fixed base of the bracing reaction frame, and h_{frame} is the height of the bracing reaction frame.

For the braced Class 2 tests the lateral displacement was measured using a cable transducer attached to the brace-to-pin connection located at midspan of the specimen. Since the brace-to-pin connection assembly remained horizontal while the specimen rotated around the center pin the lateral displacement measurement did not need to be corrected to account for the twist of the beam (see Figure 3.9). The relationship between the lateral displacement at midspan and the force in the tension braces is shown in Figure 4.6 for the Class 1 specimens. The same relationship is shown for the braced Class 2 specimens in Figure 4.7. The lateral displacement-to-brace force relationship shown in these figures was used to assign a spring-stiffness to the lateral restraint provided in the finite element analysis as discussed in Chapter 5.

For the unbraced Test 6, the cable transducer was attached to a thin steel beam that was fastened to a hinge welded to the midheight of the beam as shown in Figure 4.8. Unfortunately, before the maximum torque was reached the thin steel beam buckled, preventing any further meaningful measurements of the lateral deflections for Test 6. For this test a linear extrapolation function was used to obtain the lateral deflections at load levels above the last lateral deflection reading.

4.4.3 Warping at End Supports

The warping angle at the ends of the specimens was obtained from measurements taken by five LVDTs. Four LVDTs were used to measure the displacements at the flange tips, while the remaining LVDT was used to measure the in-plane translation of the vertical reaction. The displacement measurements of each flange tip were corrected for

the translation of the support and the end rotation of the specimen. The warping angle was subsequently calculated from the corrected flange tip displacements. Figure 4.9 illustrates the influence of the end rotation on the flange tip displacements. Referring to Figure 4.9, the effects of end rotation on the flange tip displacement can be quantified using the following equations:

$$A = l_h \cdot \sin\theta - (z - z \cdot \cos\theta) \quad [4.14]$$

$$B = l_h - (l_h \cdot \cos\theta - z \cdot \sin\theta) \quad [4.15]$$

$$D = l_h - \sin\theta - (d - d \cdot \cos\theta) \quad [4.16]$$

$$C = (d \cdot \cos\theta + A) - d \quad [4.17]$$

$$L_{tf} = \sqrt{(L_{ti} + D)^2 + C^2} \quad [4.18]$$

$$L_{bf} = \sqrt{(L_{bi} + B)^2 + A^2} \quad [4.19]$$

$$\Delta L_{br} = L_{bf} - L_{bi} \quad [4.20]$$

$$\Delta L_{tr} = L_{tf} - L_{ti} \quad [4.21]$$

where, A is the vertical displacement of the bottom flange due to end rotation,

B is the horizontal displacement of the bottom flange due to end rotation,

C, is the vertical displacement of the top flange due to end rotation,

D, is the horizontal displacement of the top flange due to end rotation,

L_{ti} and L_{bi} are the initial lengths of the top and bottom cables respectively,

L_{tf} and L_{bf} are the final lengths of the top and bottom cables,

d is the depth of the beam,

l_h is the horizontal distance from the center of the support (at the knife edge) to the end of the beam,

z is the distance from the outer surface of the bottom flange to the center of the knife-edge,

θ is the end rotation of the beam,

and ΔL_{br} and ΔL_{tr} are the change in lengths of the top and bottom cables due to the end rotation.

Since the rotation of the flange due to warping is small, the displacement of the vertical support can simply be subtracted from the measured flange tip displacement to provide a reasonable correction for the in-plane translation of the beam. Finally, the corrected flange tip displacement can be expressed as:

$$L_w = \Delta L_{meas.} - \Delta L_{support} - \Delta L_{rot.} + L_i \quad [4.22]$$

where, L_w is the corrected distance from the flange tip to the LVDT,

$\Delta L_{meas.}$ is the measured change in length of the cable,

$\Delta L_{support}$ is the change in cable length due to the displacement of the vertical support,

ΔL_{rot} is change in cable length due to the end rotation,

and L_i is the initial length of the cable.

The calculation required to determine the warping angle from the corrected flange tip displacement is illustrated in Figure 4.10. Referring to Figure 4.10:

$$\alpha = \cos^{-1}\left[\frac{(L_i + l_h)^2 + \frac{b^2}{2} + l_h^{\,2} - L_i^{\,2}}{2 \times \sqrt{l_h^{\,2} + \frac{b^2}{4}} \times \sqrt{(L_i + l_h)^2 + \frac{b^2}{4}}}\right] \quad [4.23]$$

and,

$$\beta = \cos^{-1}\left[\frac{(L_i + l_h)^2 + \frac{b^2}{2} + l_h^{\,2} - L_w^{\,2}}{2 \times \sqrt{l_h^{\,2} + \frac{b^2}{4}} \times \sqrt{(L_i + l_h)^2 + \frac{b^2}{4}}}\right] \quad [4.24]$$

The flange end rotation due to warping is equal to:

$$\phi_{flange} = \beta - \alpha \quad [4.25]$$

Finally, the warping angle is equal to:

$$\theta_w = \phi_{tflange} + \phi_{bflange} \quad [4.26]$$

Plots of warping angle versus midspan twist for the Class 1 specimens are shown in Figure 4.11. Similar plots for the Class 2 specimens are shown in Figures 4.12. The expected increase in warping angle with increasing midspan twist is shown in both figures. It is worth noting that for all six specimens the top flange rotation was in the order of six to seven times the rotation of the bottom flange. For an I-shaped beam subjected to torsion only both flanges would be expected to experience the same rotation. However, the second order effect due to the in-plane flexural stresses increased out-of-plane deformations in the top flange, which was in compression, and had the opposite effect of the bottom flange, which was in tension.

Figure 4.11 shows that, for a given midspan twist, Specimen 1 warped less than the Specimens 2 and 3. This is expected since Specimen 1 was subjected to the smallest moment-to-torque ratio. Figure 4.11 also shows that the rate of change of the slope of the warping angle versus midspan twist is largest for Specimen 3, which was subjected to the largest moment-to-torque ratio.

Figure 4.12 shows a well-defined relationship between the warping angle and the midspan twist for Specimens 5 and 6. The warping angle versus midspan twist relationship, however, is not as well defined for Specimen 4. The unbraced Specimen 6 experienced more warping at a given midspan twist than the braced Specimen 5. Specimen 4, which was subjected to the smallest moment-to-torque ratio, experienced the least amount of warping in the top flange.

4.4.4 Torque

Torque is a function of force and distance and, therefore, cannot be measured directly. The measured loads applied by the three jacks in combination with the geometry of the loading bracket and the measured midspan twist are used to calculate the applied torque. The applied torque is also influenced by out-of-plane deflections. As mentioned previously, despite being braced at midspan the beams did deflect laterally. The lateral deflections became significant later in the tests, thus appreciably increasing the torque applied to the beams. Referring to Figure 4.13, the applied torque can be calculated as:

$$T_{applied} = P_2 \times \left(\frac{d}{2} \cdot \sin\theta_t + q \cdot \cos\theta_t - r \cdot \sin\theta_t \right) - P_1 \times \left(s \cdot \sin\theta_t + \frac{d}{2} \sin\theta_t \right) + (P_1 + P_2) \times X \quad [4.27]$$

where, P_1 is the force applied by the central jack,

P_2 is the sum of the force applied by the primary torque jacks,

d is the depth of the beam,

θ_t is the angle of twist at midspan,

q is the initial horizontal distance from the centroid of the cross-section to the primary torque clevis,

r is the initial vertical distance from the top flange of the specimen to the primary torque clevis,

s is the initial vertical distance from the bottom flange of the specimen to the central clevis,

and X is the measured lateral deflection at midspan.

The resisting torque can also be calculated for each test. Measurements of the lateral reaction forces at the flange tips, the forces in the lateral braces, beam depth and vertical deflection are all needed to calculate the resisting torque. The resisting torque calculation is illustrated in Figure 4.14.

$$T_{resisted} = (R_{TFN} + R_{TFS}) \times ((d - t) + Y) + (R_{BFN} + R_{BFS}) \times ((d - t) - Y) \quad [4.28]$$

where, R_{TFN} is the reaction force at the top north flange tip,

R_{TFS} is the reaction force at the top south flange tip,

R_{TBN} is the reaction force at the bottom north flange tip,

R_{TBS} is the reaction force at the bottom south flange tip,

d is the depth of the beam,

t is the average thickness of the flanges,

and Y is the vertical deflection of the beam at midspan.

The torque calculations are subject to multiple sources of error. The presence of measurement errors in the loads, lateral and vertical deflections, and midspan twist all affect the accuracy of the calculated torques. Errors in recording the initial position and overall geometry of the loading bracket also adversely affect the torque calculations. Additional sources of error include the misalignment of the reaction components and the initial out-of-straightness of the specimens. Table 4.4 presents the maximum torques applied to each specimen along with the corresponding calculated resisting torque as well as the absolute difference and percent difference between the two. It is important to note that the discrepancy between the applied and resisting torques was not constant throughout the tests. In general, the largest discrepancies occurred during the initial stages of loading and they gradually decreased as the applied loads increased.

The measured loads were used to calculate both the applied and resisting torques and any errors in these load measurements would have a directly proportional impact on the calculated torque values. Load cells were used to measure the applied vertical loads, vertical reaction forces, and bearing reactions at the flange tips. Lateral bracing forces were measured by strain gauges mounted to the tension rods. The load cells and tension braces used in the test set-up were calibrated just prior to testing and were accurate to within $\pm$ 0.5%. Therefore, any errors in the calculated torque values resulting from errors in the load measurements are expected to be in the order of $\pm$ 0.5%.

The applied vertical loads and vertical reactions were monitored during the tests to ensure that the vertical forces entering the system were fully transferred to the end supports. For all six tests, the sum of the vertical reactions was within 1 % of the total applied vertical load. This discrepancy is slightly higher than the accuracy expected from the load cells and suggests that there were some friction losses in the system.

The lateral reaction forces were also monitored during testing. Initially however, due to the difficulty integrating load cells into the torsional end restraints only one load cell was used to monitor the lateral reactions at each end. These load cells measured the bearing forces in the top flange reactions. For these tests, the bearing forces in the bottom flanges were determined from statics by summing the top flange reaction forces and the forces in the lateral braces. For Test 5 additional load cells were incorporated

into the bottom flange reactions. These load cells measured the bearing forces at the bottom flanges. The additional load cells enabled a check to see if the lateral forces did indeed satisfy statics. The lateral forces in tests 5 and 6 satisfied equilibrium to within 2.2 % and 2.5 %, respectively. This is higher than the expected 0.5% accuracy of the load cells and suggests that friction forces somewhere in the test set-up may have also resisted the applied torque. Another possibility for this higher than expected discrepancy is that the reaction forces may not have acted through the center of the load cells. Although the load cells are reasonably good at measuring slightly eccentric loads, large eccentricities would result in inaccurate measurements of the reaction forces. Great care was taken in aligning the components of the torsion reactions and every attempt was made to ensure that the flange tips were firmly seated against the torsion reaction before the start of each test. However, it is probable that some small amount of twist occurred at the supports during the initial stages of loading before the reaction components came into full bearing. This could have altered the alignment of the load cell introducing errors into both the load measurements and the torque calculations. Despite these problems the lateral load measurements were balanced to within 2.5% as mentioned and any discrepancy between the applied and resisted torques caused by eccentricities at the bearing supports and friction losses is expected to be also limited to 2.5%.

Errors in measuring the geometry of the loading bracket may also have affected the torque calculations. However, great care was taken in measuring the loading bracket geometry and these measurements proved repeatable to within 1 mm for each test. A 1 mm discrepancy translates to a 0.2% error in the length the lever arm of the loading bracket. The calculated applied torque is linearly proportional to the length of the lever arm and therefore, the direct contribution to the torque discrepancies from errors in the loading bracket geometry would be expected to be in the order of 0.2%.

The midspan twist was measured by two clinometers in each test to provide one level of redundancy. The measurements from the two clinometers were within 3% for all tests. At the maximum permitted rotation of 45° a 3% error in rotation equates to a discrepancy of 2.4% in the length of the horizontal lever arm used to calculate the applied torque. The discrepancy in the horizontal lever arm is less at smaller rotations. At a midspan rotation of 30° the resulting error in the horizontal lever arm is less than 1%.

Therefore, errors in the midspan twist measurement have a less significant impact on the applied torque calculation at small rotations, but may result in errors of up to 2.4% at the maximum rotation permitted by the test set-up.

In the first four tests, the misalignment of the vertical reactions also adversely affected the torque calculations. For these tests, the knife-edge component of the vertical reactions was centered about the width of the bottom flange. However, it was later noted that for each specimen the center of the flange to web junction was located approximately 3 mm away from the middle of the flange. This means that the vertical reactions were acting eccentrically to the initial location of the central pin about which the beam was forced to twist. As a result, for these four tests the vertical reaction forces were contributing a resisting torque equal to the vertical force multiplied by the initial eccentricity. The initial sweep of the beam also could create an eccentricity between the vertical reactions and the initial point of twist. The initial sweep was measured for several untested specimens and all had an initial out-of-straightness of less than 1.5 mm over the full length of the specimen, 4 m. Therefore, the sweep of the beam appears to have a minimal influence of the torque calculations. However, depending on orientation it is possible for the influence of the sweep of the beam to be additive to the influence of the misalignment of the vertical reactions. An eccentricity of 4.5 mm between the center pin and the center of the vertical support could result in a discrepancy of ± 2% between the applied and resisted torque.

The out-of-plane displacements measurements are perhaps the measurement with the lowest level of certainty and are potentially the largest contributor to the discrepancies between the calculated applied and resisting torques. As mentioned previously, although only Specimen 6 was unbraced the bracing reaction frame was not infinitely rigid and all specimens experienced out-of-plane displacements at midspan. For the Class1 specimens the lateral displacement of the beam at midspan was not measured directly and had to be extrapolated from the sway measurements of the bracing frame. The extrapolated lateral displacement measurements are expected to be accurate to within ± 5%. Increasing the lateral displacement values for the Class 1 specimens by 5% results in an increase in the calculated applied torque by as much as 4%.

The midspan vertical deflection was measured by two cable transducers to

provide one level of redundancy. The measurements from the two cable transducers were in agreement to within ± 5%. The vertical deflection measurements had to be corrected to account for the midspan rotation and out-of-plane displacement of the beam. Therefore, the accuracy of the vertical deflection measurement is dependent on the accuracy of the rotation and out-of-plane displacement measurements. The errors associated with these two measurements account for much of the discrepancy between the readings of the two cable transducers. However, the torque calculation is not overly sensitive to vertical deflection and a 5% change in the vertical deflection measurement results in less than a 1% change in the calculated resisting torque.

Torque is the product of a force and distance and, therefore, the errors in the calculated torque will be the product of the errors in the force and distance measurements. As was noted above the level of accuracy in the load measurements is quite high (± 2.5% accounting for friction losses) and most of the discrepancy between the applied and resisting torque values is the result of errors in the measured rotations, deflections and initial geometry of the beam that were used to calculate the distance through which the measured force was acting. It is possible for the geometric sources of error to be additive and the maximum expected error in the calculated torque values can be approximated as the sum of the geometric sources of error multiplied by the error associated with friction losses, which could be expressed as:

$$E_{torque\max} = 1 - \left[1 + E_{friction}\right] \times \left[1 + E_{bracket} + E_{rotation} + E_{alignment} + E_{lateral} + E_{vertical}\right] \qquad [4.29]$$

$$E_{torque\max} = 1 - \left[1 + 0.025\right] \times \left[1 + 0.002 + 0.024 + 0.02 + 0.04 + 0.01\right]$$

$$E_{torque\max} = 0.123 = 12.3\%$$

There are two sources of error in Test 6 not present in the other tests that may account for the large discrepancy between its maximum applied torque and the corresponding resisting torque. Test 6 was unbraced and as discussed above, due to the failure of the cable transducer connection lateral deflection measurements were not recorded for the full duration of the test and a linear extrapolation function was used to estimate the lateral deflections at load levels above the last lateral deflection reading.

The applied torques calculated using the approximate lateral deflections are adversely affected by the inaccuracies of these approximations and this may account for some of the larger than expected discrepancy.

The second source of error unique to Test 6 also has to deal with the lateral deflection measurement. In all previous tests, the lateral bracing forced the specimens to rotate about the midheight of the beam. However, since Specimen 6 was unbraced the rotation would have occurred about the shear center of the specimen. However, the exact location of the shear center was impossible to determine because of local distortions caused from loading bracket at the critical section. Therefore, although the hinge attempted to eliminate any errors in the lateral deflection readings due to the midspan twist, errors still occurred because the beam was not rotating about the exact location of the hinge. For these two reasons the calculated resisting torque for Specimen 6 is probably a more accurate measure of the torque applied to the beam.

For the first test, there was a limited amount of stroke available in the primary torque jacks. The main reason for this was that the elevation of the end supports was too low. The bolthole spacing on the support columns limited the elevation of the end supports and the optimum elevation was not obtainable. Also, during the first test Specimen 1 was positioned in the reaction frame so that the bottom flange was level. The out-of-parallel of the specimen flanges was such that the top beam of the loading bracket was sloped down towards the distributing beam (see Figure 3.6). This further limited the available stroke in the primary torque jacks. As a result, the primary torque jacks in Test 1 ran out of stroke before a definite yield plateau was reached. To avoid this problem in the subsequent tests, the available stroke in the primary torque jacks was maximized. This was accomplished through the initial positioning of the specimens in the reaction frames. First, the specimens were set on the vertical reactions and the distributing beam was attached to the clevis on the top beam of the loading bracket. The primary torque jacks were then fully extended causing the beam to twist. Since the twist was not resisted the specimens experienced a rigid body rotation about the z-axis. Once the jacks were fully extended the torsion restraints were placed into bearing. An example of the initial angled position of Specimens 2 through 6 is illustrated in Figure 4.15.

The average of the calculated applied and resisting torque is considered as the best representation of the actual torque experienced by the beams. For the remainder of this paper, therefore, the term torque refers to the average of the calculated applied torque and the calculated resisting torque.

The relationships between torque and midspan twist for the Class 1 sections are plotted in Figure 4.16, while Figure 4.17 shows the same relationship for the Class 2 sections. Figures 4.18 and 4.19 show the relationship between the bending moment and torque applied to the Class 1 and Class 2 sections, respectively. The slopes of the lines in Figures 4.18 and 4.19 represent the average ratio of bending-moment to torque for each individual test. An attempt was made to maintain this ratio reasonably constant throughout each test, but it is apparent from Figure 4.19 that this was not accomplished for Tests 5 and 6. The moment-to-torque ratio was also not well controlled during the early stage of Test 1 as shown in Figure 4.18.

Figures 4.16 and 4.17 show an initial linear relationship between the torque and the midspan twist. The linear region of the curves is followed by a gradual transition zone, in which the midspan twist begins to increase faster than the torque. The maximum torque carrying capacity of Specimen 1 and Specimen 4 was not reached before the primary torque jacks ran out of stroke. However, the a plateau started to develop for Tests 2, 5 and 6, while Test 3 actually showed a decrease in torque carrying capacity of the test specimen.

Figure 4.17 shows that Specimen 6, despite being unbraced, has as much torque carrying capacity as Specimen 5. The intention was to test these two Specimens at the same bending-moment to torque ratio in order to evaluate the influence of the central brace. However, Figure 4.19 shows that Specimen 6 was subjected to an average bending-moment to torque ratio that was approximately 7% less than that of Specimen 5. This means that for the same level of torque Specimen 6 was subjected less bending than Specimen 5. It is also worth noting that there was a large imbalance between the applied torque and the calculated resisting torque for Specimen 6 as discussed above.

4.4.5 Bending Moment

The bending moment is a function of force and distance and is dependant on the boundary conditions. For a simply supported beam subjected to a point load at midspan the maximum bending moment occurs at the location of the point load and is equal to the following:

$$M = \frac{P \times l}{4} \quad [4.30]$$

where, P is equal to the point load,

and l is equal to the span of the beam

The maximum bending moment for a simply supported beam subjected to a uniform load is also located at midspan and calculated as follows:

$$M = \frac{w \times l^2}{8} \quad [4.31]$$

where, w is equal to the uniformly distributed load,

and l is equal to the span of the beam

Therefore, the maximum bending moment for the tested specimens was calculated as follows:

$$M = \frac{(P_1 + P_2 + P_{bracket}) \times l}{4} + \frac{w_{beam} \times l^2}{8} \quad [4.32]$$

where, P_1 is the force applied by the central jacks,

P_2 is the sum of the force applied by the primary torque jacks,

$P_{bracket}$ is the weight of the loading bracket,

w_{beam} is the uniformly distributed weight of the beam,

and l is the span of the beam

4.4.6 Strain Distributions

Electrical resistance strain gauges were used to measure strains during the six tests. Since the beams were simply supported and subjected to one point loading, the location of the maximum bending moment and critical section coincided with the midspan loading point. However, the presence of the loading bracket made it impossible to mount strain gauges at this location. Instead, strain gauges were located 375 mm on

either side of the specimen centerline. This distance was to ensure that the strain readings would not be affected by the local distortions caused by the loading bracket.

Since both ends of the beams were similarly restrained and the loads were applied at midspan, it was anticipated that the strain distributions would be symmetric about midspan. For this reason, only one side of the specimen was fully gauged with a selected number of gauges mirrored about midspan to verify the assumed symmetry of the strain distributions. The exact arrangement of the strain gauges is shown in Figure 3.12.

Strain distributions for a given loading point measured during the testing of Specimen 2 and Specimen 5 at cross-sections located 375 mm on either side of midspan are plotted in Figure 4.20. These two figures are representative of the typical shape of the cross-sectional strain distribution for the tested I-shaped steel beams prior to local buckling of the top flange. The three points of zero strain present in the cross-section, one in each flange and a third near the center of the web is common to all the tested specimens. The near linear strain gradient across the flanges and through the web is also common characteristics of the tested specimens. The strong agreement between the strain measurements taken on the north and south sides of midspan shown in Figure 4.20 is consistent with the strain readings taken during the other tests.

Electrical resistance strain gauges were also attached to each specimen at the location of one of the end supports to measure any normal strains and to provide an indication as to how close the end supports were to the ideal case they were attempting to model. If the end supports were successful in permitting free rotation and free warping minimal normal strains would be present in the flanges of the beam at the support location. The maximum and minimum normal strain across both the top and bottom flange at the maximum test load is shown for each specimen in Table 4.5. The variation in normal strain across the flanges of each Specimen indicates that the test set-up did not fully achieve the desired ideal end conditions.

Table 4.1 Material properties

Section/Class	Mean Modulus of Elasticity (MPa)	Mean Static Yield Strength (MPa)	Mean Static Ultimate Strength (MPa)
W250×67/Class1	205 500	297	422
W250×73/Class2	207 500	300	442

Table 4.2 Average cross-sectional dimensions

Specimen No.	Depth (mm)		Width (mm)		Flange Thickness (mm)		Fillet Radius (mm)		Web Thickness (mm)	Out-of-Parallel (mm)
	d	d_1	b	b_1	T	t_1	R	R_1	w	$\lvert d-d_1 \rvert$
1	253	256	206	204	15.4	15.6	11.5	11.2	8.6	3.6
2	253	257	205	204	15.4	15.6	11.2	11.0	8.6	4.0
3	252	257	206	204	15.4	15.7	11.2	10.8	8.6	4.6
4	255	252	257	254	13.3	13.6	10.0	11.0	9.5	3.4
5	255	252	256	255	13.3	13.6	11.5	10.5	9.5	2.6
6	254	253	258	256	13.3	13.7	11.0	12.0	9.5	1.2

* See Appendix B for detailed measurements.

Table 4.3 Average cross-sectional properties

Section Class	T_{up} (kN·m)	T_{wp} (kN·m)	M_p (kN·m)	M_y (kN·m)	M_{fp} (kN·m)	Z_x ($10^3 mm^3$)	S_x ($10^3 mm^3$)	I_x ($10^6 mm^4$)	I_y ($10^6 mm^4$)
Class 1	9.72	5.79	263	231	48.4	885	779	99.5	22.3
Class 2	9.71	7.94	289	257	66.4	964	857	106	37.8

Table 4.4 Discrepancies between applied and resisted torques

Specimen No.	Applied Torque (kN·m)	Resisted Torque (kN·m)	Absolute Difference (kN·m)	Percent Difference (%)
1	28.8	27.1	1.7	6.2
2	23.8	22.3	1.5	6.6
3	17.4	16.4	1.0	6.0
4	32.5	31.0	1.5	5.1
5	24.5	24.4	0.1	0.3
6	23.9	26.9	3.0	12.8

Table 4.5 Normal strains at south end support measured at maximum test load

Specimen No.	Top Flange		Bottom Flange	
	Max. Strain (με)	Min. Strain (με)	Max. Strain (με)	Min. Strain (με)
1	128	17.5	399	80.8
2	Gauge Failed	47.7	322	-13.5
3	264	-30.0	385	-65
4	783	4.5	520	179
5	155	-358	386	218
6	75.4	-107	252	183

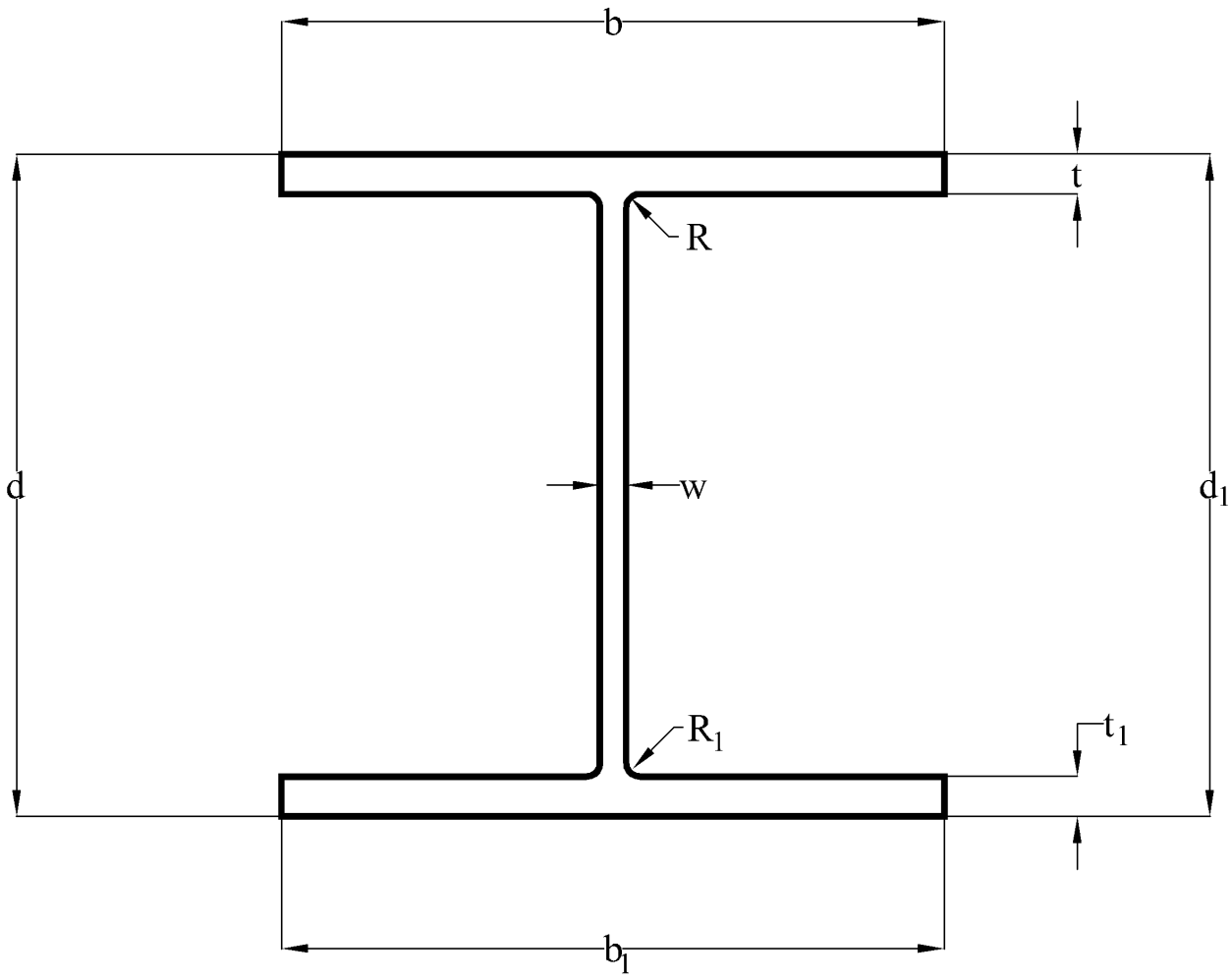

Figure 4.1 Cross-sectional measurements

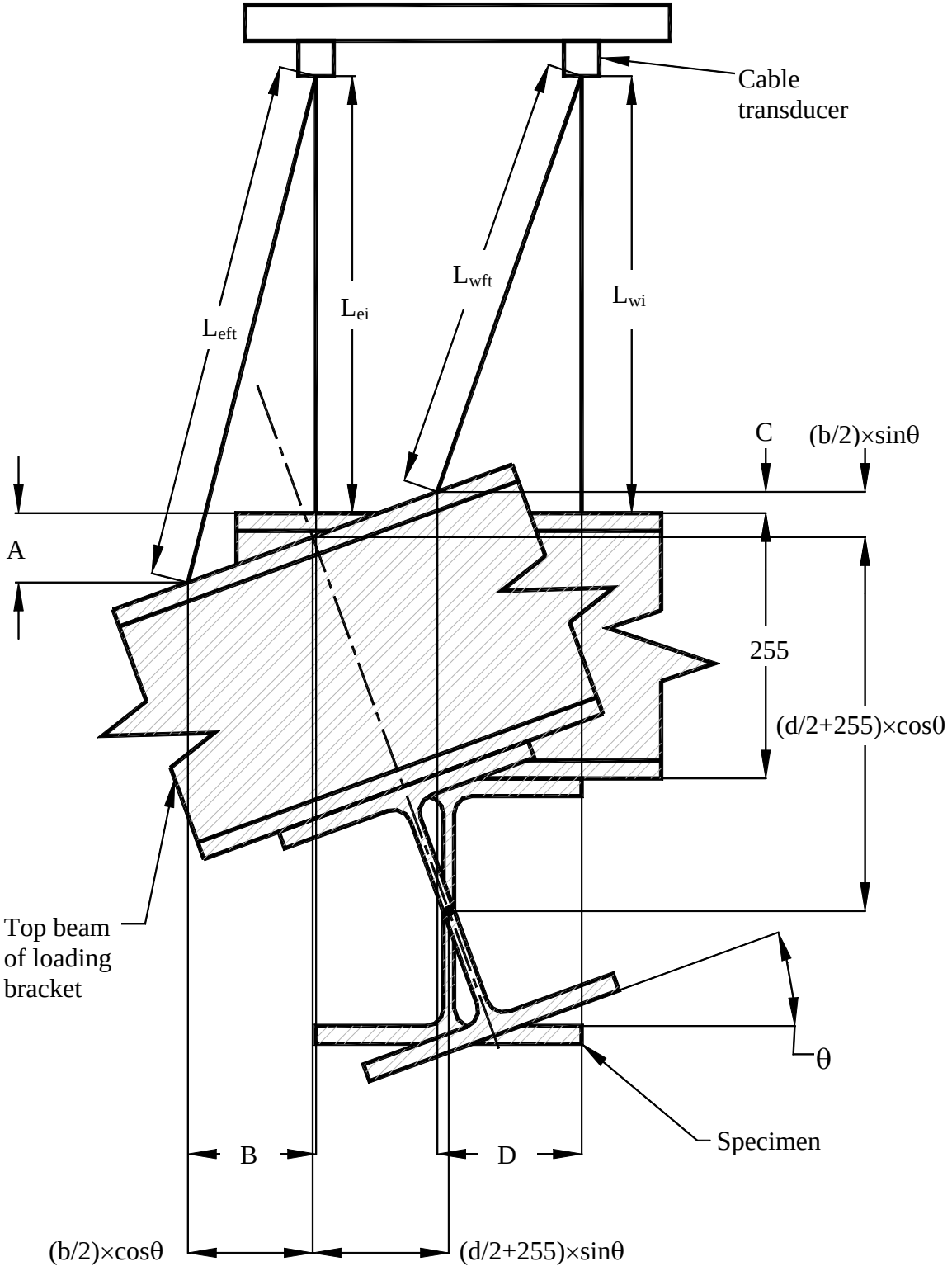

Figure 4.2 Influence of midspan twist on vertical deflection measurement

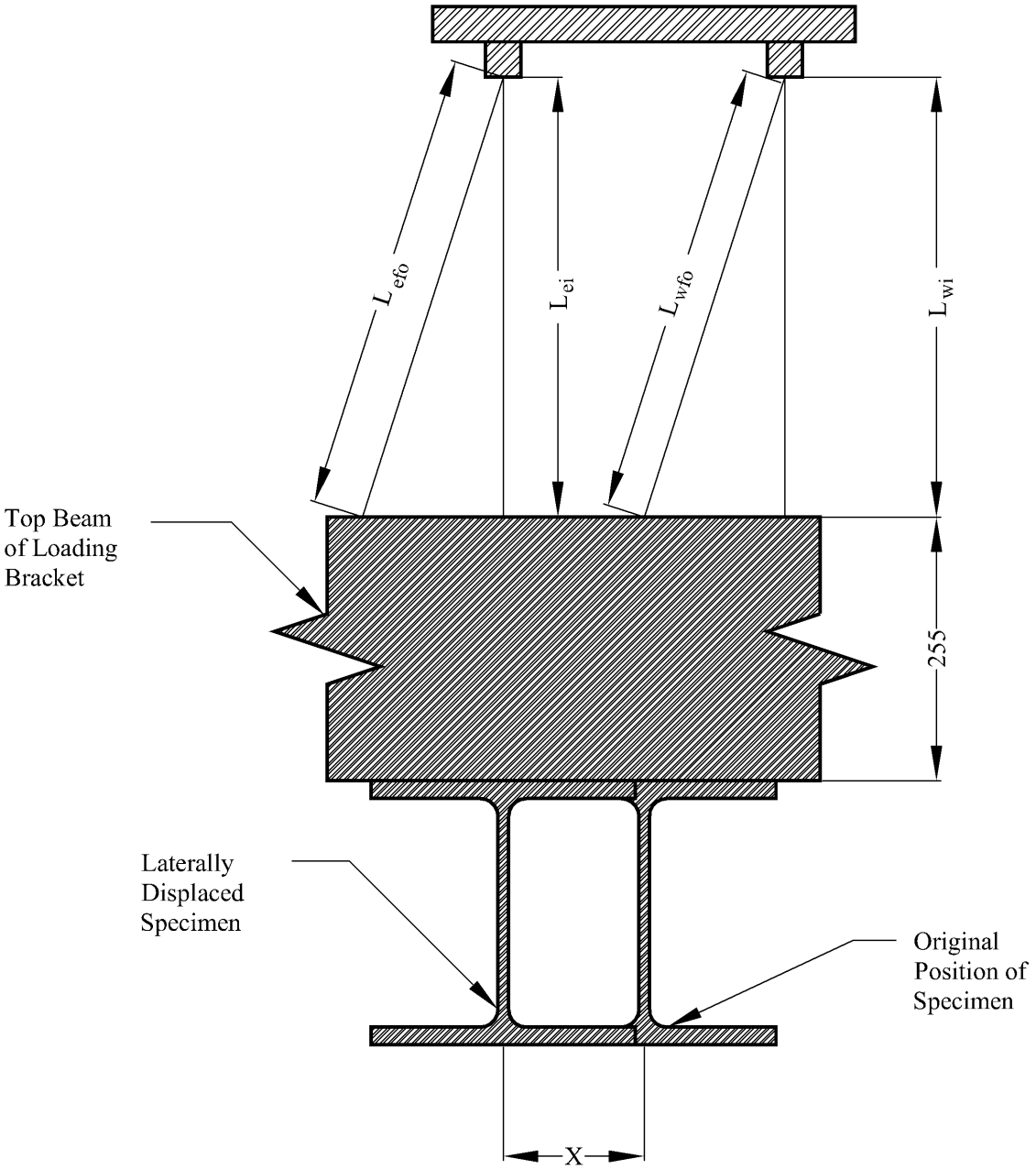

Figure 4.3 Influence of lateral displacement on vertical deflection measurement

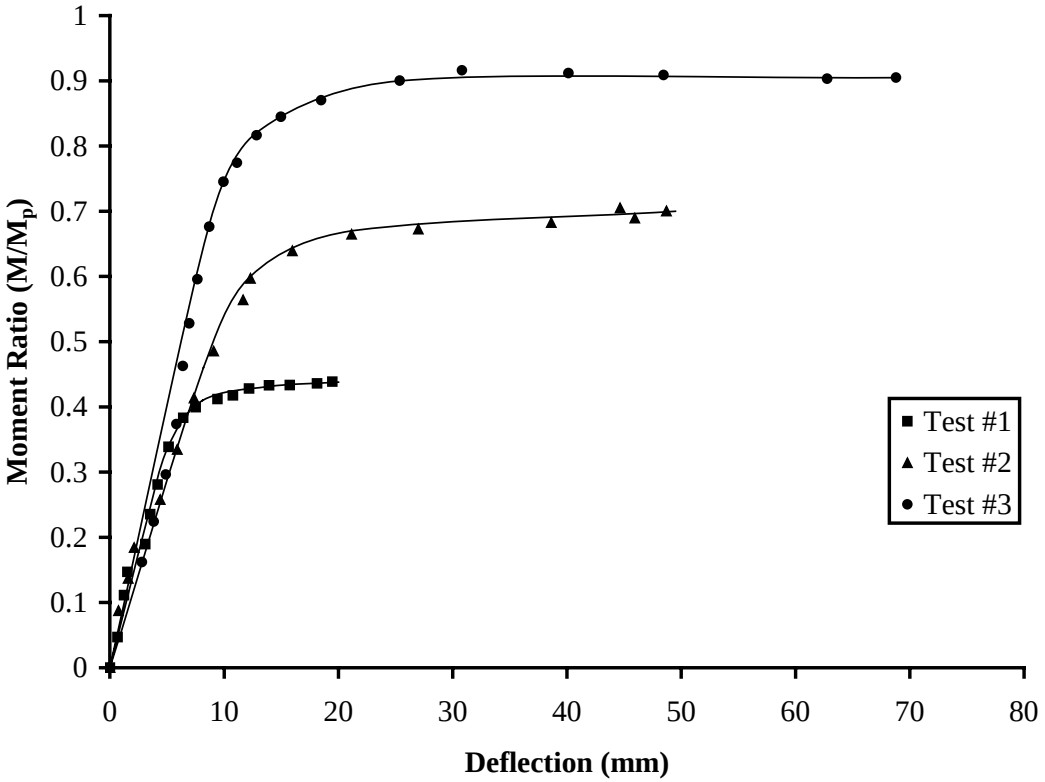

Figure 4.4 Moment-deflection relationship for Class 1 specimens

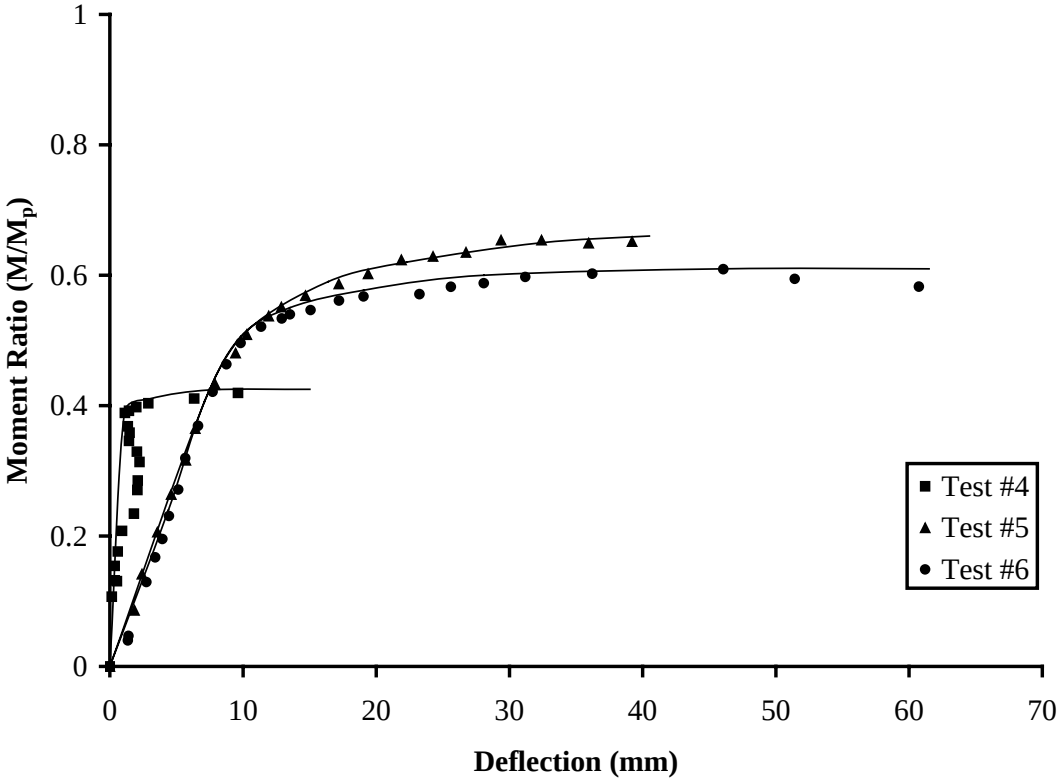

Figure 4.5 Moment-deflection relationship for Class 2 specimens

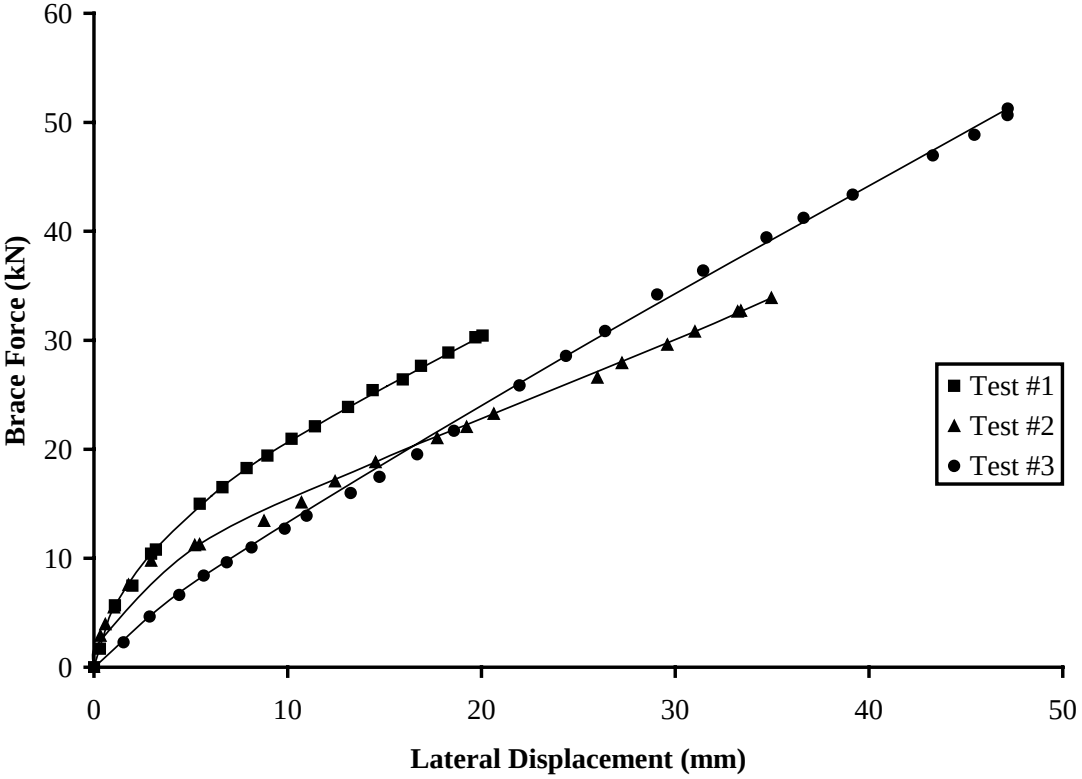

Figure 4.6 Relationship between lateral displacement and brace force Class 1 specimens

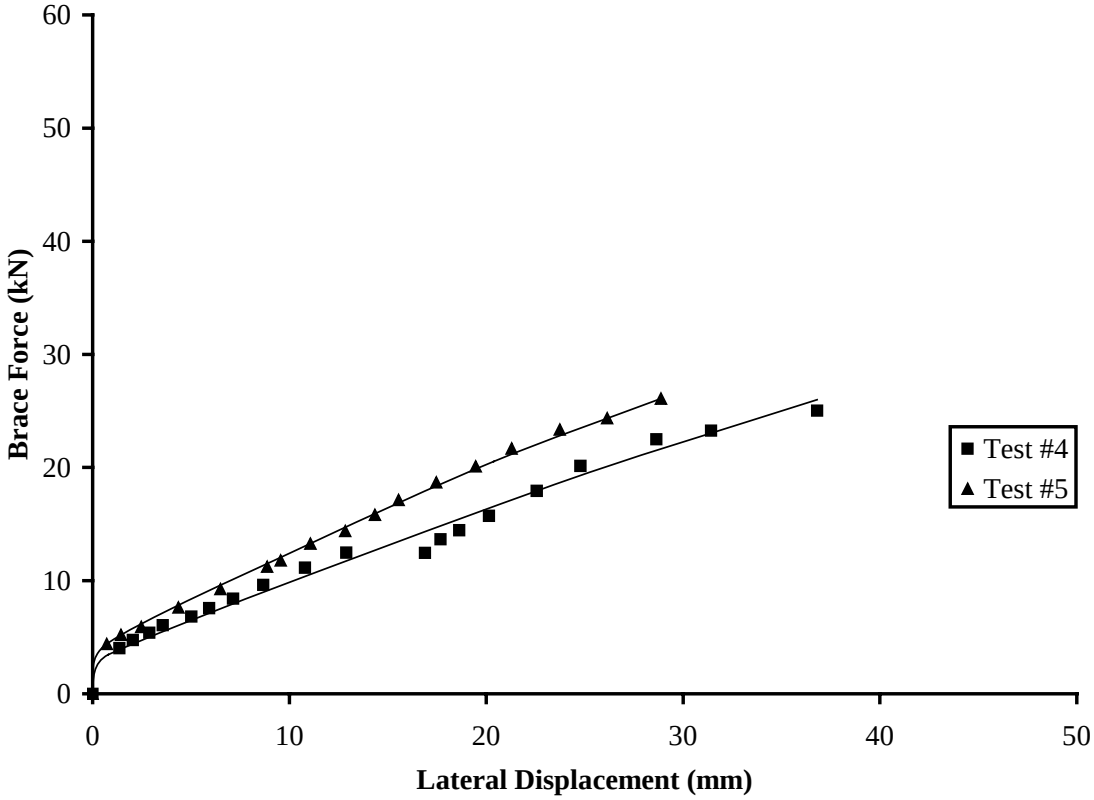

Figure 4.7 Relationship between lateral displacement and brace force Class 2 specimens

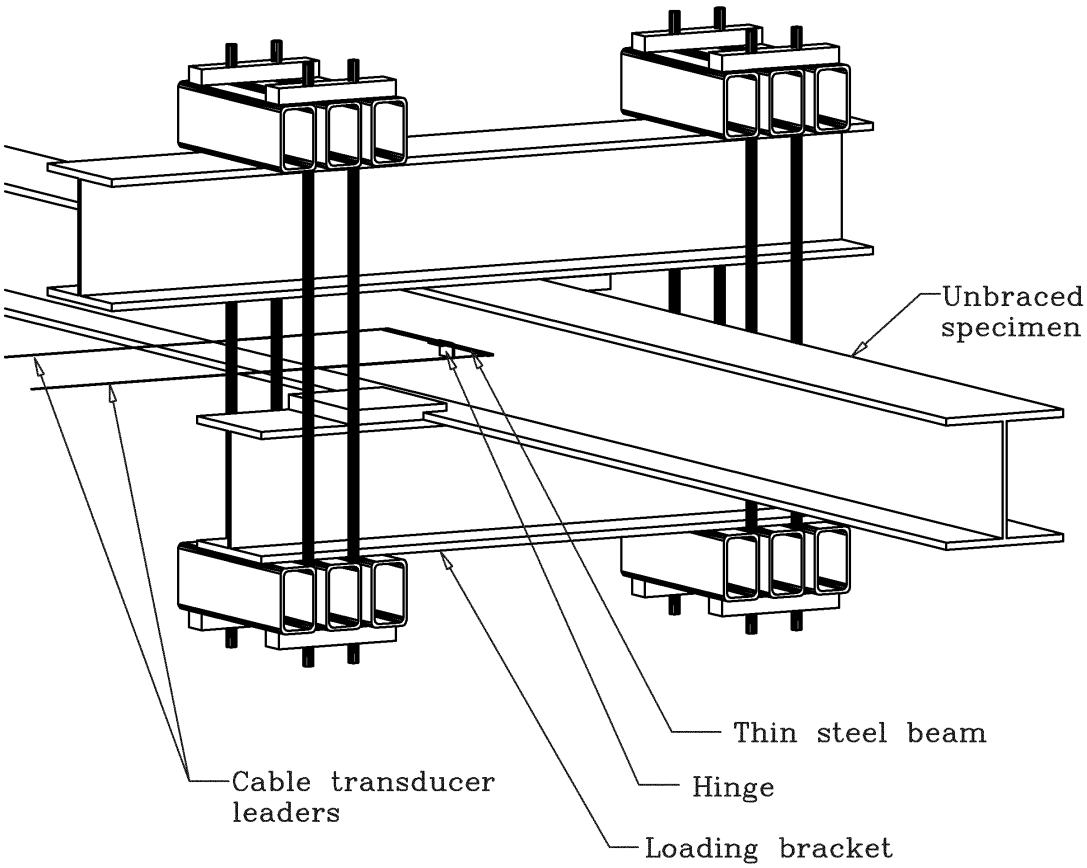

Figure 4.8 Lateral deflection measurement for unbraced specimen

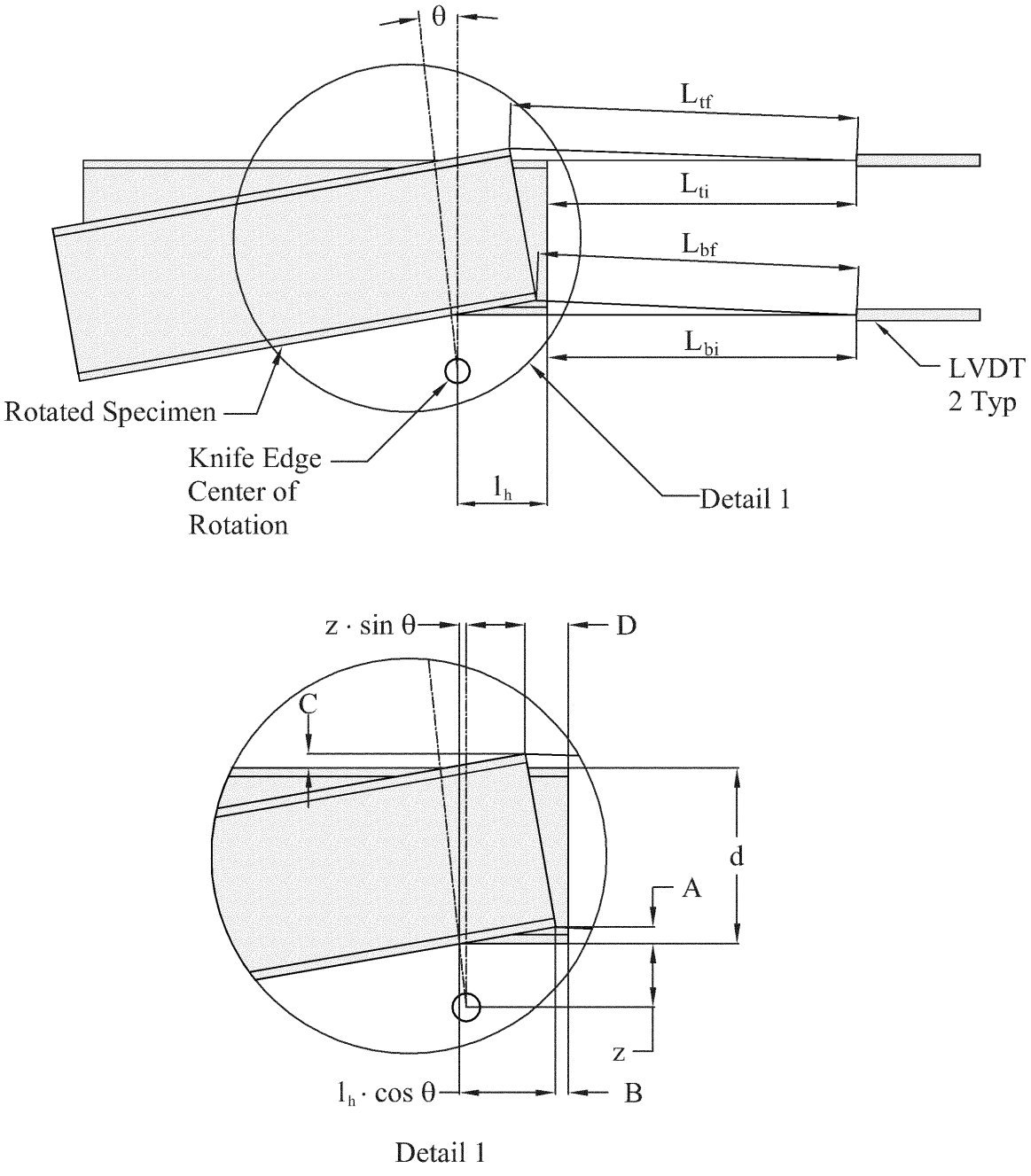

Figure 4.9 Influence of end rotation on measured flange tip displacement

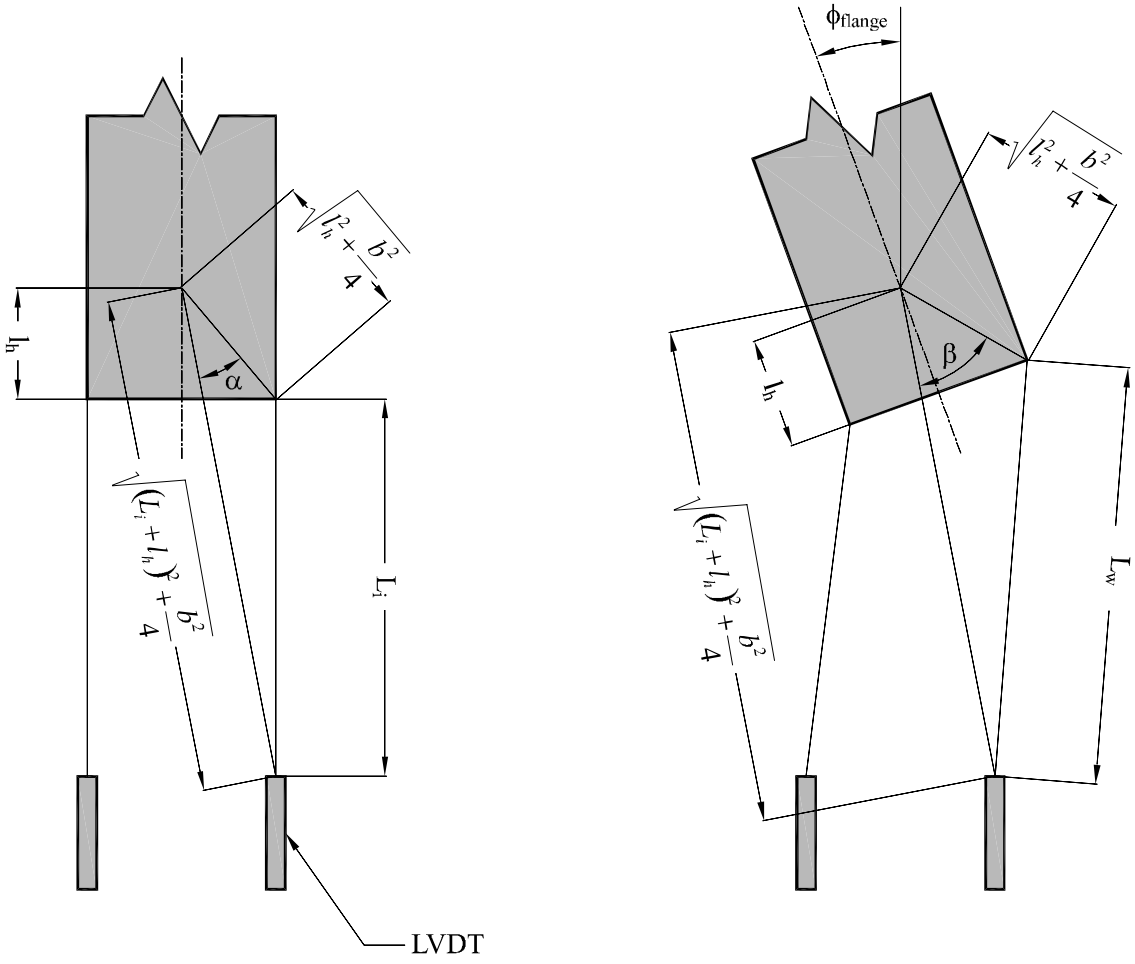

Flange End Rotation

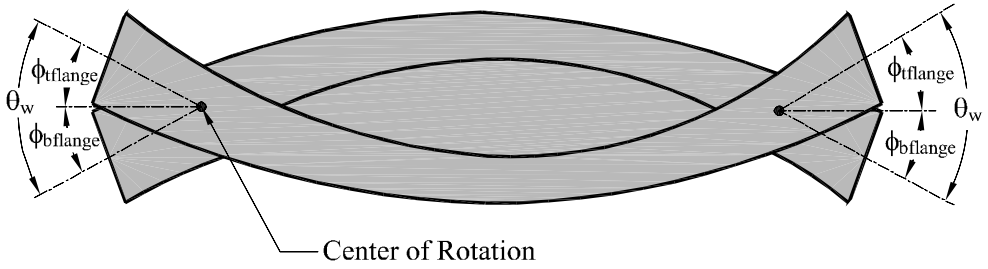

Figure 4.10 Plan view of beam showing warping angle measurement

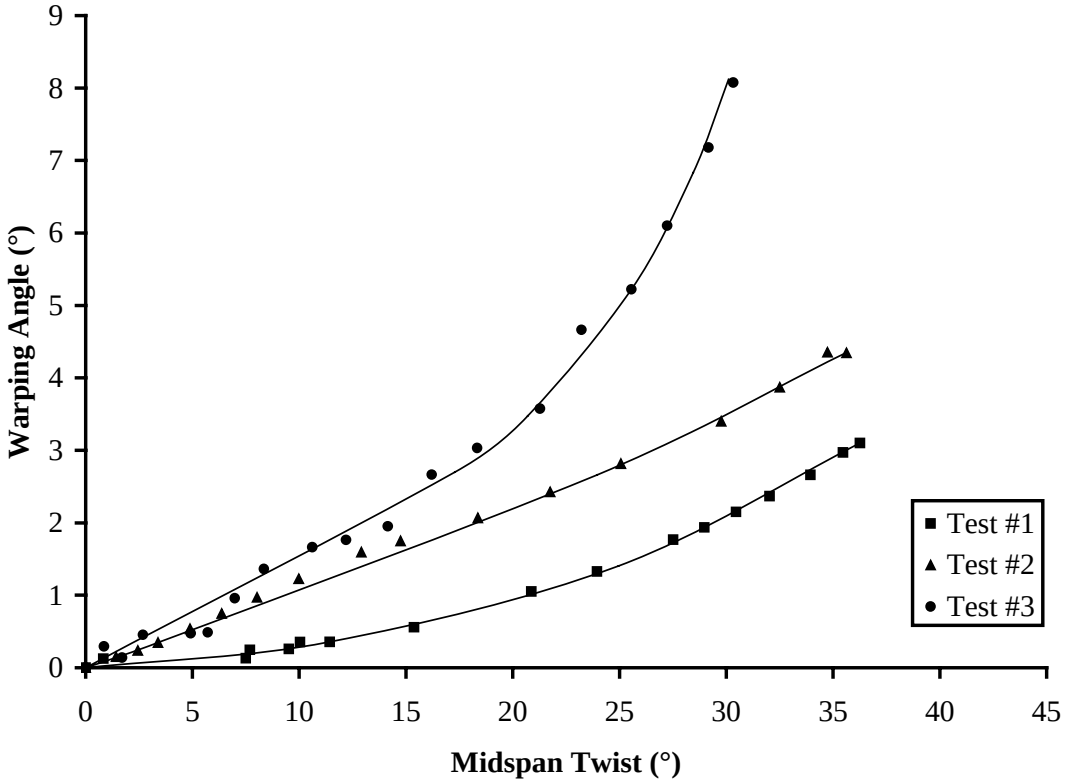

Figure 4.11 Warping angle vs midspan twist for Class 1 specimens

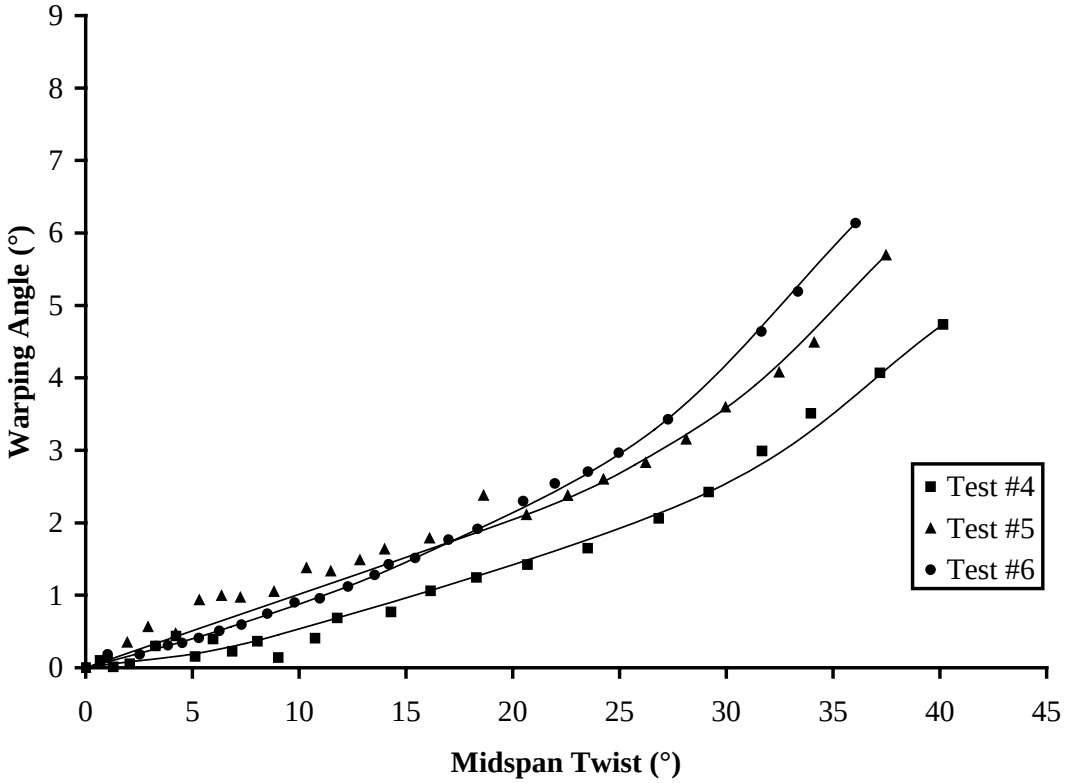

Figure 4.12 Warping angle vs midspan twist for Class 2 specimens

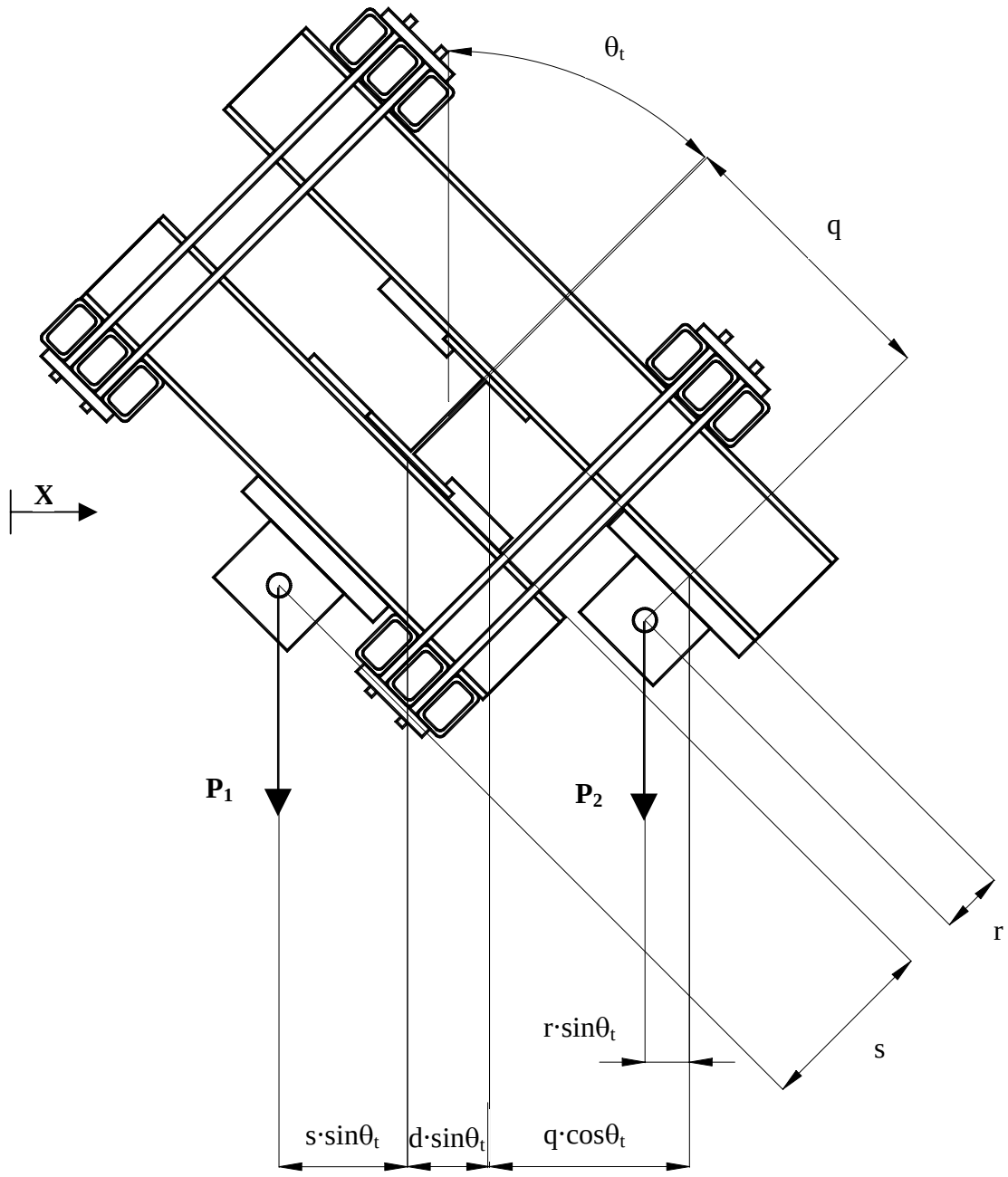

Figure 4.13 Applied torque calculation

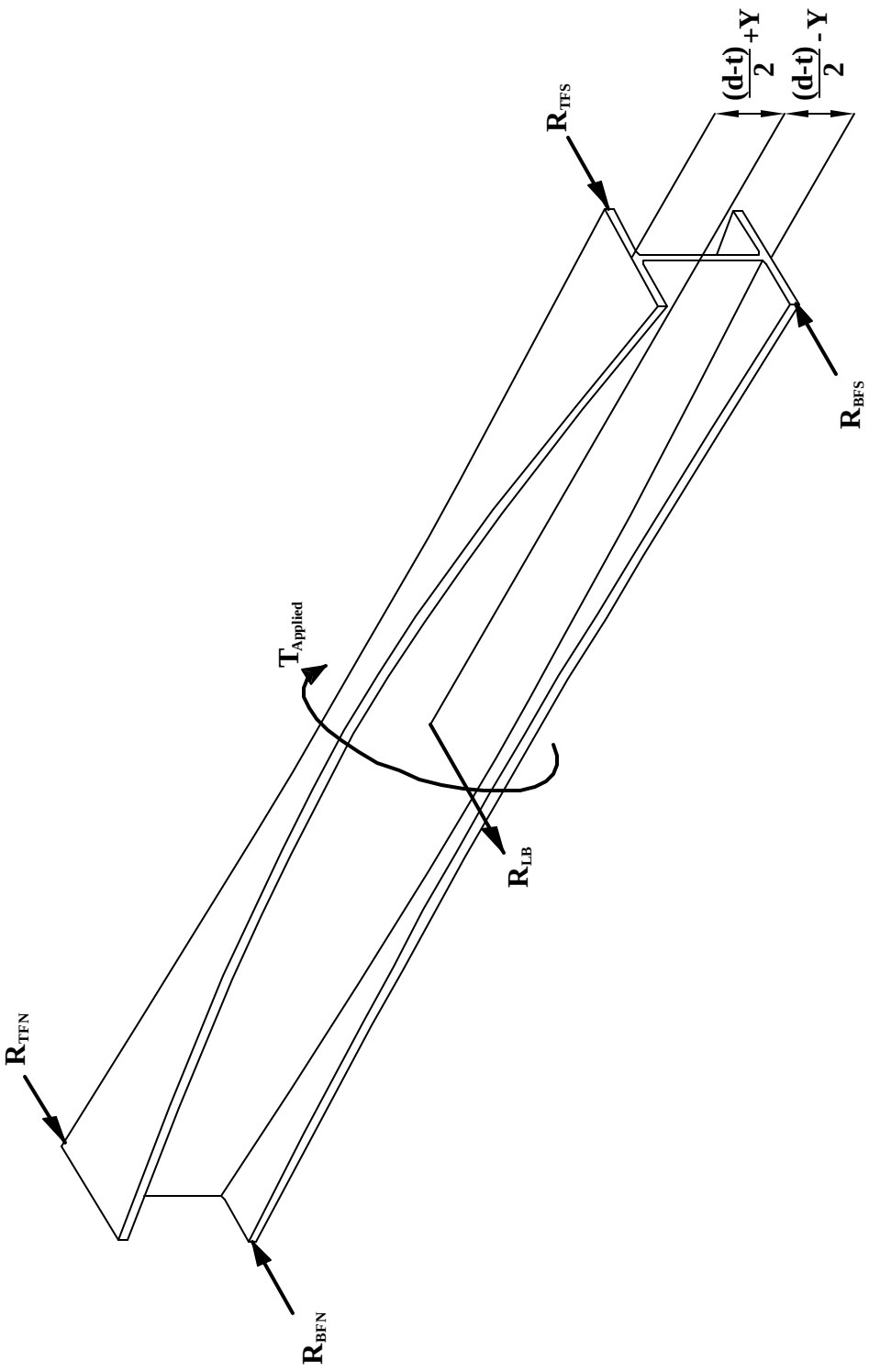

Figure 4.14 Resisting torque calculation

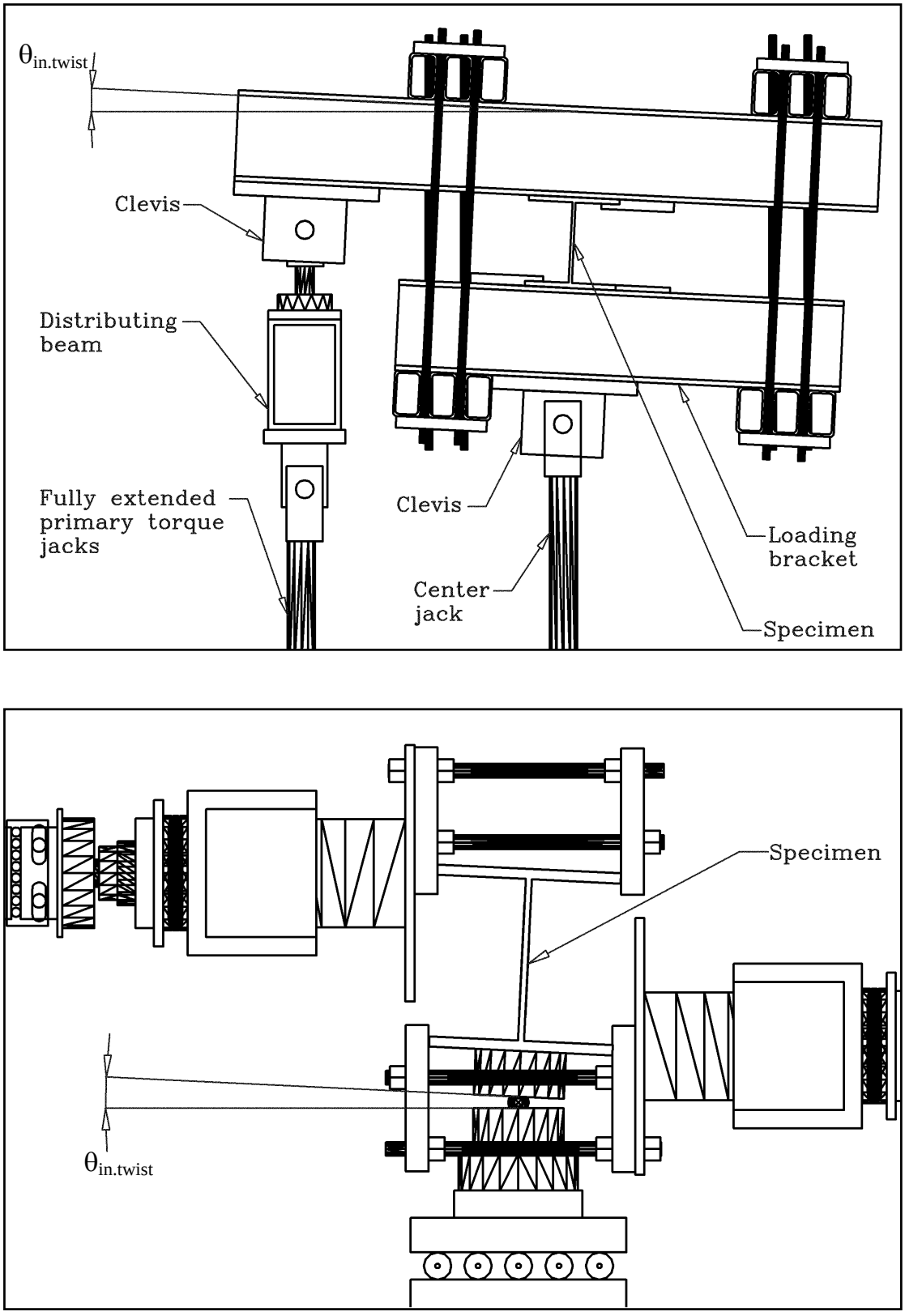

Figure 4.15 Initial angle of twist for specimens 2 through 6

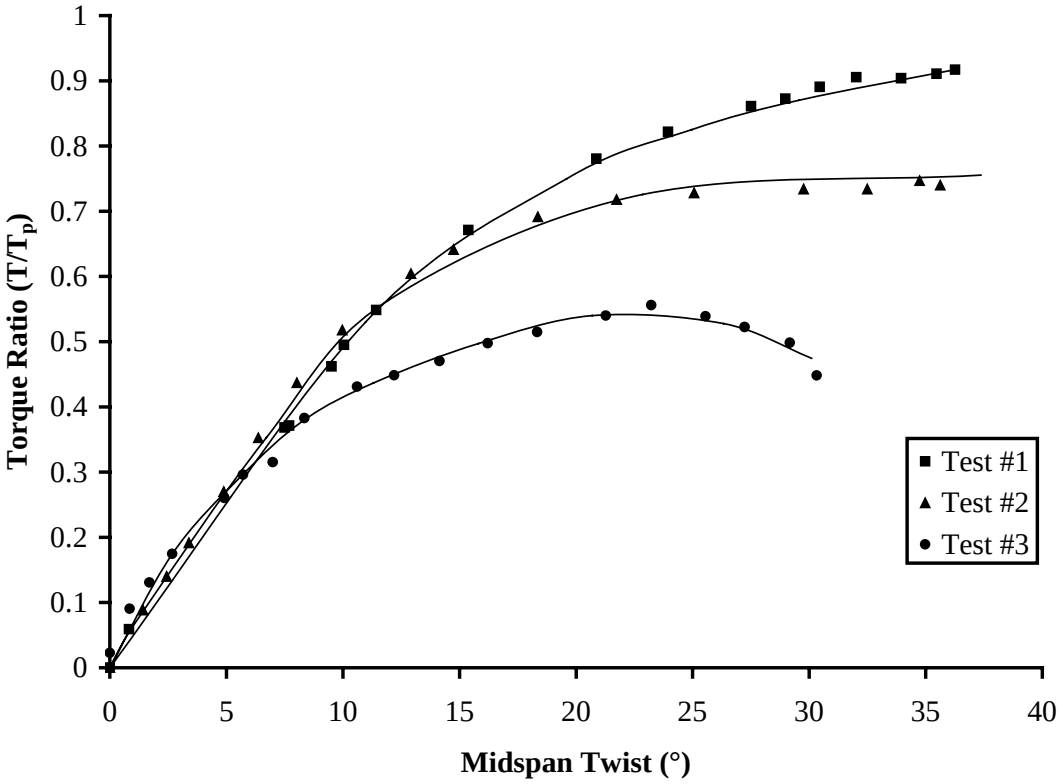

Figure 4.16 Relationship between torque and midspan twist for Class 1 specimens

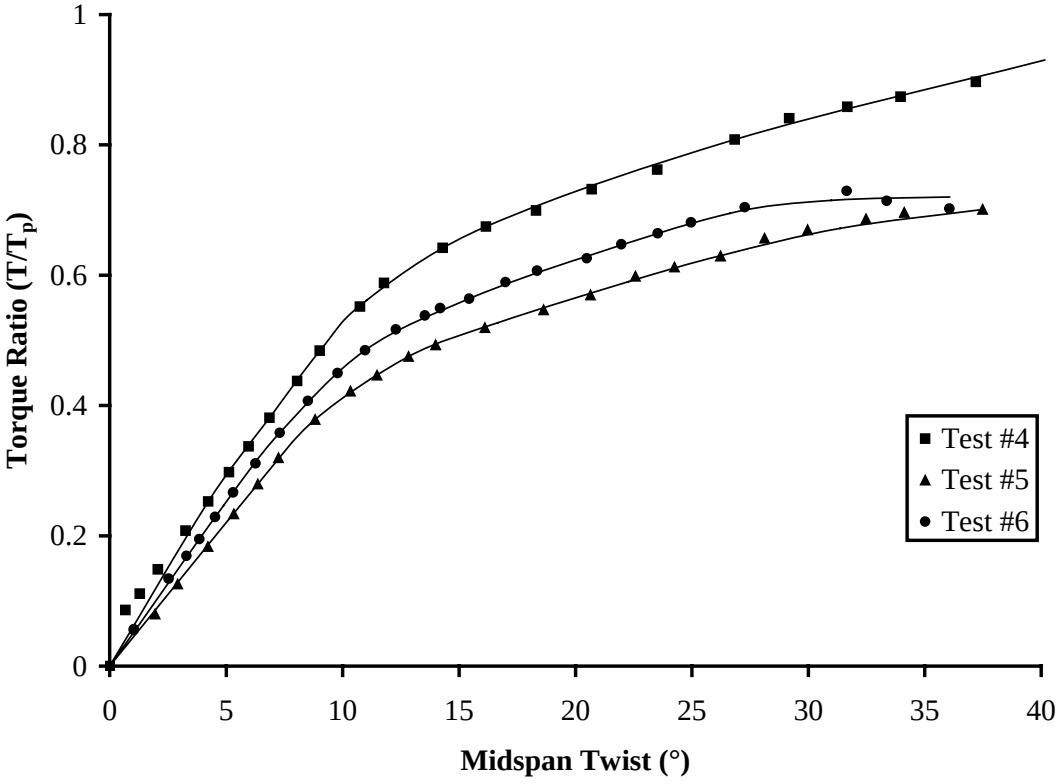

Figure 4.17 Relationship between torque and midspan twist for Class 2 specimens

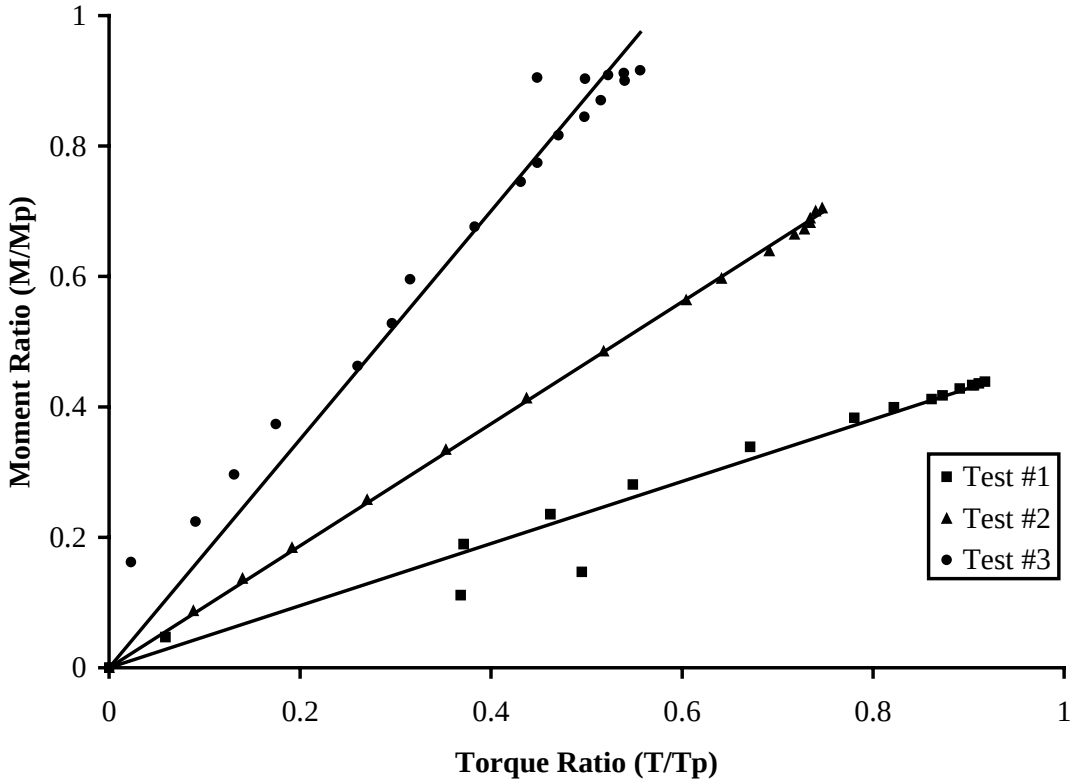

Figure 4.18 Relationship between bending moment and torque - Class 1 specimens

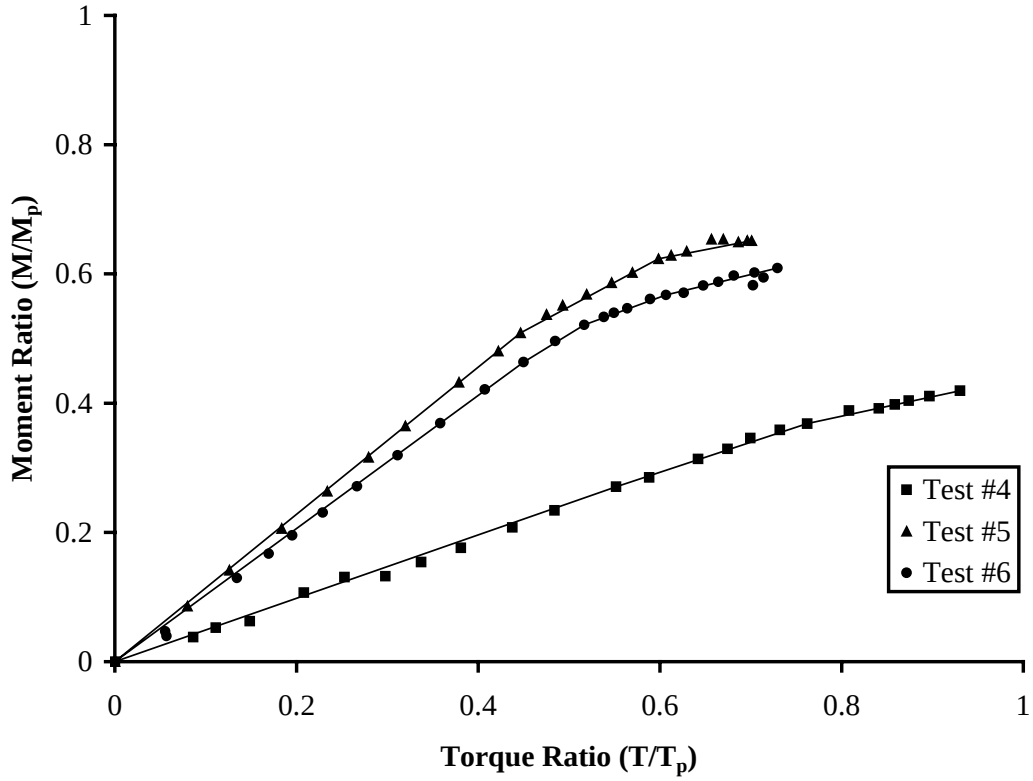

Figure 4.19 Relationship between bending moment and torque - Class 2 specimens

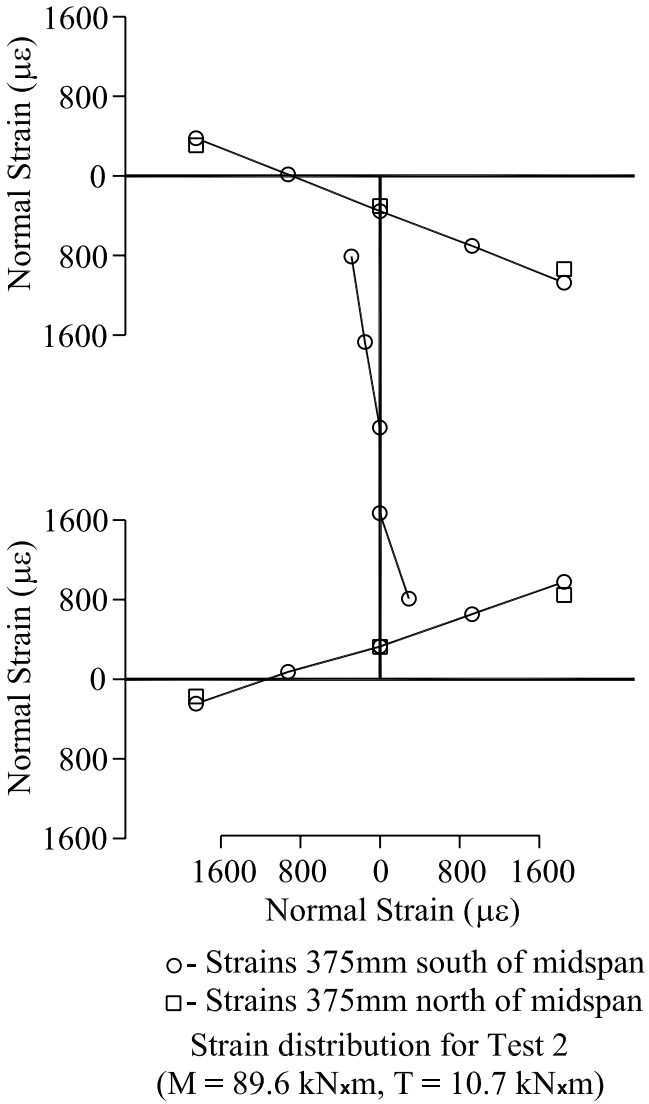

Strain distribution for Test 2
(M = 89.6 kN×m, T = 10.7 kN×m)

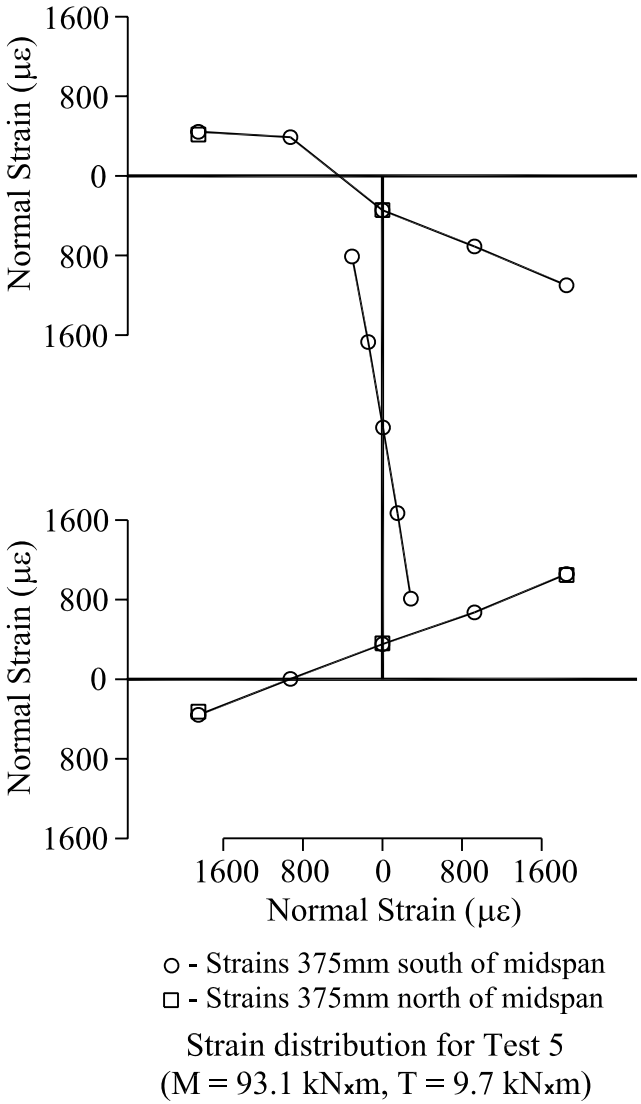

Strain distribution for Test 5
(M = 93.1 kN×m, T = 9.7 kN×m)

Figure 4.20 Typical strain distributions for I-shaped steel beams subjected to combined bending and torsion

5. Finite Element Analysis

5.1 General

The objective of the finite element analysis was to develop a model that would predict the behaviour of I-shaped steel beams subjected to combined bending and torsion. The analytic bending moment and torque capacities will be compared to the experimental beam strengths to validate the model. To further validate the model, the predicted load versus displacement responses will be compared to the observed response of the test specimens. A validated finite element model will provide a useful tool for evaluating the effect of parameters that were not specifically investigated in the test program. A full parametric study is, however, beyond the scope of this project.

Table 5.1 outlines the first phase of the finite element analysis in which a total of six models were analyzed, one corresponding to each of the tested specimens. The finite element analysis was performed using the commercial finite element software ABAQUS, version 5.7 (Hibbitt *et al*. 1997). The analysis was conducted on a SUN Ultra 1 workstation.

5.2 Description of the Model

5.2.1 Elements and Mesh

The ABAQUS S4R shell element was used to model the I-shaped beams. The S4R element is a four-node, doubly curved shell element that accounts for finite membrane strains and allows for changes in element thickness. This element has six degrees of freedom at each node: three displacement components and three rotation components. The S4R element only has one integration point located at the centroid of the element. The cross-sectional behaviour of the S4R element, however, is integrated at five points through the thickness (Hibbitt *et al*. 1997).

The size of the finite element mesh can have significant effects on the accuracy of the numerical results. In general, the smaller the element size the more accurate the determination of strain energy within the element. However, the finer the finite element mesh the greater the computational effort required. The selected finite element mesh was based on the results of a preliminary mesh refinement study. The model used for the study was a simply supported W250X67 beam pinned in torsion and loaded with 5:1, 10:1 and 20:1 moment-to-torque ratios. Three different meshes were studied; a coarse, intermediate, and fine mesh (see Figure 5.1). Table 5.2 summarizes the results of the mesh study. The intermediate mesh converged to within 0.8% of the fine mesh results with considerably less computational effort and was selected for use in the finite element analysis.

The tested specimens were modeled using 960 shell elements. Each model had 60 elements along the length, 8 elements over the depth of the web and 4 elements across the flanges. The aspect ratio of the web and flange elements was 2.4:1 and 1.4:1, respectively. The intermediate mesh shown in Figure 5.1 is an example of a typical undeformed finite element mesh used for the Class 1 specimens in the analysis program. The cross-sectional dimensions of each model were based on the average measured cross-section dimensions listed in Table 4.2.

The thickness of the elements located at midspan was increased to account for the effects of the brace-to-pin connection and loading bracket. During the experimental tests the midspan brace was connected to a pin that was clamped between two 25-mm thick plates bolted to either side of the web (see Figure 3.8). The thickness of the highlighted web elements in Figure 5.3 was set equal to the thickness of the web plus the two 25-mm thick plates: 59 mm for the Class 1 sections and 60 mm for the Class 2 sections.

The highlighted flange elements in Figure 5.3 had a thickness of 32 mm for the Class 1 sections and 30 mm for the Class 2 to simulate the influence of the loading bracket. The loading bracket prevented the flanges from buckling at midspan during the tests. The increased flange thickness represented the flange thickness of the specimen plus an assumed equivalent thickness of the attached loading beam. This equivalent thickness was taken as the thickness of the flange of the loading beam that was in contact with the specimen (16mm). Although this is a lower bound equivalent thickness, the

assumed thickness was sufficiently large to force failure of the model to occur outside the width of the loading bracket and rerunning the analysis with thicker midspan flange elements did not increase the strength of the beam.

5.2.2 Initial Conditions

The initial out-of-straightness of the beam was modeled using a half sine wave with an amplitude of $l/500$, where l is the span length. This value was based on initial out-of-straightness measurements taken of six untested specimens. An initial out-of-parallel for the flanges, as defined in Section 4.2, equal to that of the corresponding test specimen was used for each model.

The model also took into account residual stresses. A temperature gradient applied over the cross-section was used to create the residual stresses. A thermal expansion coefficient was included when defining the material properties of the beam and, for convenience, an initial temperature of 0°C was defined at all nodes as a reference temperature. The nodes were divided into 17 sets based on their location in the cross-section. In the first step of the analysis temperature changes were introduced to at each node set to create the desired residual strains in the cross-section. The desired residual strains were obtained by dividing the residual stresses by the modulus of elasticity used in the finite element model. The applied temperature gradient and the resulting average longitudinal membrane stresses recorded at the end of the first step of the analysis are plotted in Figure 5.4. The applied temperature change at each node set is also listed in Table 5.3.

5.2.3 Material Model

The I-shaped beams were modeled using an isotropic, elastic-strain-hardening material. The constitutive model incorporated a von Mises yield surface and an isotropic strain hardening flow rule. Nominal stress versus strain data obtained from the coupon tests were converted to true stress and logarithmic strain curves to define the material response. Figure 5.5 shows the material model used to model the Class 1 specimens

while Figure 5.6 shows the material model used for the Class 2 sections in the finite element analysis. The stress and strain values used for the FEA material model are also presented in Table 5.4.

5.2.4 Boundary Conditions

A spring element was used to model the lateral brace used in the test setup. The SPRING1 element from ABAQUS, which acts as a spring between a node and ground, was attached to the center node of the model (see Figure 5.2). The SPRING1 element will follow the center node as it deflects vertically while providing partial lateral restraint simulating the tension brace and glider box assembly used in the test setup. The stiffness of the spring element was calculated from the midspan lateral deflections and the tensile strains in the lateral braces measured during the tests (see Section 4.4.2). The ratio of the midspan lateral deflection over the corresponding lateral bracing force varied throughout the loading history of each test. A piece-wise linear spring stiffness was used in the analysis to simulate the variation in the stiffness of the lateral bracing system. Table 5.5 shows the lateral displacements and corresponding brace forces that were used to define the stiffness of the spring element for the Class 1 and Class 2 specimens.

Each model had a total length of 4600 mm and a clear span of 4000 mm. At 2000 mm on either side of midspan the models were vertically pinned at the node located at the intersection of the web and bottom flange (see Figure 5.2). These restraints provided vertical support, but allowed strong axis rotation similar to the vertical end reactions used in the experimental program. However, during the tests the strong-axis end rotation was about the center of the spherical bearing, 12mm below the underside of the flange, instead of directly at the flange-to-web junction as it was modeled during the analysis.

An ideal torsionally-pinned connection was simulated in the experimental program using rockers, rollers and bearings at the end supports (see Section 3.3.1). For the finite element analysis, lateral restraints at the flange-to-web junctions located 2000 mm from midspan (see Figure 5.2) were used to model this ideal torsionally-pinned

connection. A longitudinal displacement restraint was provided at the center node of the model for stability (see Figure 5.2).

5.2.5 Loading

The loading bracket was not incorporated into the finite element model. A concentrated vertical load and a concentrated torque were applied to the node located at the center of the model to simulate the test loading condition. The increased thickness of the web elements at this location minimized local deformations caused by the concentrated vertical load and torque (see Figure 5.3).

5.3 Analysis

The finite element analysis used a linear load path to approximate the loading of the Class 1 sections as shown in Figure 5.7. The slope of the finite element load paths for the Class 1 specimens were controlled to within 7% of the mean slope of the corresponding experimental tests. A piece-wise linear load path was used to approximate the loading of the Class 2 specimens as shown in Figure 5.8. The slope of the analytical load path was within 1% of the corresponding experimental load path for the Class 2 specimens. The moment and torque values used to define the piece-wise linear load path for the Class 2 specimens are also shown in Table 5.6. The models were analyzed using a nonlinear static analysis performed by ABAQUS. The analysis included the effects of both geometric and material nonlinearities.

5.4 Analysis Results

The maximum bending moment and torque carried by each model are listed in Table 5.7. Table 5.7 also lists the maximum bending moments and torques of the corresponding test specimens as well as the test-to-predicted ratios. As discussed in Section 4.4.1 the primary torque actuators ran out of stroke before any reduction in the

moment carrying capacity of the beams was observed. Despite this the experimental capacity of all of the specimens was greater than that predicted by the FEA model.

For the Class 1 sections (specimens 1, 2, and 3) there was a significant discrepancy between the experimental and predicted bending moment capacities. The largest difference was seen in specimen 2, which had a measured bending moment capacity 26% higher than that determined with the FEA model. The test-to-predicted ratio ranged from 1.09 to 1.26 for the bending moment capacities of the Class 1 sections as shown in Table 5.7. The moment capacity predictions were closer to the measured moment capacities for the Class 2 sections (specimens 4, 5, 6). The predicted moment capacity was within 8% of the measured capacity for Specimen 5 and Specimen 6. The percent difference of the test-to-predicted torque capacities ranged from 14% to 26 % for the Class 1 specimens and 2% to 21 % for the Class 2 specimens.

The predicted bending moment versus vertical deflection relationships obtained from the analysis are plotted in Figure 5.9 for the Class 1 sections and in Figure 5.10 for the Class 2 sections. In Figure 5.9 it is shown that in addition to underestimating the capacity of the Class 1 specimens the FEA models also exhibit a softer response with a more gradual transition from the initial linear slope to the capacity plateau. Although not as pronounced as for the Class 1 specimens, Figure 5.10 shows that the Class 2 FEA models also exhibit a more gradual transition from the initial linear slope to the capacity plateau than their corresponding test specimens. The initial linear slope of the predicted moment versus deflection curves is compared to the slope of the recorded experimental moment versus deflection response in the elastic region in Table 5.8 for the Class 1 and Class 2 specimens. The percent difference of the test-to-predicted slopes in the linear region ranged from 0.4% to 8% for the Class 1 specimens. The vertical deflection measurements were quite erratic during Test #4 and prevent any meaningful comparison of the test-to-predicted slopes in the initial linear region for this specimen. For the remaining 2 Class 2 specimens the percent difference of the test-to-predicted slopes in the linear region were within 3%. It is evident from the ratio of the initial slopes that the FEA model is able to more accurately predict the response of the beam in the elastic region.

The relationship between torque and midspan twist observed during the experimental tests is compared to the relationship predicted by the FEA model in Figure 5.11 and Figure 5.12 for the Class 1 and Class 2 sections, respectively. It is apparent from both figures that the finite element models actually show a greater initial torsional stiffness than the test specimens. The experimental torque versus midspan twist curves have a shallow initial slope followed by a gradual transition to the capacity plateau. The torque versus midspan twist response predicted by the finite element models has a steeper initial slope with a more abrupt transition to the capacity plateau.

The deformed shape of the finite element model closely resembles the observed deformation of the test specimens (see Figure 5.13). Despite the fact that the FEA models underestimate the capacity of the beams the finite element model is able to provide a good prediction of the initial response of the I-shaped steel beams to the combined bending and torsional loads.

5.5 Sensitivity Study

The primary purpose of the experimental portion of this research was to obtain test results that could be used to validate a finite element model. The desired experimental boundary conditions including lateral support, free rotation, and ideally pinned connections in both torsion and bending necessitated an elaborate test set-up. Despite an attempt to model these conditions as closely as possible in the laboratory ideal conditions can never be fully realized because of the physical limitations of friction and gravity and it is evident from strain gauge readings that ideally pinned end supports were not fully obtained. Also, as discussed in Chapter 4 the complexities of the test set-up created several challenges with the measurements of displacements and forces.

The ABAQUS SR4 element has been used extensively in finite element analysis and has proven to be robust. The discrepancy between the FEA results and the experimental results seems to indicate that the ideal boundary conditions used in the FEA model do not accurately represent the boundary conditions that were achieved in the laboratory. To help understand the reason for the discrepancies between the experimental

results and FEA results the sensitivity of the analysis to varying material properties and to boundary conditions with different levels of fixity was investigated.

5.5.1 Sensitivity to Material Strength

The material model used in the analysis (see Figure 5.5 and Figure 5.6) was based on the results of coupon tests performed on material taken from the top flanges of the Class 1 and Class 2 sections as discussed in Section 4.3. However, the strength of an I-shaped beam is typically not homogeneous over the cross-section. Since no material tests were conducted on the web material any variation in the strength of the section was not accounted for in the FEA model.

Another reason that the sensitivity of the FEA model to varying material strengths should be investigated is the low yield strengths determined from the coupon tests. The material grade of both sections was classified as G40.21-M 300W, which has a minimum yield strength of 300MPa. Although 300MPa is the minimum yield strength for G40.21 300W actual yield strengths for this grade of material are typically closer to 350MPa. The yield strength determined from the coupon tests for the Class 2 sections was just 300MPa and the coupons taken from the Class 1 sections actually had a yield strength of 297MPa just below the allowed minimum for G40.21 300W. The extensometer was calibrated just prior to the coupon tests and the results from all coupons for each section were in close agreement. So despite the low measured yield strengths there is a strong level of confidence in the results. To help understand the reason for the discrepancies between the measured and predicted beam capacities, the sensitivity of the FEA model to changing material strength was investigated.

To assess the sensitivity of the FEA model to changes in material strength the analysis for Specimen 1 was re-run using the material model shown in Figure 5.14. The new material model had the same modulus of elasticity as the one shown in Figure 5.5, but the yield strength was increased from the 297MPa used in the original analysis to 350MPa. A comparison of the moment-deflection relationship between the beam with the increased yield strength and the original analysis is shown in Figure 5.15. The torque-rotation comparison between the same two beams is shown in Figure 5.16.

The moment-deflection and torque-twist relationships plotted in Figure 5.15 and Figure 5.16 respectively show that an increase of 16.8% in the yield strength of the material translated to an increase of 9.9% in the capacity of Specimen 1. However, even with the large increase in yield strength the capacity determined from the analysis is still 5% below the experimental results. The yield strengths determined from the coupon tests are on the lower end for G40.21-M 300W, but the tests were conducted in strict accordance to ASTM and there is no reason to suspect any gross errors in the results. The yield strengths determined from the coupon tests were within 1% for both the Class 1 and Class 2 sections. Therefore, any errors in the determination of the material yield strength likely account for less than 1% of the discrepancy between the measured and predicted beam capacities.

5.5.2 Sensitivity to Stiffness of Lateral Restraint

The stiffness of the lateral spring used in the FEA model was based on the lateral deflection of the test specimens and the measured strains in the lateral braces. However, as discussed in Chapter 4 there was no direct measurement of the lateral deflection at midspan for the Class 1 tests, but rather the lateral deflection was extrapolated from the sway measurements of the bracing frame. A sensitivity test of the FEA model to the stiffness of lateral restraint was performed because of the potential for errors in the determination of the experimental brace stiffness. The analysis for Specimen 1 was re-run with a completely fixed lateral support to determine the upper bound influence of the lateral support. The influence of the spring stiffness on the moment-deflection behavior and torque-rotation behavior for Specimen 1 are shown in Figure 5.15 and Figure 5.16, respectively.

Figure 5.15 and Figure 5.16 show that changing the spring to a completely rigid lateral support increased the capacity of Specimen 1 by 9.9%. Although there was some uncertainty in the level of lateral support used during the tests, it is certain that a complete rigidity was not achieved and the results of the rigid support analysis represent an upper bound to the influence of the lateral support on the capacity of the beam. The capacity determined from the analysis of Specimen 1 with rigid lateral support is still 5%

less than the experimental capacity of Specimen 1. Therefore, although errors in the lateral support measurements may explain some of the discrepancy between the analytical and experimental results this error was not the sole contributor.

5.5.3 Sensitivity to Level of Torsional Restraint

The end supports used in the test setup attempted to simulate torsionally-pinned end conditions. However, strain gauges located at the south end support recorded variations in normal strain across the flanges (see Section 4.4.5) and it is evident that the torsional-end supports provided during the tests did not permit free warping. Although it is known that there was partial warping restraint, it is difficult to quantify the influence of friction forces in the rollers and bearings or the influence of misalignment of the rocker to the component of the torsional reaction. Still it is clear that the ideal torsional restraints used in the FEA model were not fully achieved in the laboratory. To bound the influence of the end supports the FEA model for Specimen 1 was re-analyzed with completely fixed torsional end restraints. The fixed torsional end condition was modeled by boxing the beams at the support locations. Finite elements were used to model 50mm thick plates, 250mm long, centered about the support locations and welded between the top and bottom flange tips on both sides of the beam (see Figure 5.17). The plate size was selected by re-running the analysis several times to determine a plate size beyond which there was no increase in the beam's capacity.

Figure 5.15 and Figure 5.16 show that fixing the end supports of Specimen 1 in torsion increases the capacity of the beam by 67%. Partially fixed torsional end restraints would increase the capacity of the beams and may help explain the discrepancy between the experimental and analytical results. However, in addition to increasing the capacity of the beam Figure 5.16 also shows a drastic change in the relationship between the applied torque and midspan twist. As expected the torsionally fixed Specimen 1 has a much stiffer response to the applied torque shown by the steep initial slope of the torque-twist curve. Although, there was some uncertainty in the level of fixity at the end supports during the tests the slope of the experimental torque-twist curve much more

closely resembles the response of a torsionally pinned support than the response of the torsionally fixed support.

5.6 Other Sources of Errors

Razzaq and Galambos (1979) have shown that the capacity of an I-shaped steel beam subjected to combined bending and torsion is dependent on the loading history. The load paths used in the finite element analysis very closely approximated the moment-to-torque curves recorded during the tests. However, as discussed in Section 3.3.2, during testing the moment-to-torque ratios could not be held constant between the recorded data points. The unknown fluctuation in experimental moment-to-torque ratios between data points made it impossible for the analysis to follow the experimental loading history exactly. However, the errors introduced from not following the exact loading history are most likely minimal as static yield points were only taken at the recorded data points.

5.7 Summary of the Finite Element Analysis

The deformed shape of the FEA model closely resembles the deformed shape of the test specimens. The FEA model was also able to closely approximate the initial response of the I-shaped steel beams to combined bending and torsion. However, the finite element model underestimated the capacity of the I-shaped sections subjected to combined bending and torsion by as much as 26%.

There is evidence that the sought after ideal boundary conditions, which can be simply modeled with finite elements, were not fully achieved in the laboratory. The losses due to friction and misalignment are not easily quantified and a sensitivity study of the FEA model revealed that the discrepancy between the experimental and analytical results could not be attributed to only one source of error.

5.8 Parametric Study

Although the desired loading and restraint conditions were very closely approximated during the tests, practical limitations prevented the attainment of both true torsionally-pinned end supports and a completely rigid midspan lateral brace. However, in order to provide a more meaningful comparison with the results of other researchers an analysis that more closely modeled ideal boundary conditions was undertaken.

The six finite element models were re-analyzed with ideal torsional end supports. The vertical restraints at the intersection of the web and bottom flange and the lateral restraints at the flange-to-web junctions used in the first phase of the analysis were retained. Also, the midspan flange elements were not increased in thickness to simulate the presence of the loading bracket, but rather maintained their original thickness so that the behavior of the flanges at the critical section could be investigated. The thickness of the midspan web elements was kept at the same thickness used in phase one in order to minimize local distortions at the loading point. The parametric models were loaded at the same initial moment-to-torque ratios and followed the load paths as the corresponding phase 1 model (see Table 5.9).

The influence of the midspan lateral brace was further investigated in the parametric study. Both unbraced and braced conditions were analyzed for models 1 through 4. Since models 5 and 6 were loaded at approximately the same loading rate, only a braced model 5 and an unbraced model 6 were analyzed. Table 5.9 summarizes the 10 models analyzed in this parametric study.

Figure 5.18 shows the moment versus midspan vertical deflection relationship for the Class 1 sections with ideal torsionally-pinned end supports. The same relationship is shown for the Class 2 sections in Figure 5.19. As expected the beams subjected to the greatest moment-to-torque ratio have the largest bending moment capacity. Figure 5.18 shows that the Class 1 sections experienced a reduction in bending moment capacity ranging from 17 to 23 % when the midspan lateral brace was removed. The Class 2 sections tested at an initial bending moment-to-torque ratio of 5:1 and 10:1 both experienced a reduction in bending moment capacity of approximately 15 % when the midspan lateral brace was removed (see Figure 5.19).

Figure 5.20 and Figure 5.21 show the relationship between torque and midspan angle of twist for the torsionally pinned Class 1 and Class 2 sections, respectively. Figure 5.20 shows that the Class 1 sections experience a reduction in torque capacity from 17 to 27% when the midspan lateral brace is removed. Figure 5.21 shows that the removal of the midspan lateral brace causes the Class 2 sections to experience a reduction in torque capacity ranging from 16 to 24%.

Table 5.1 First phase of analysis

Analysis No.	Corresponding Test Specimen	Class	Initial B.M/Torque Ratio	Span (m)	Lateral Support Condition
1	1	1	5:1	4	Braced
2	2	1	10:1	4	Braced
3	3	1	20:1	4	Braced
4	4	3	5:1	4	Braced
5	5	3	10:1	4	Braced
6	6	3	10:1	4	Unbraced

Table 5.2 Mesh refinement study results

Mesh Size	Moment-to-Torque Ratio	M_{max} (kN·m)	T_{max} (kN·m)	Midspan Deflection @ M_{max} (mm)	Midspan Rotation @ T_{max} (mm)
Coarse Mesh	5:1	130	26.0	30.3	34.7
	10:1	202	20.2	32.0	24.9
	20:1	266	13.3	38.1	19.2
Intermediate Mesh	5:1	128	25.6	31.4	35.5
	10:1	199	19.9	33.8	25.9
	20:1	262	13.1	40.6	20.2
Fine Mesh	5:1	127	25.4	31.6	35.7
	10:1	198	19.8	35.4	27.0
	20:1	261	13.1	41.7	20.6

Table 5.3 Temperature gradient used to create residual stresses

Top Flange	**Node Set**	**T1**	**T2**	**T3**	**T4**	**T5**		
	Initial Temp. (°C)	0	0	0	0	0		
	Final Temp. (°C)	96	48	0	48	96		
Web	**Node Set**	**W1**	**W2**	**W3**	**W4**	**W5**	**W6**	**W7**
	Initial Temp. (°C)	0	0	0	0	0	0	0
	Final Temp. (°C)	24	48	72	96	72	48	24
Bottom Flange	**Node Set**	**B1**	**B2**	**B3**	**B4**	**B5**		
	Initial Temp. (°C)	0	0	0	0	0		
	Final Temp. (°C)	96	48	0	48	96		

Table 5.4 Material models for Class 1 and Class 2 specimens

Class 1 Sections (W250X67)		**Class 1 Sections (W250X67)**	
True Stress (MPa)	**Logarithmic Strain**	**True Stress (MPa)**	**Logarithmic Strain**
297.4	0	304.9	0
302.5	0.0172	308.8	0.0126
359.8	0.0317	391.9	0.0342
429.3	0.0786	453.3	0.0671
448.3	0.0871	489.8	0.1073
489.9	0.1474	511.7	0.1397

Table 5.5 Piece-wise linear spring stiffnesses used in FEA models

Analysis #1		Analysis #2		Analysis #3		Analysis #4		Analysis #5	
Force (kN)	**Disp. (mm)**	**Force (kN)**	**Disp. (mm)**	**Force (kN)**	**Disp. (mm)**	**Force (kN)**	**Disp. (mm)**	**Force (kN)**	**Disp. (mm)**
0	0	0	0	0	0	0	0	0	0
2.6	0.4	2.0	0.12	8.4	5.7	3.5	0.8	44.2	0.7
5.7	1.1	11.3	5.4	28.6	24.4	17.9	22.6	13.3	11.1
10.4	3.0	18.8	14.5	51.3	47.2	26.0	36.8	20.6	20.4
15.7	6.1	23.3	20.6					26.1	28.9
19.1	8.6	30.8	31.0						
22.1	11.4	33.9	35.0						
25.8	15.1								
30.4	20.0								

Table 5.6 Piece-wise linear load path used in the Class 2 FEA models

Test #4		Test #5		Test #6	
Moment (kN × m)	**Torque (kN × m)**	**Moment (kN × m)**	**Torque (kN × m)**	**Moment (kN × m)**	**Torque (kN × m)**
17.0	**3.86**	**157**	**16.5**	**146**	**16.9**
44.4	**11.3**	**190.5**	**22.5**	**161**	**19.6**
61.8	**15.2**			**188**	**28.3**
81.4	**19.5**				
92.4	**22.3**				
108	**27.2**				
138	**35.5**				

Table 5.7 Comparison of experimental and predicted capacities

Specimen / Model No.	Max. Bending Moment (kN·m)		Max. Torque (kN·m)		Test/Predicted	
	Test	Predicted	Test	Predicted	Bend. Mom.	Torque
1	117.2	101.0	27.9	23.5	1.16*	1.19*
2	187.0	148.0	23.1	18.3	1.26	1.26
3	242.5	222.0	16.9	14.8	1.09	1.14
4	122.9	122.7	31.8	31.2	1.00*	1.02*
5	190.6	176.8	24.3	20.1	1.08	1.21
6	178.8	164.8	25.4	20.94	1.08	1.21

*Primary torque jacks ran out of stroke before any reduction in load carrying capcity.

Table 5.8 Comparison of experimental and predicted initial linear response

Specimen / Model No.	Initial Slope of Moment Ratio vs. Deflection Curve (1/mm)		Test/Predicted
	Test	Predicted	
1	0.0578	0.0535	1.08
2	0.0557	0.0559	0.996
3	0.0630	0.0587	1.07
4	0.1106	0.0548	2.02
5	0.0585	0.0583	1.00
6	0.0598	0.0582	1.03

Table 5.9 Parametric study

Analysis No.	Corresponding Test Specimen	Class	Initial B.M/Torque Ratio	Span (m)	Braced / Unbraced
7	1	1	5:1	4	Braced
8	1	1	5:1	4	Unbraced
9	2	1	10:1	4	Braced
10	2	1	10:1	4	Unbraced
11	3	1	20:1	4	Braced
12	3	1	20:1	4	Unbraced
13	4	2	5:1	4	Braced
14	4	2	5:1	4	Unbraced
15	5	2	10:1	4	Braced
16	6	2	10:1	4	Unbraced

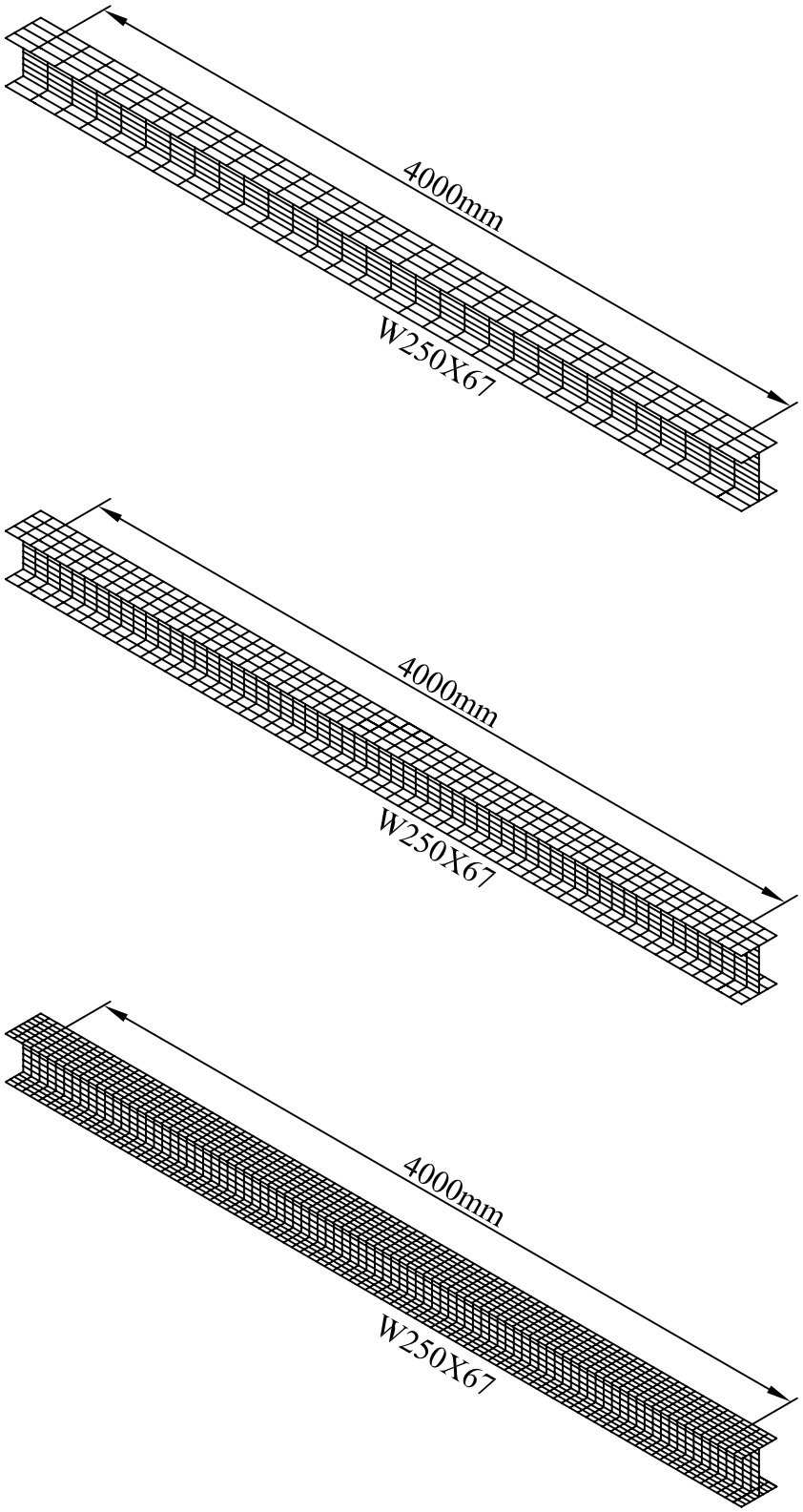

Figure 5.1 Mesh sizes used in mesh refinement study

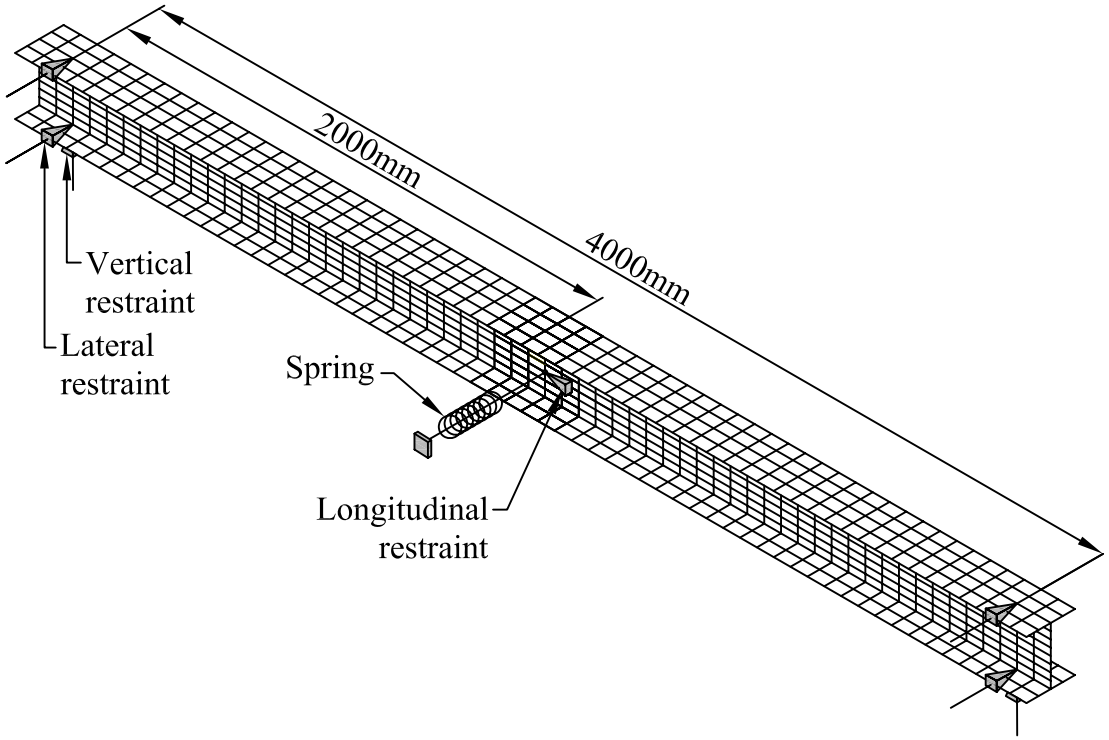

Figure 5.2 Finite element model - boundary conditions

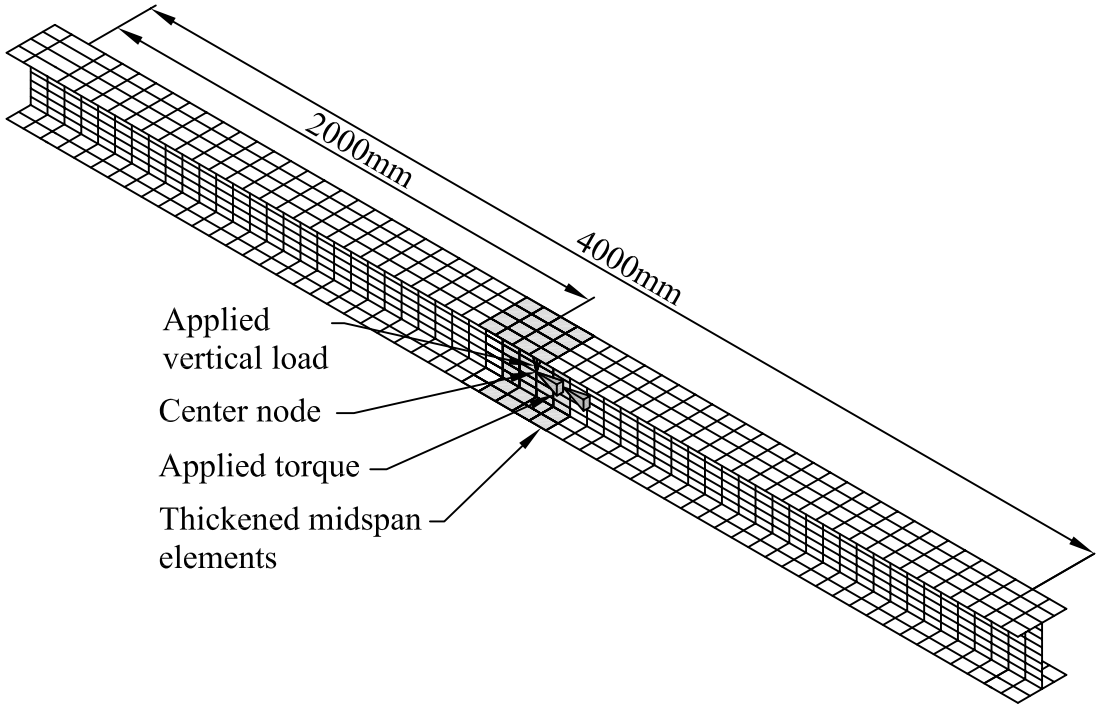

Figure 5.3 Finite element model - location of applied loads

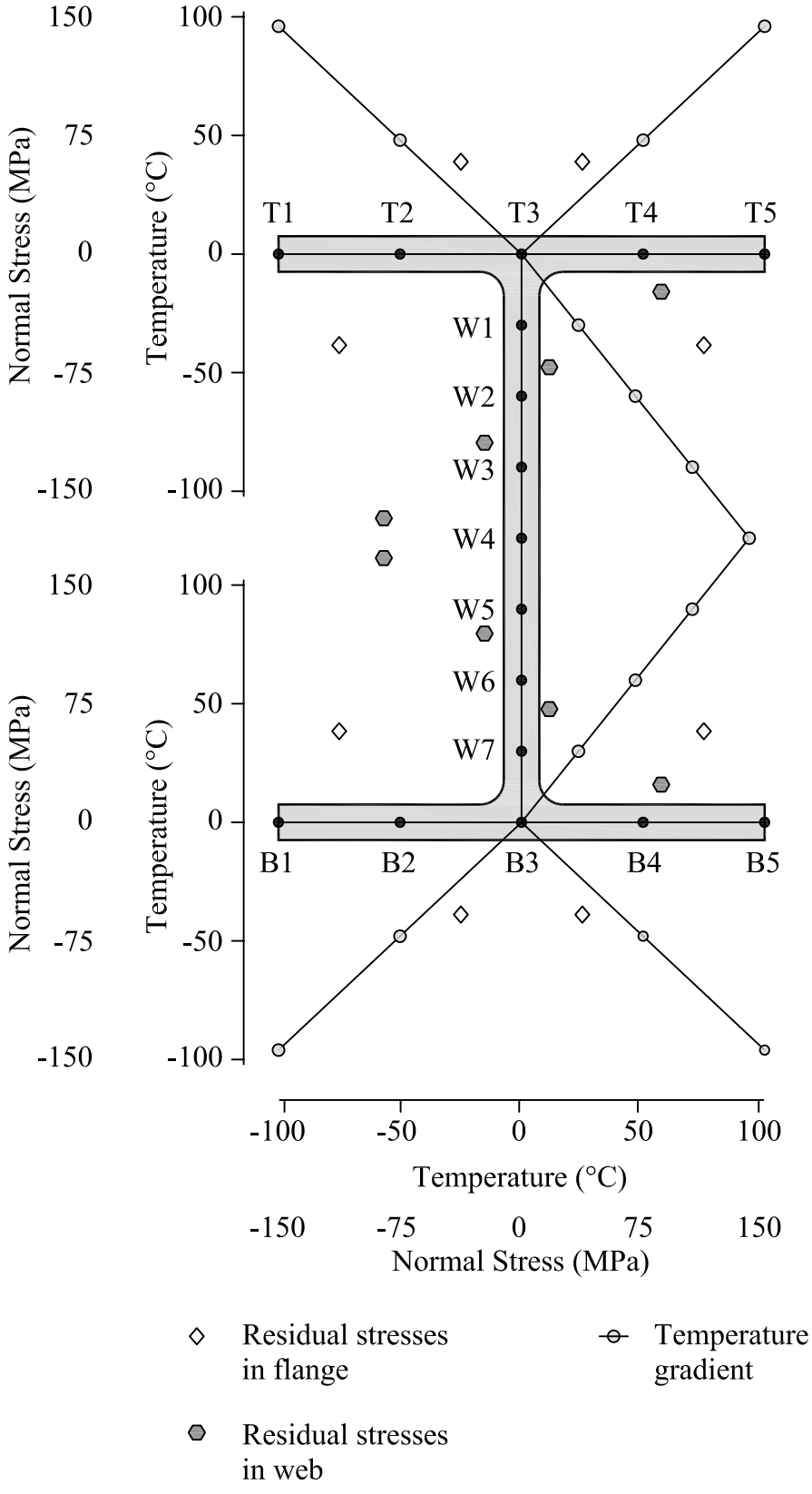

Figure 5.4 Input temperature gradient and resulting residual stress pattern

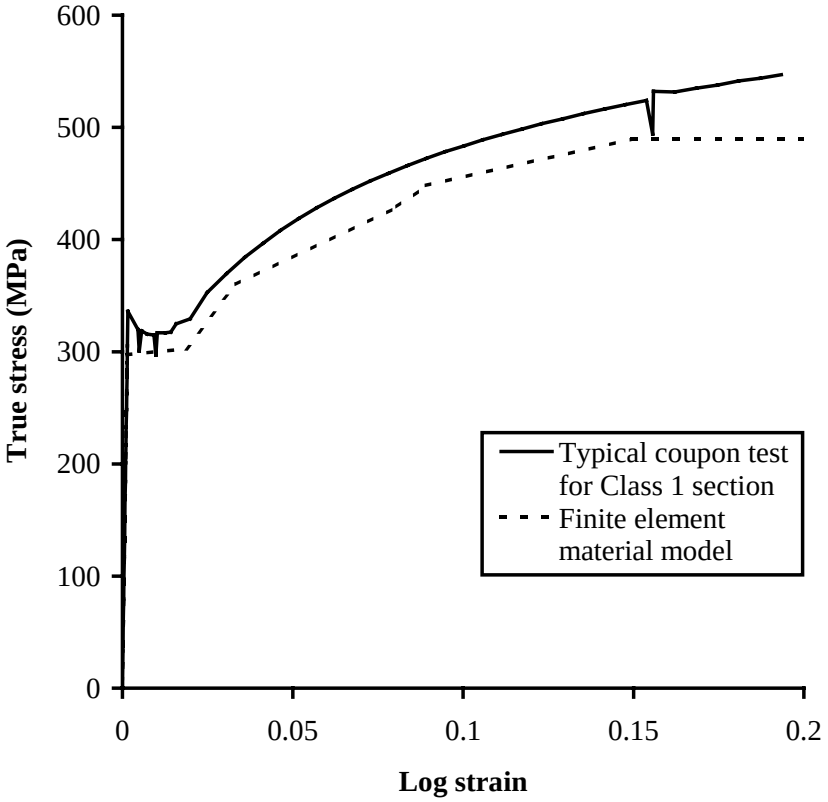

Figure 5.5 Material model for Class 1 section

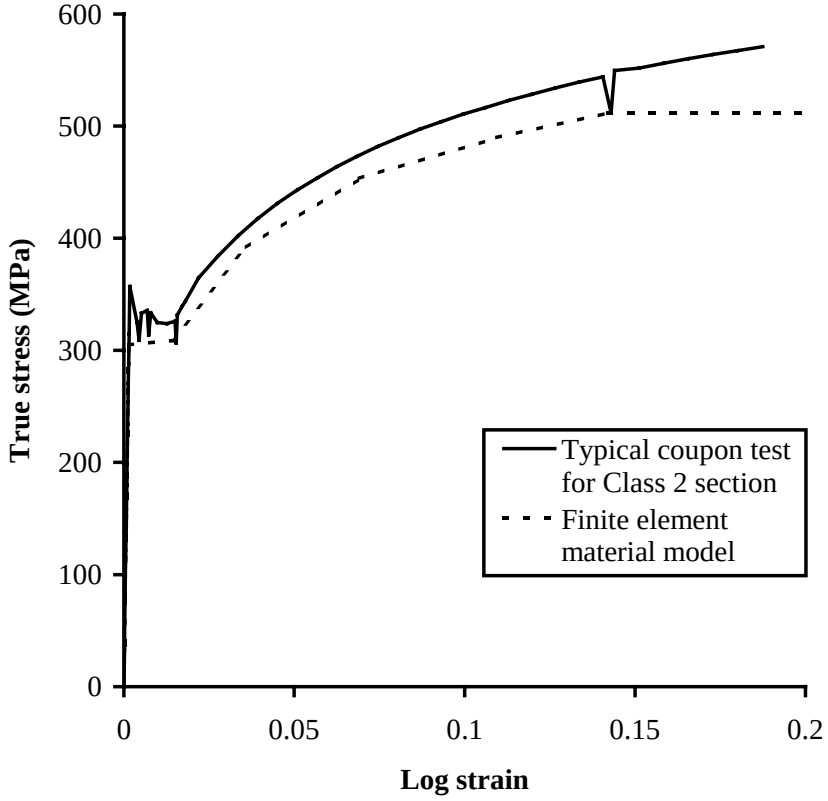

Figure 5.6 Material model for Class 2 section

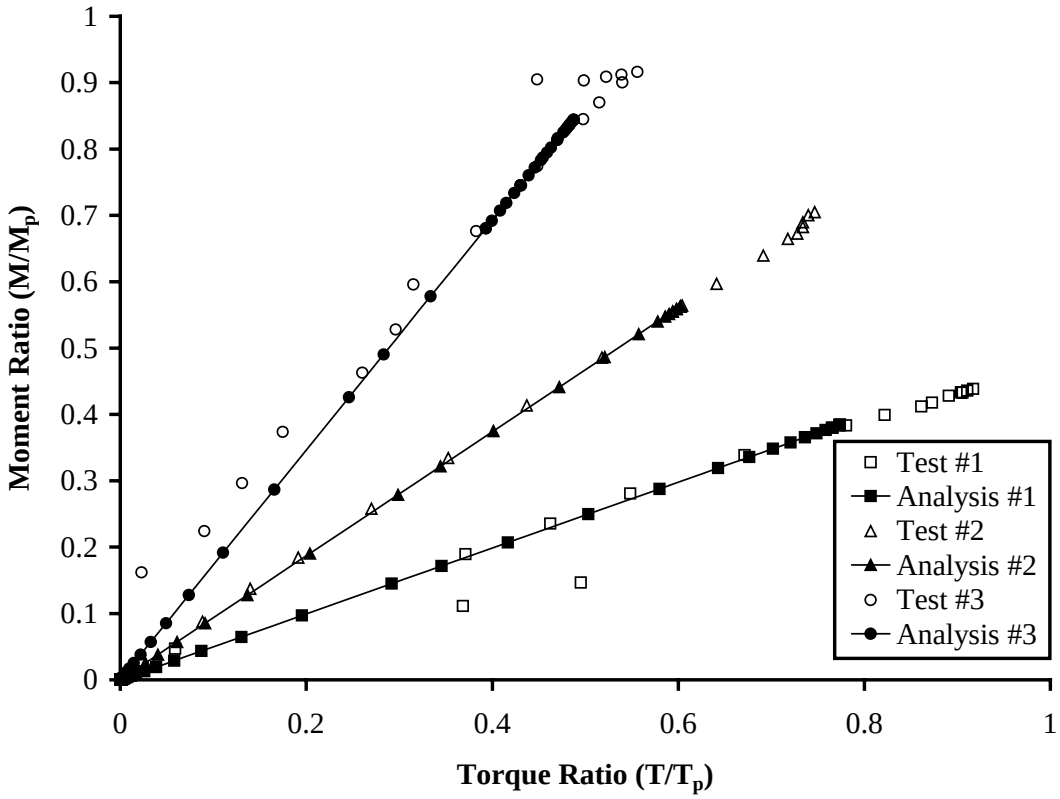

Figure 5.7 Bending moment-torque relationship - Class 1 specimens

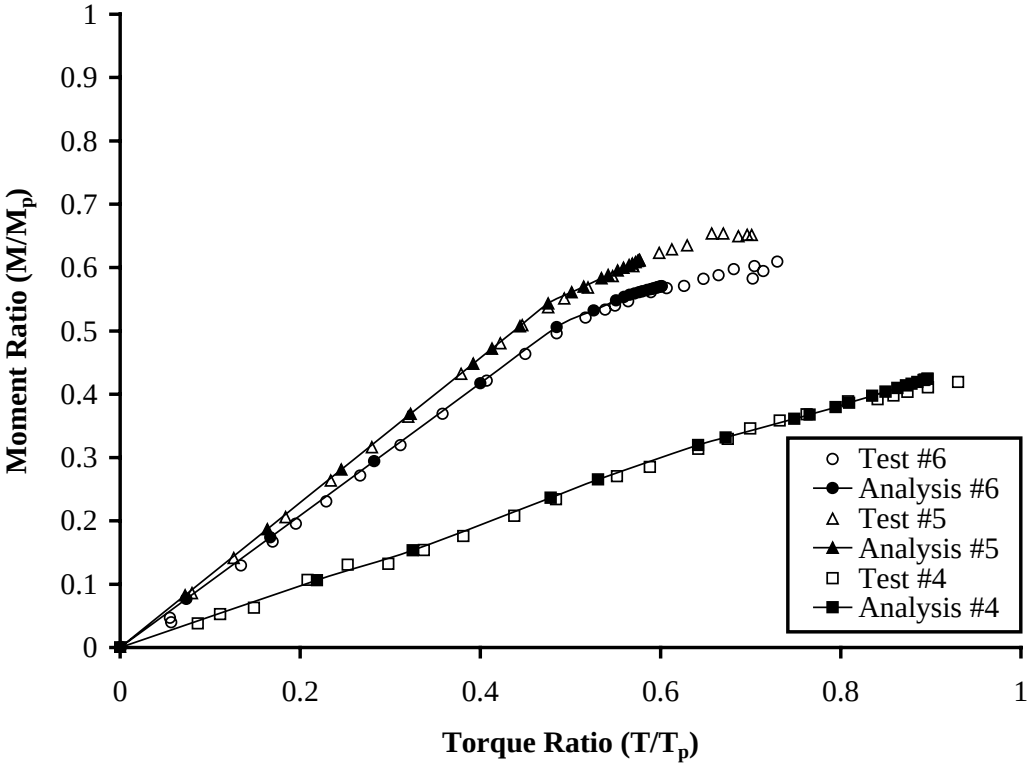

Figure 5.8 Bending moment-torque relationship Class 2 specimens

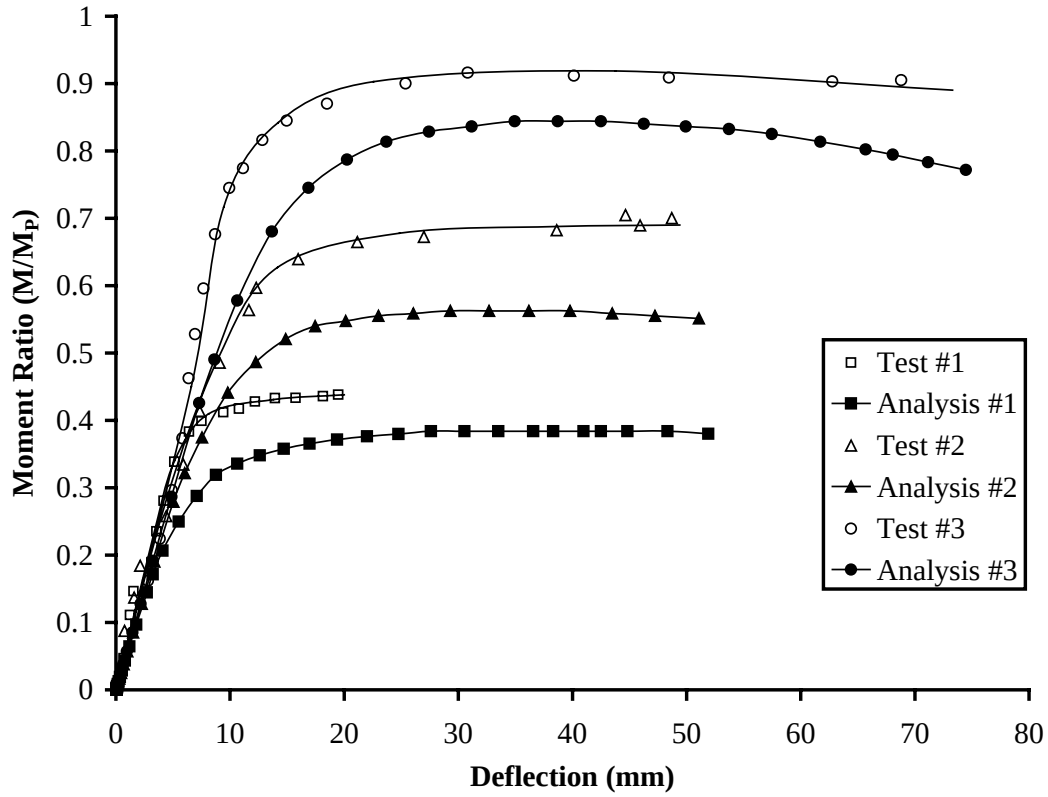

Figure 5.9 Bending moment-deflection relationship - Class 1 specimens

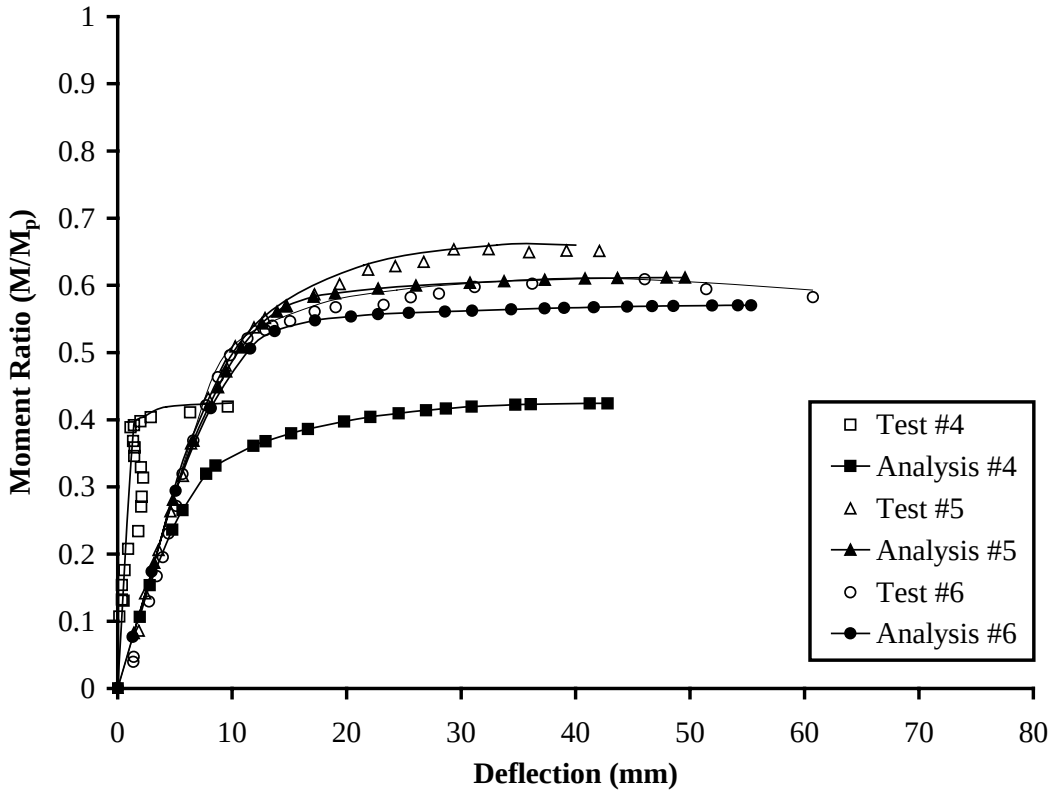

Figure 5.10 Bending moment-deflection relationship - Class 2 specimens

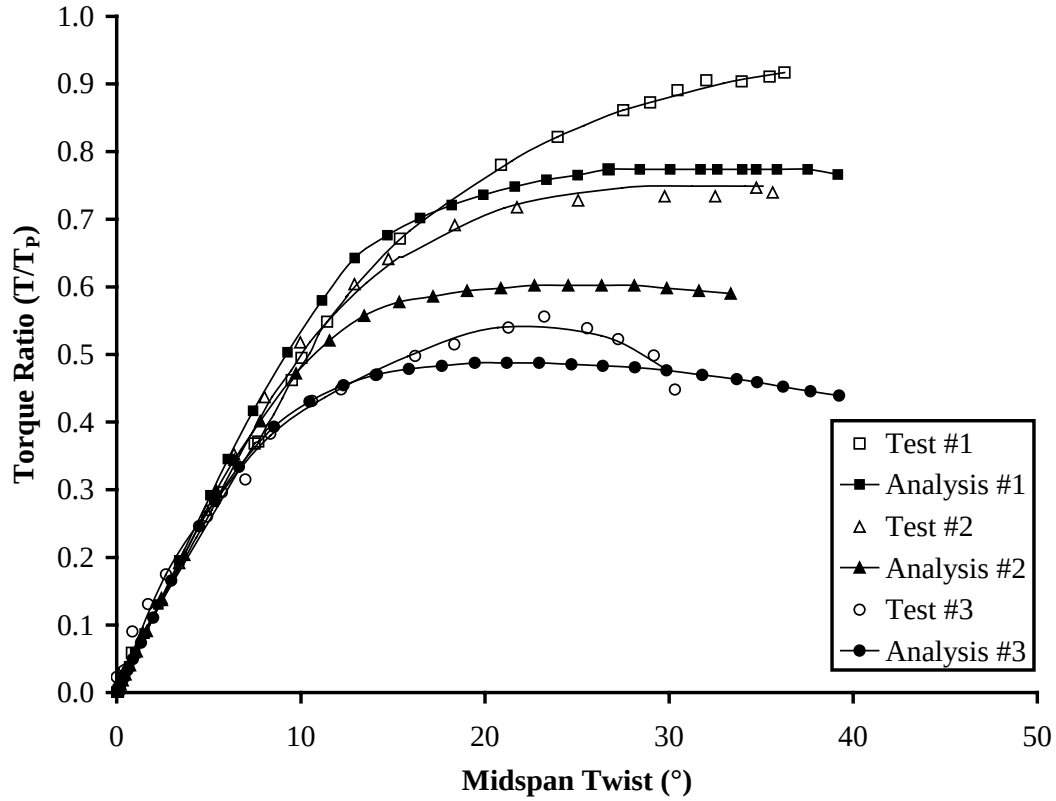

Figure 5.11 Torque-midspan twist relationship - Class 1 specimens

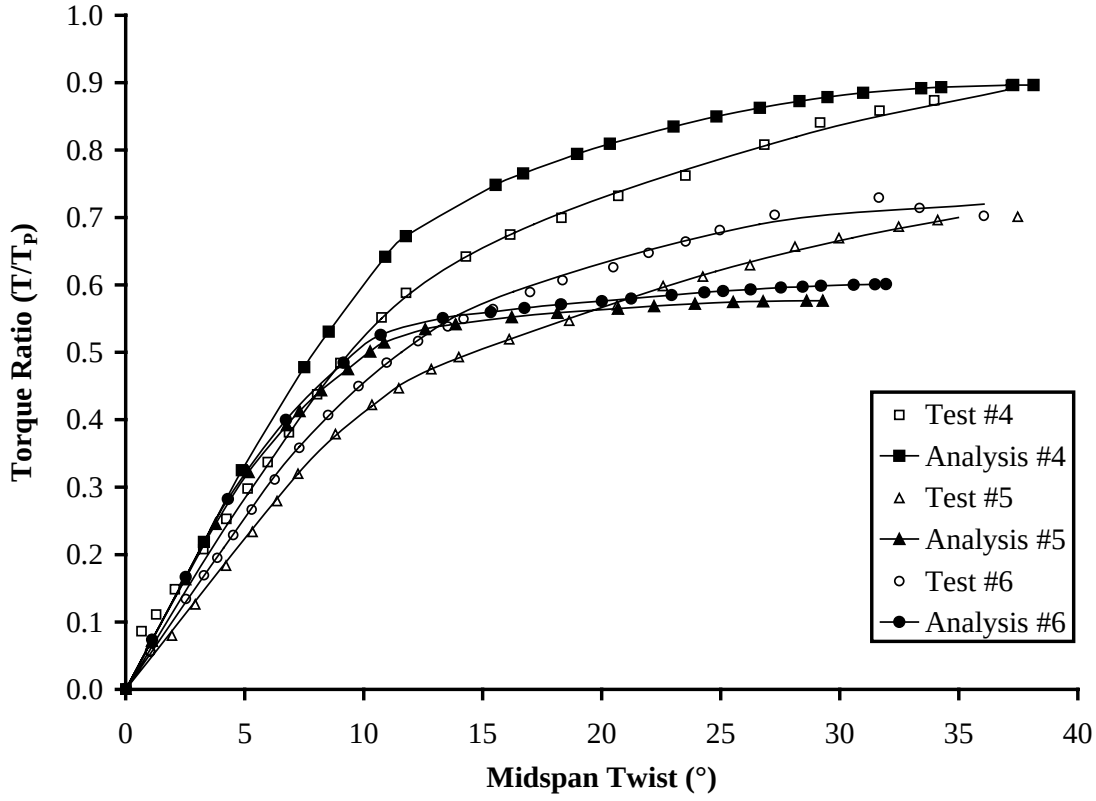

Figure 5.12 Torque-midspan twist relationship - Class 2 specimens

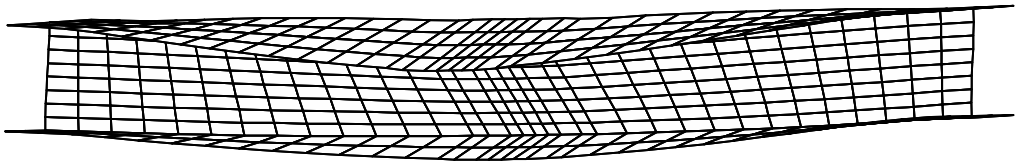

Analysis 2

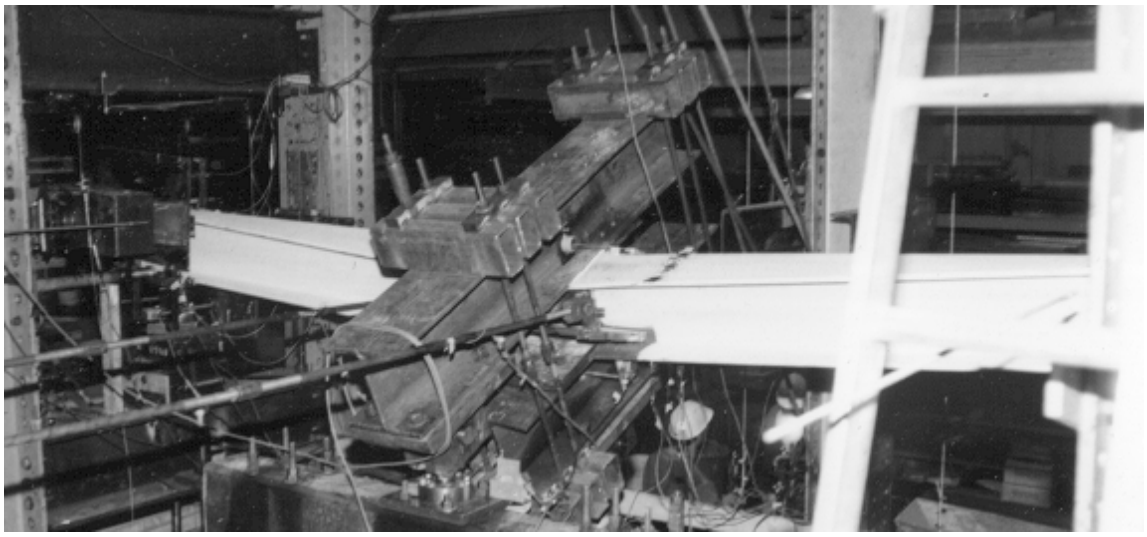

Test specimen 2

Figure 5.13 Deformed finite element model and deformed test specimen

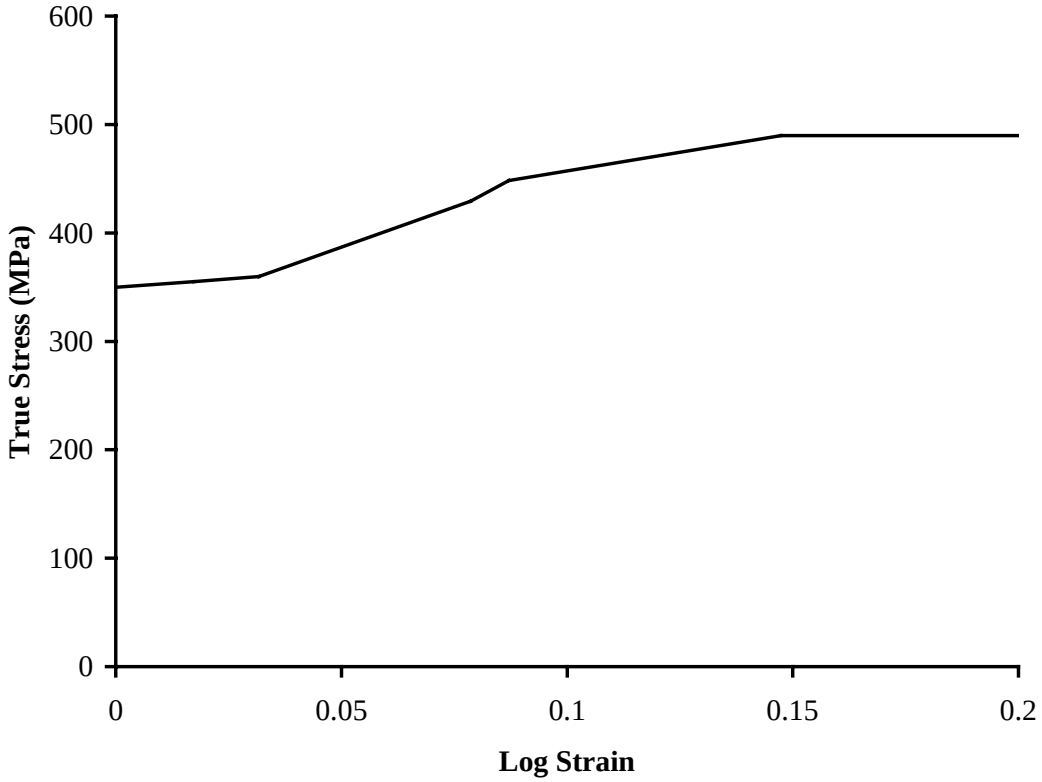

Figure 5.14 Finite element material model for F_y = 350MPa

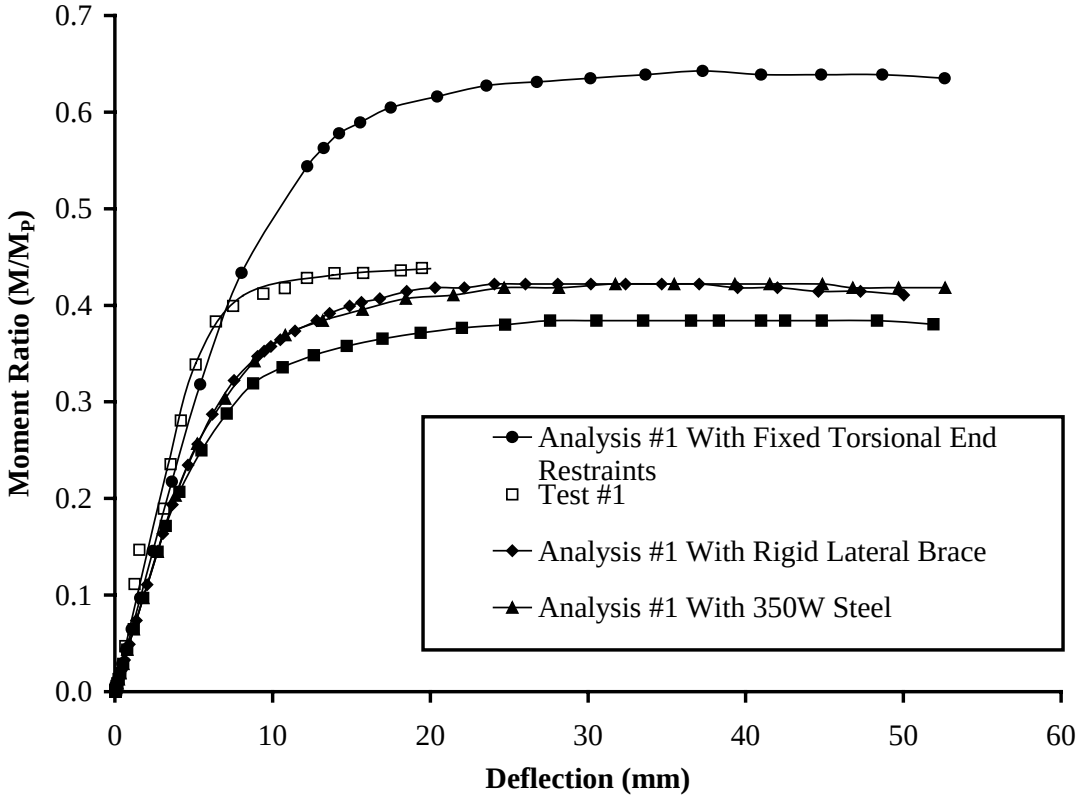

Figure 5.15 Sensitivity of bending moment-deflection relationship

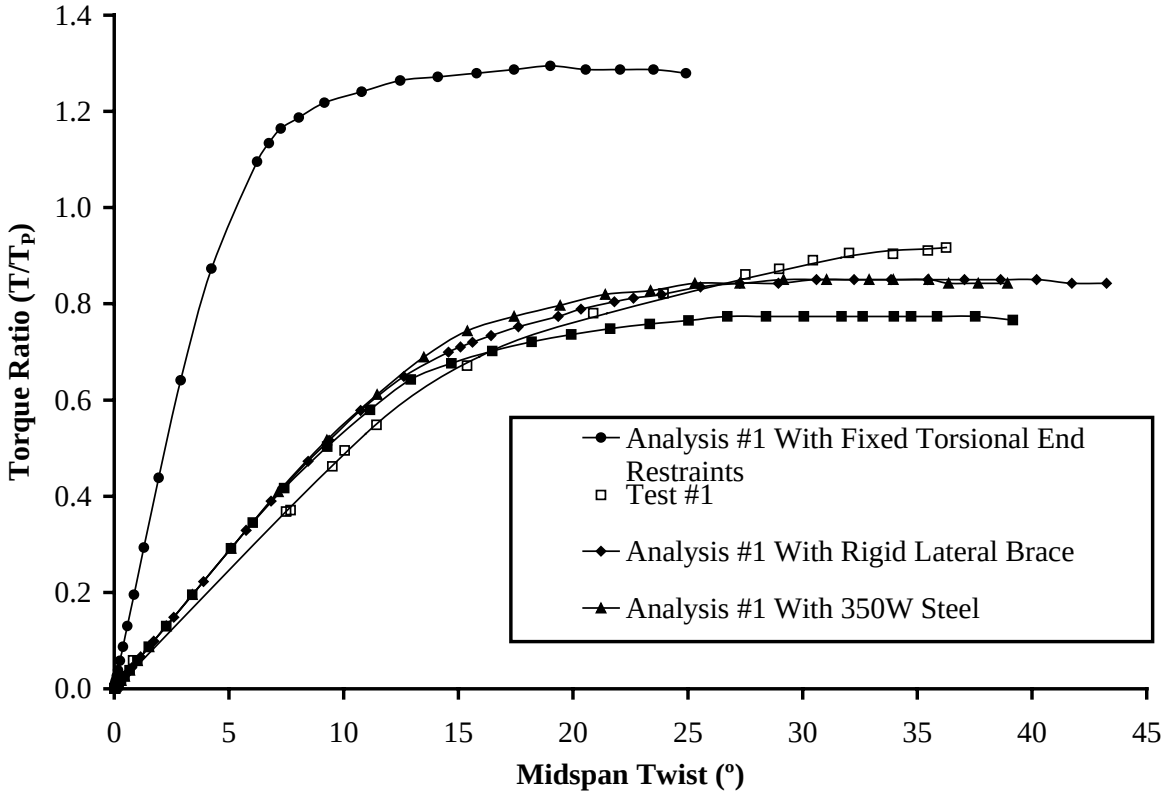

Figure 5.16 Sensitivity of torque-midspan twist relationship

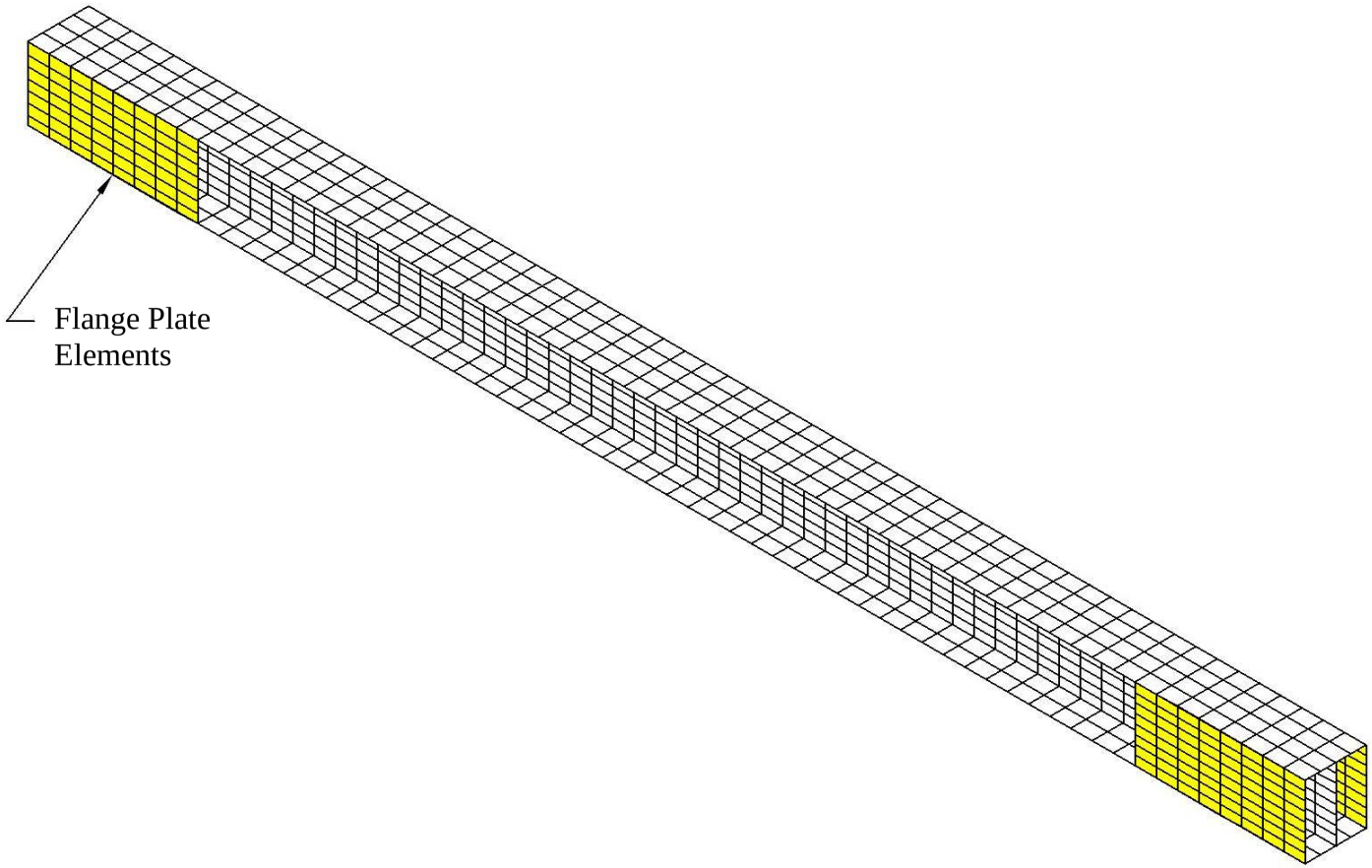

Figure 5.17 Finite element model with fixed warping end restraints

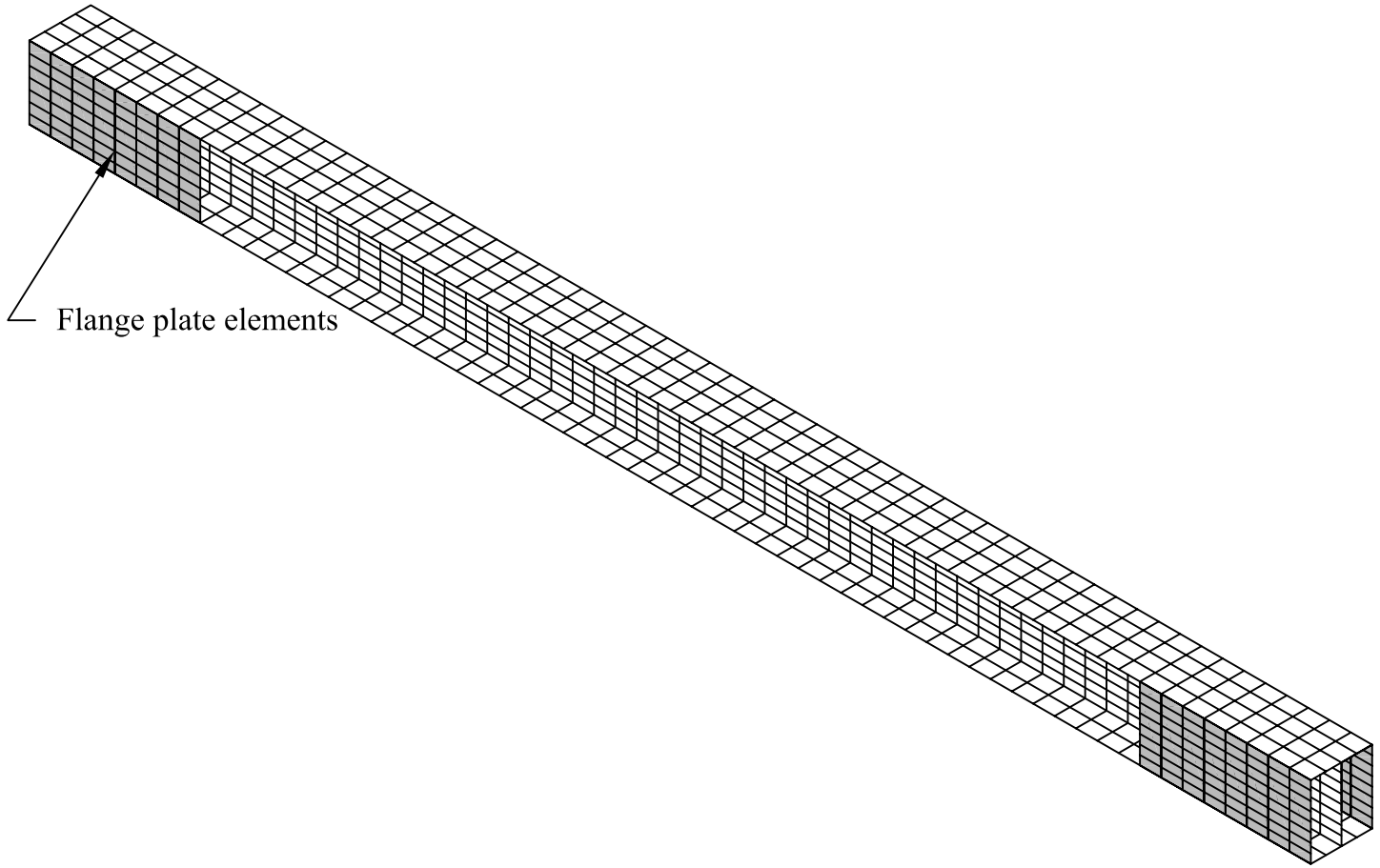

Figure 5.17 Finite element model with fixed torsional end restraints

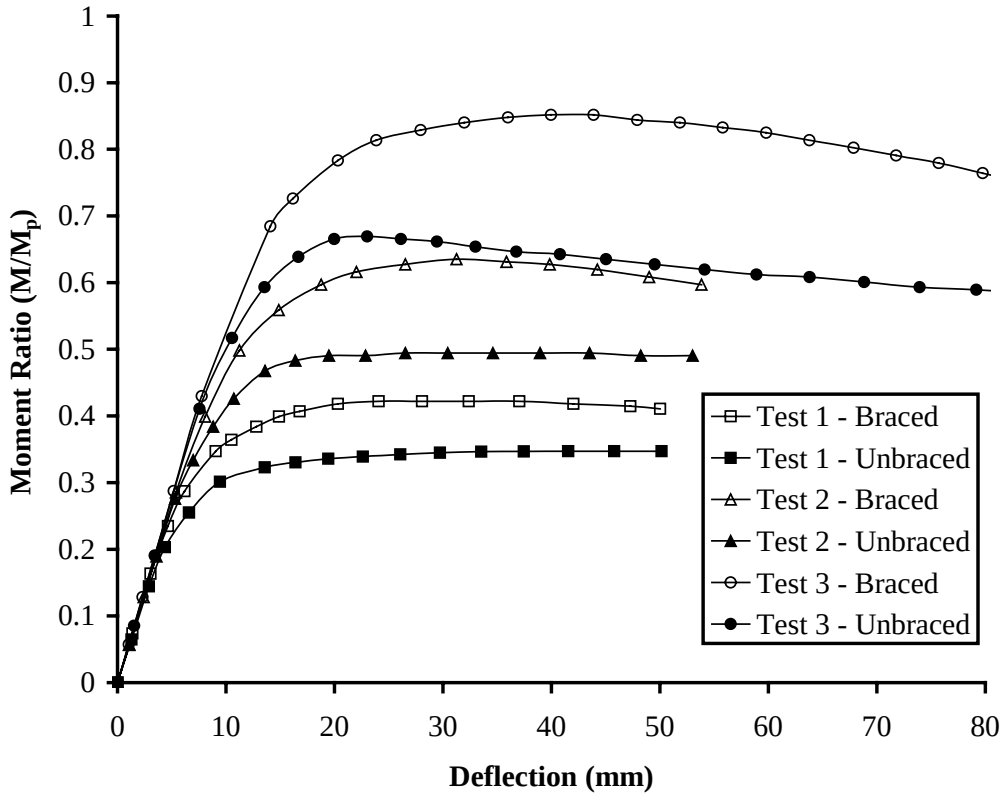

Figure 5.18 Parametric study – moment-deflection relationship - Class 1 specimens

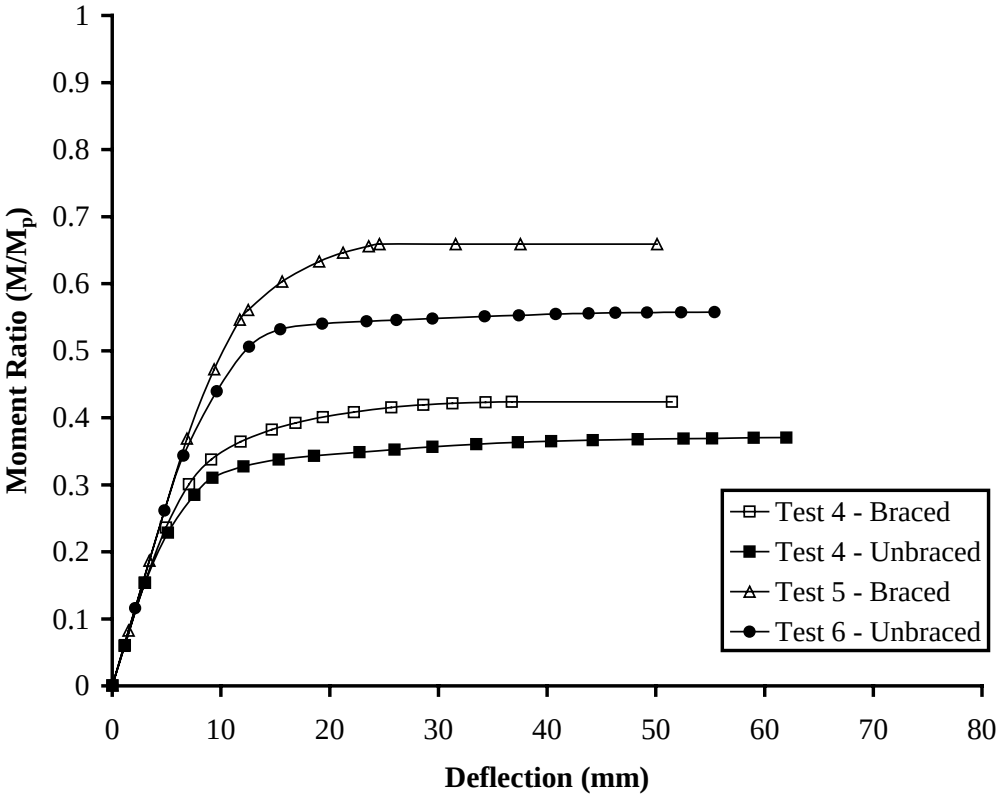

Figure 5.19 Parametric study – moment-deflection relationship - Class 2 specimens

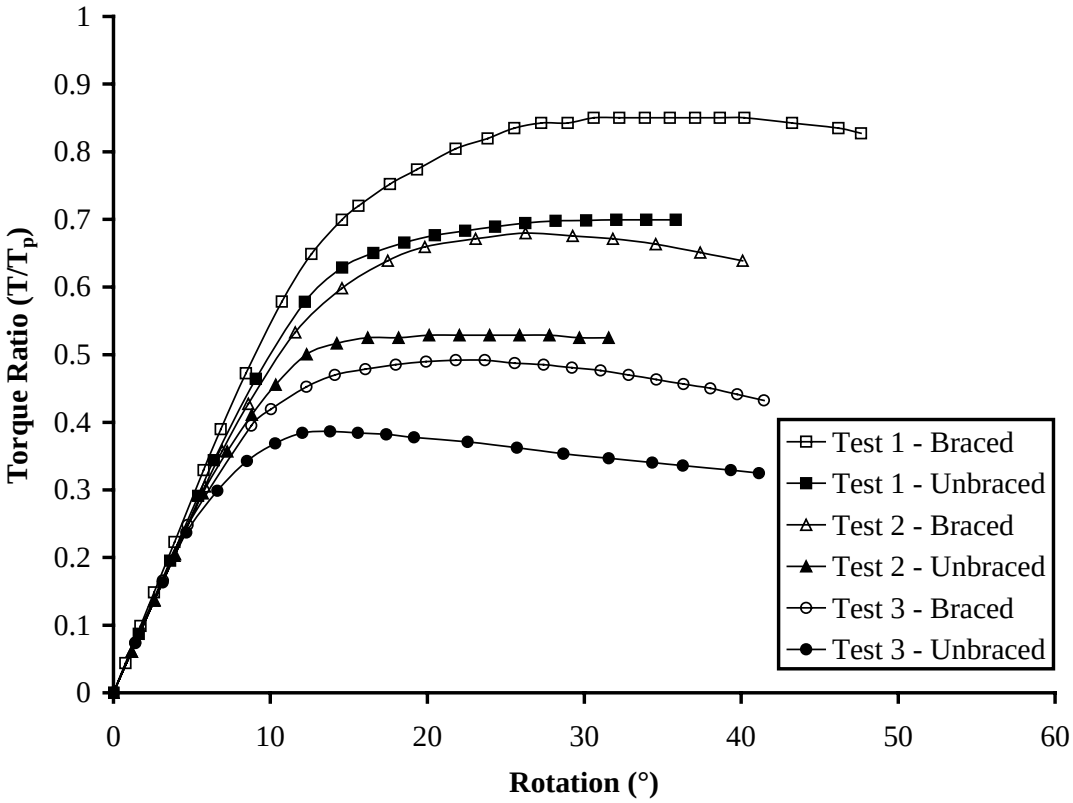

Figure 5.20 Parametric study – torque-rotation relationship - Class 1 specimens

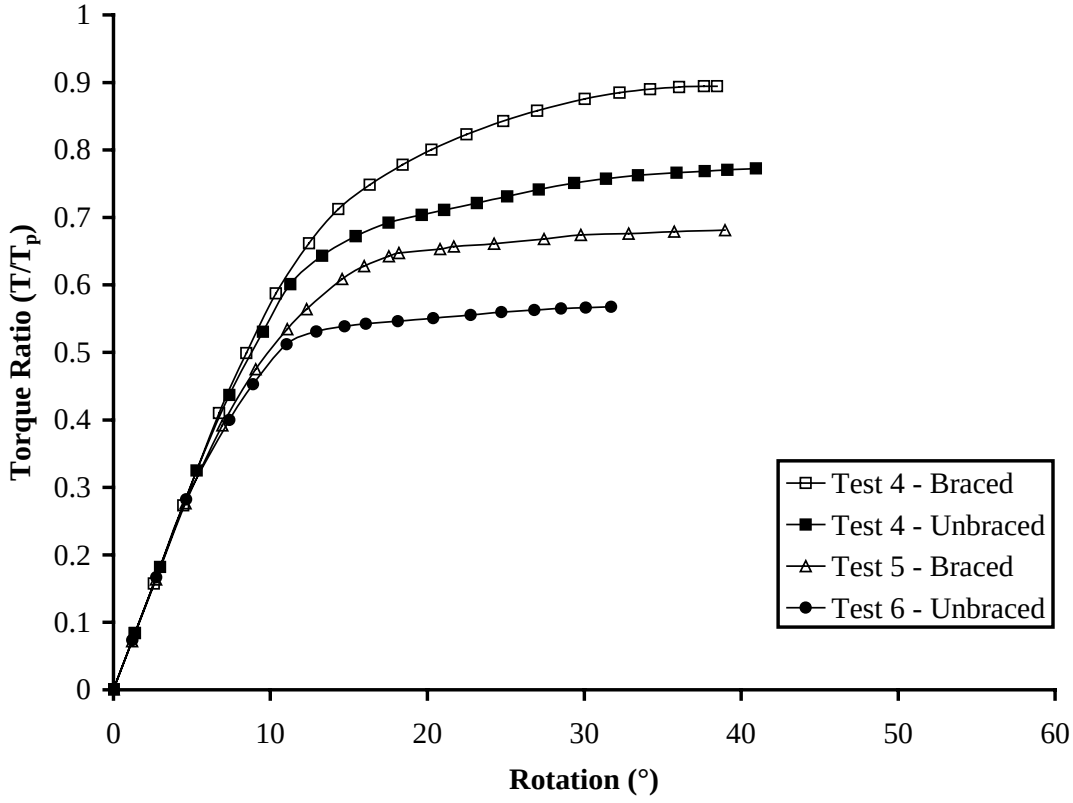

Figure 5.21 Parametric study – torque-rotation relationship - Class 2 specimens

6. Discussion

6.1 General

This chapter examines both elastic and inelastic design methods and compares the beam capacities predicted using these methods to the capacities determined from both the laboratory tests and from the finite element analysis. The limitations of each design method are discussed. Bending and torsion interaction curves are also developed using the results of the finite element analysis. The calculations required to develop the interaction curves shown in this chapter are provided in Appendix C.

6.2 Elastic Design

The material properties obtained from the coupon tests and the measured cross-sectional properties were used to plot the first yield design equation. Figure 6.1 compares the first yield design and the LRFD design, incorporating the reduction factor based on work by Chu and Johnson (1974), to the Class 1 test results. The same comparison for the Class 2 beams is shown in Figure 6.2. Figures 6.1 and 6.2 show that there is much reserve capacity beyond the first yield. It is evident that, for the tested beams, the additional conservatism employed by Chu and Johnson (1974) and the LRDF standard is not necessary from a strength point of view. However, for slender sections the concerns of premature failure by lateral-torsional buckling may be warranted.

It should be noted that typically it is not possible to utilize the reserve capacity beyond first yield because the service requirements of the member cannot accommodate the rotations associated with higher torsional loads. In fact, rotations should still be checked if the service loads fall with the first yield design envelope.

6.3 Driver and Kennedy (1989)

Driver and Kennedy (1989) proposed a limit states design approach for combined bending and torsion. Interaction diagrams were developed for both ultimate and

serviceability limit states. For Class 1 sections the ultimate limit states interaction diagram was based on an idealized fully plastic stress distribution where the maximum normal stress due to bending and warping is limited to the ultimate tensile strength. According to S16-01 Clause 13.6 the flexural capacity of the tested Class 1 beams is limited by lateral-torsional buckling. For this case, Driver and Kennedy proposed that the ultimate limit states interaction curve be based on a maximum moment corresponding to the lateral-torsional-buckling moment resistance and a maximum torque equal to the plastic torque based on the yield strength rather than the ultimate tensile strength (Driver and Kennedy, 1989).

The material properties obtained from the coupon tests and the measured cross-sectional properties were used to determine the ultimate limit states interaction diagram for the tested Class 1 sections. A comparison between the test results and the predicted interaction curve is presented in Figure 6.3. Figure 6.3 shows that Driver and Kennedy's (1989) ultimate limit states interaction diagram predicts the capacity of the tested Class 1 beams to within ± 3%. However it is worth noting that, since the compression flanges of the tested beams were unbraced, the ultimate limit states interaction diagram shown in Figure 6.3 was determined using the lateral-torsional-buckling moment resistance. Although the compression flanges were unbraced, lateral deflection of the point of rotation was limited by midspan bracing and the lack of this bracing would further reduce the capacity of the beams. It is possible, that for completely unbraced beams the ultimate limit states diagram proposed by Driver and Kennedy (1989) for Class 1 sections, in which the flexural capacity is governed by lateral torsional buckling, maybe non-conservative.

The ultimate limit states interaction diagram proposed by Driver and Kennedy for the tested Class 2 sections is shown in Figure 6.4. For this case, the maximum bending moment is limited to the plastic moment and the maximum torque is limited to the plastic torque based on the yield strength (Driver and Kennedy, 1989). Figure 6.4 shows that the ultimate limit states diagram predicts the capacities of the tested beams to within ± 6%.

Despite the fact that the Driver and Kennedy model does quite accurately predict the capacity of the tested beams there are some deficiencies in their approach to combined bending and torsion. Driver and Kennedy recognized that the presence of

warping normal stresses reduce the moment capacity of a beam subjected to combined bending and torsion. However, the capacity envelope in their moment-torque interaction diagrams extends horizontally from the strong-axis moment capacity of the beam to the St. Venant torque and reduction in the moment capacity is only assumed to occur once the St. Venant torque has been exceeded. The rationale is that the St. Venant torque only results in shear stresses and does not reduce the beam's moment capacity and that the warping normal stresses will only occur after the St. Venant torque has been exceeded. Warping torsion does not develop only subsequent to the St. Venant torque, but rather warping and pure torque develop simultaneously and the proportion of each component is dependent on the level of warping restraint at the critical section. For the tested beams the maximum torque and maximum moment both occurred at midspan. Because of the loading condition imposed on the test specimens, warping was restrained at midspan and strain gauges mounted at the flange tips near the critical section indicated that the onset of warping normal stresses were coincident with the start of torsional loading.

The Driver and Kennedy (1989) ultimate limit states interaction diagram also does not adequately deal with lateral-torsional buckling. The Driver and Kennedy (1989) model reduces the moment capacity in accordance to S16-01 Clause 13.6 to the lateral-torsional-buckling moment, but fails to consider the destabilizing effects of an applied torsional load. It is expected that torsional moments will amplify both rotations and lateral deflections, thereby reducing the buckling moment.

The formulation proposed by Driver and Kennedy (1989) does not take into consideration the reduced strength of the rotated section. A beam subjected to combined bending and torsion will experience bi-axial bending as the cross-section rotates. Since the applied moment has a component acting about the weak axis, the moment capacity of the beam will be less than the strong-axis moment capacity.

Considering the presence of warping normal stresses at the onset of torsional loading, the destabilizing effects of an applied torsional load, and the reduced strength of a rotated I-shaped beam, the horizontal line in Driver and Kennedy's (1989) model extending out from the moment capacity of the beam to the St. Venant torque is flawed. All of these factors will act to reduce the moment capacity of an I-shaped beam subjected to torsion and the horizontal line in Driver and Kennedy's (1989) equation should in fact

have a negative slope. This equation is potentially non-conservative particularly at high moment-to-torque ratios and should not be used for design.

6.4 Pi and Trahair

The problem of combined bending and torsion has been studied extensively by Pi and Trahair. In 1993, they investigated the interaction effects of combined bending and torsion using a large deformation, inelastic, finite element model. Both initial imperfections and residual stresses were included in the finite element formulation. The following equation describes the lower bound interaction of their finite element analysis for an I-shaped beam centrally braced at the shear center (the terms of the equation are defined in Chapter 2).

$$\left(\frac{PL}{4M_p}\right)+\left(\frac{Pe}{2T_p}\right)=1 \qquad [6.1]$$

The measured material and cross-sectional properties were used to plot this interaction equation for the tested Class 1 and Class 2 beams. This equation is compared to the combined bending and torsion test results in Figure 6.5 for the Class 1 beams and in Figure 6.6 for the Class 2 beams. Figure 6.5 and Figure 6.6 show that the Pi and Trahair (1993) equation conservatively predicts the capacity of the tested beams.

In 1994, Pi and Trahair (1994a) developed a design approach for torsion that accounted for the section class. They proposed that the same local buckling classifications, which are used for bending design, also be used for torsion design. A plastic torsion design was proposed for Class 1 sections, which they considered to have sufficient ductility and rotation capacity to allow the plastic collapse mechanism to fully develop. For Class 2 sections, a first hinge design was proposed. Pi and Trahair (1994) also suggested that torsion design for Class 3 sections be based on a first yield design and Class 4 sections be designed for torsion using a local buckling design.

Pi and Trahair (1994a) extended their torsion design approach to deal with combined bending and torsion and proposed two interaction equations. For Class 1

sections they proposed that the plastic-collapse load factors be determined independently for both bending and torsion. The following circular interaction equation was proposed to account for interaction effects.

$$\lambda_{ip}^{\ 2} + \lambda_{tp}^{\ 2} \leq 1 \qquad [6.2]$$

where, λ_{ip} is the plastic collapse load factor for in-plane bending, and
λ_{tp} is the plastic collapse load factor for torsion.

For the remaining section classes, the appropriate torsion design is used to determine the torsion capacity. The torsion and moment design capacities are then used in the following linear interaction equation to account for interaction effects.

$$\frac{M}{M_r} + \frac{T}{T_r} \leq 1 \qquad [6.3]$$

where, M is the applied in-plane bending moment,
T is the applied torque,
M_r is the moment resistance of the beam accounting for lateral buckling, and
T_r is the torsion capacity of the beam dependent on section class.

The torsion and bending plastic collapse load factors were used to plot equation 6.2 for the Class 1 beams tested in the present program. Figure 6.7 shows that the Pi and Trahair's interaction diagram based on plastic collapse accurately predicts the capacity of the tested Class 1 beams.

Pi and Trahair's (1994a) interaction equation is an adaptation of work originally performed by Hodge (1959). Hodge (1959) proposed a plastic analysis for the case of combined bending and uniform torsion and Dinno and Merchant (1965) later extended Hodge's circular interaction diagram to cover combined bending and non-uniform torsion. For the case of combined bending and non-uniform torsion, Driver and Kennedy (1989) claim that this circular interaction equation is an upper bound solution, since it fails to account for warping normal stresses. Pi and Trahair (1994a) acknowledge that the summation of independent plastic collapse load factors is not rigorous, but claim it is still conservative because it neglects the strengthening effects of Wagner stresses and

strain hardening. Although the theoretical moment capacity of the tested Class 1 beams is slightly less than the plastic moment because of lateral-torsional buckling, the Class 1 test results still lie outside the circular interaction curve in support of Pi and Trahair's claim. Clearly, however, this equation should not be used for Class 1 beams whose moment capacity is governed by lateral-torsional buckling. The moment capacity of the tested Class 1 beams was only slightly reduced because of lateral-torsional buckling and the capacities of beams more susceptible to this type of failure will lie within the predicted interaction equation.

The measured cross sectional properties were used to calculate the torsional capacity based on a first hinge analysis for the tested Class 2 specimens. Figure 6.8 compares the linear interaction diagram based on Pi and Trahair's equation 6.3 to the test results for the Class 2 beams. Equation 6.3 conservatively predicts the capacity of the tested Class 2 sections.

6.5 Finite Element Analysis

The bending and torsion interaction behavior was predicted using finite element models for both the Class 1 and Class 2 beams. The predicted interaction behavior of both unbraced beams and beams centrally braced at the point of rotation are compared to the test results in Figure 6.9 and Figure 6.10 for the Class 1 and Class 2 beams respectively. All of the tested Class 1 beams were centrally braced at the point of rotation and Figure 6.9 shows that the finite element model conservatively predicts the capacity of the Class 1 beams. Figure 6.10 shows that the capacity of the unbraced Class 2 test specimen exceeds the capacity predicted by the finite element model while the finite element model closely approximates the capacities of the two braced Class 2 beams.

The predicted moment capacity for the braced Class 1 beams shown in Figure 6.9 exceeds the plastic moment by approximately 20%. Similarly, Figure 6.10 shows that the moment capacity predicted for the braced Class 2 beams exceeds the plastic moment by approximately 20%. The material model used in the finite element analysis took into account both strain hardening and residual stresses (see Chapter 5). The calculated

moment capacities for both the Class 1 and Class 2 beams assumed the beams to be unbraced and were based on the yield strength of the material. The additional moment capacity can be largely attributed to the influence of strain hardening and the midspan brace. The predicted moment capacities of the unbraced beams are much closer to the moment capacities calculated using S16-01.

The finite element analysis clearly shows the destabilizing effects of the torsional load. Although the midspan brace was located at the point of rotation and the compression flange of the beam was unsupported the brace still had a significant influence on the capacity of the beams. The finite element curves in Figure 6.9 show that the capacity of the Class 1 sections is reduced by 18% when the central brace is removed. A 15% reduction in capacity is shown in Figure 6.10 for the Class 2 beams.

The interaction curves developed from the finite element analysis show a near linear reduction in moment capacity with increasing torque for both the Class 1 and Class 2 unbraced beams. For both sections, the braced beam interaction behavior is characterized by an initially steep reduction in moment capacity followed by a brief decrease in the rate of moment reduction before the curves return near to the original slope. A straight line, however, could be used to reasonably approximate the plotted portion of the finite element interaction curves for both the unbraced and braced beams. It should be noted that beyond the plotted portion the slopes of the interaction curves flatten out and the finite element model was able to resist torques greatly exceeding the plastic torque. This was due in part to strain hardening and Wagner stresses in addition to the fact that a limiting rupture strain was not defined in the finite element material model. This additional torsion capacity is not considered to be useable for structural applications, as the beams will be highly distorted.

The unbraced interaction curves developed from the finite element model are compared to the inelastic interaction equations in Figure 6.11 and Figure 6.12 for the Class 1 and Class 2 beams respectively. Figure 6.11 reveals that the Driver and Kennedy and Pi and Trahair circular interaction curves, which did not consider the destabilizing effects of torsion overestimate the capacity of the unbraced Class 1 beam. However, the linear interaction equation developed by Pi and Trahair (1993), which did consider stability closely approximates the finite element curve.

The linear interaction curve developed by Pi and Trahair also provides a reasonable approximation of the predicted interaction behavior of the unbraced Class 2 beam. The Driver and Kennedy model is shown in Figure 6.12 to highly overestimate the capacity of the unbraced Class 2 beam. The Pi and Trahair interaction equation using a torsional capacity based on a first hinge analysis is shown to conservatively predict the capacity of the Class 2 beams.

6.6 Summary

In this chapter both elastic and inelastic design approaches have been compared to the combined bending and torsion tests conducted on Class 1 and Class 2 beams. The first yield design approach was found to be highly conservative for both section class investigated and reduction factors used by the LRFD to account for interaction effects do not appear to be warranted for strength designs. First yield designs are considered best suited for serviceability design.

The ultimate limit states interaction diagrams proposed by Driver and Kennedy (1989) closely approximated the capacities of the tested Class 1 and Class 2 beams. However, the finite element model indicates that the midspan brace had a significant impact on the capacity of the Class 1 beams and the Driver and Kennedy design approach is potentially non-conservative at high moment-to-torque ratios. The Driver and Kennedy ultimate limit state diagrams fail to adequately account for the destabilizing effects of torsion, the influence of warping normal stresses, and bi-axial bending. Although these shortcomings are somewhat offset by strain hardening, and Wagner stresses this interaction model should be used with caution particularly at high moment-to-torque ratios.

The linear interaction equation based on a finite element analysis by Pi and Trahair (1993) conservatively predicts the capacity of the tested beams. The finite element curves plotted by Pi and Trahair (1993) are in close agreement with the finite element model developed in this study. However, the linear interaction equation is not based on a rigorous mathematical account of the interaction behavior of the beam, but rather represents a simple lower bound approximation. A complete parametric study is

required confirming its applicability for a complete range of slenderness ratios, loading conditions and end conditions before the equation can be confidently used for combined bending and torsion design.

The interaction equations based on section class, which were developed by Pi and Trahair (1994a), also conservatively predict the capacity of the tested beams. However, the circular interaction equation based on plastic collapse has similar shortcomings as the ultimate limit states equations developed by Driver and Kennedy (1989). The circular interaction equation does not accurately account for warping normal stresses, neglects the destabilizing effects of torsion and does not consider the influence of bi-axial bending. The Class 1 test results lie just outside the circular interaction equation and this equation should be expected to overestimate the capacity of unbraced Class 1 beams.

The interaction behavior of combined bending and torsion is complex. A single equation that accurately accounts for the many factors that influence the interaction behavior and yet is applicable for a wide range of sections is not achievable. The Bethlehem Steel Corporation has published a series of charts to describe the elastic behavior of beams under torsion and a series of equations at least as extensive would be required to accurately describe the inelastic behavior of combined bending and torsion.

Researchers have recognized that such a series of equations would prove cumbersome for design and have developed simplified equations approximating this complex problem. However, in striving to accurately describe the interaction behavior several of these simplified equations have been shown to overestimate the capacity of beams subjected to combined bending and torsion. For structural design the necessity of an equation that accurately predicts the inelastic capacity of a beam subjected to combined bending and torsion is debatable. Certainly for low moment-to-torque ratios beams will be highly distorted long before they reach their inelastic capacity that it is hard to imagine an application in which they could still be fit for purpose just prior to failure.

The best option for the development of a simple universal design approach for I-shaped beams subjected to combined bending and torsion is a simple interaction equation that can be shown to be a clear lower bound solution. However, this requires the willingness to sacrifice accuracy in order to ensure conservatism. As beams will most

often be governed by serviceability this is not considered an unfair tradeoff. The linear interaction equation proposed by Pi and Trahair (1993) could potentially be a lower bound solution and could be easily adapted to the Canadian code. This equation could be expressed using nomenclature consistent with S16-01 as:

$$\frac{M_f}{M_r} + \frac{T_f}{T_p} \leq 1 \qquad [6.4]$$

For members with low torsional rigidity this equation may not be conservative. Trahair and Bradford (1991) have described the slenderness of unbraced beams using the following formula:

$$\lambda = \sqrt{\frac{M_p}{M_u}} \qquad [6.5]$$

A slenderness limit could be established beyond which beams could not be designed for combined bending and torsion similar to the KL/r requirements given in S16-01 for compression members. A complete parametric study is obviously required to establish slenderness limits and to confirm that this equation is a lower bound solution before it can be confidently used for combined bending and torsion design.

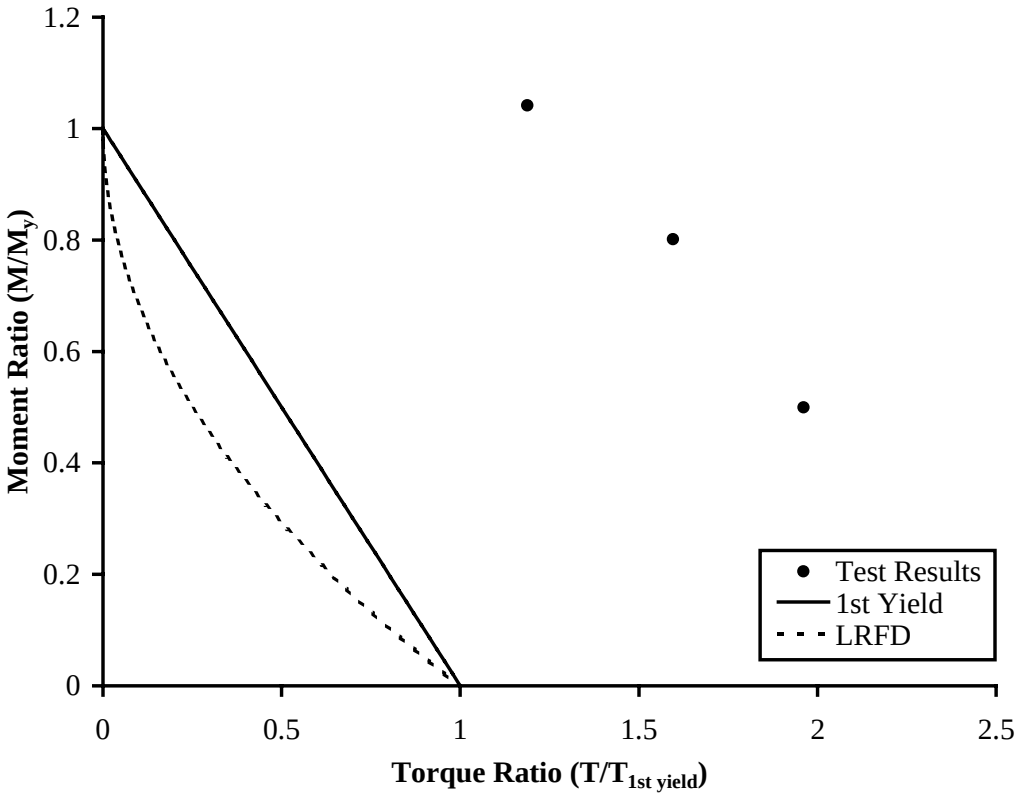

Figure 6.1 Comparison of Class 1 test results to elastic design methods

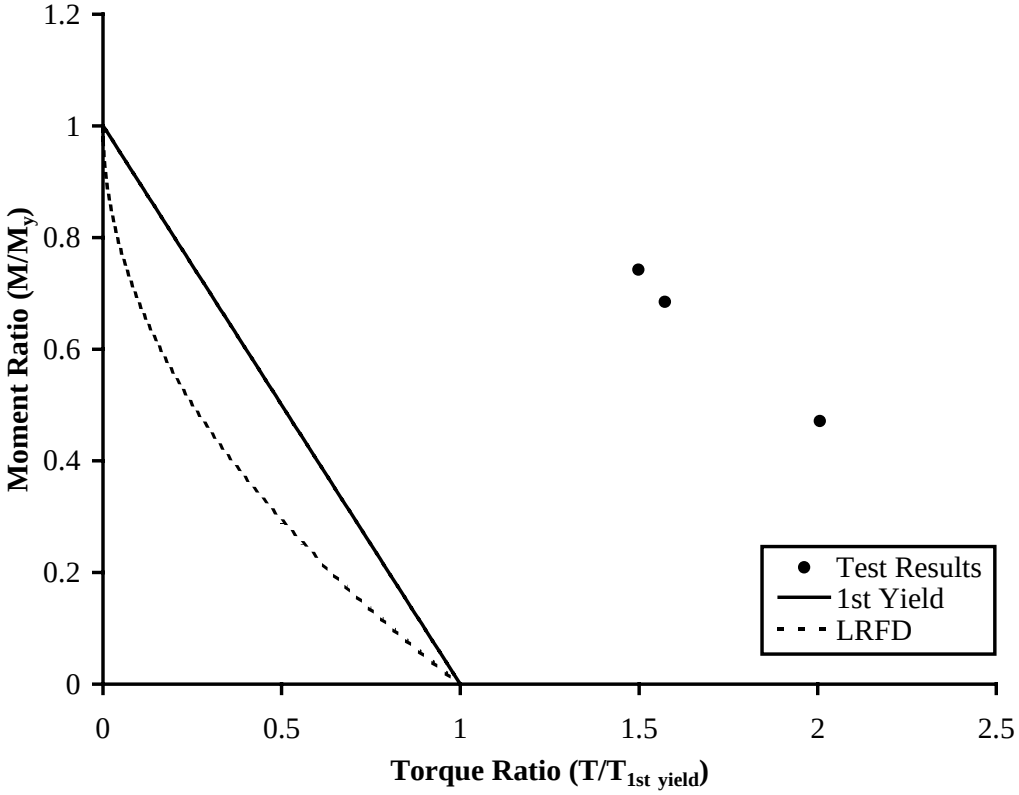

Figure 6.2 Comparison of Class 2 test results to elastic design methods

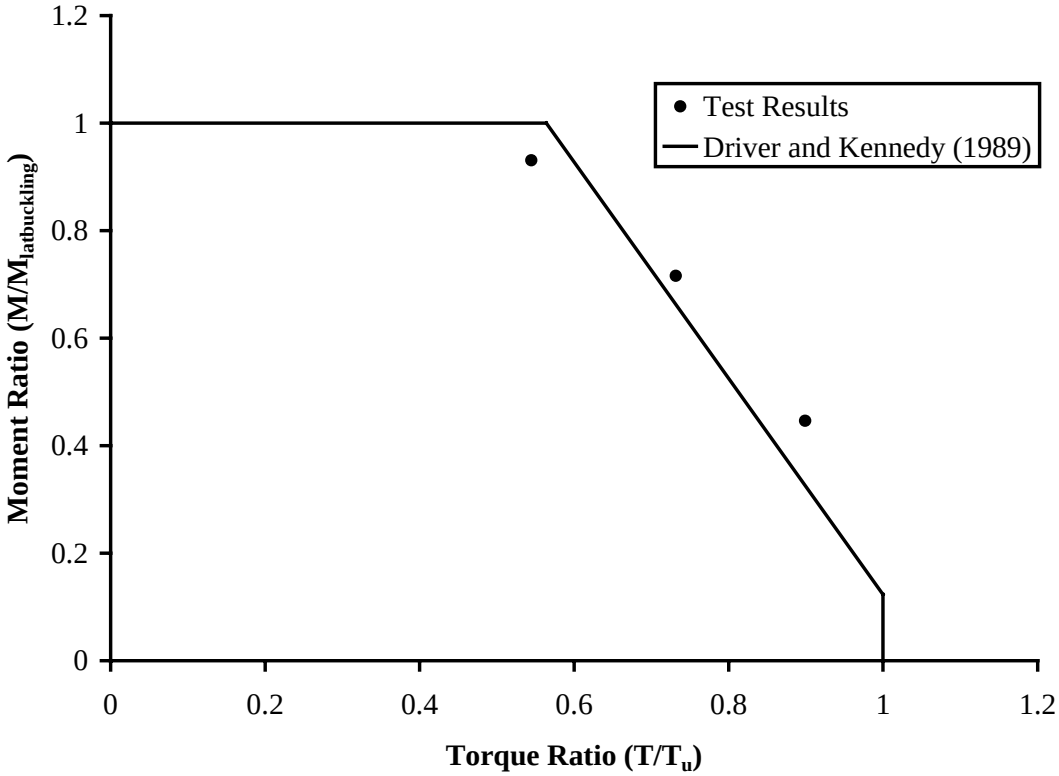

Figure 6.3 Comparison of test results to the Driver and Kennedy (1989) design method for Class 1 sections governed by lateral-torsional buckling

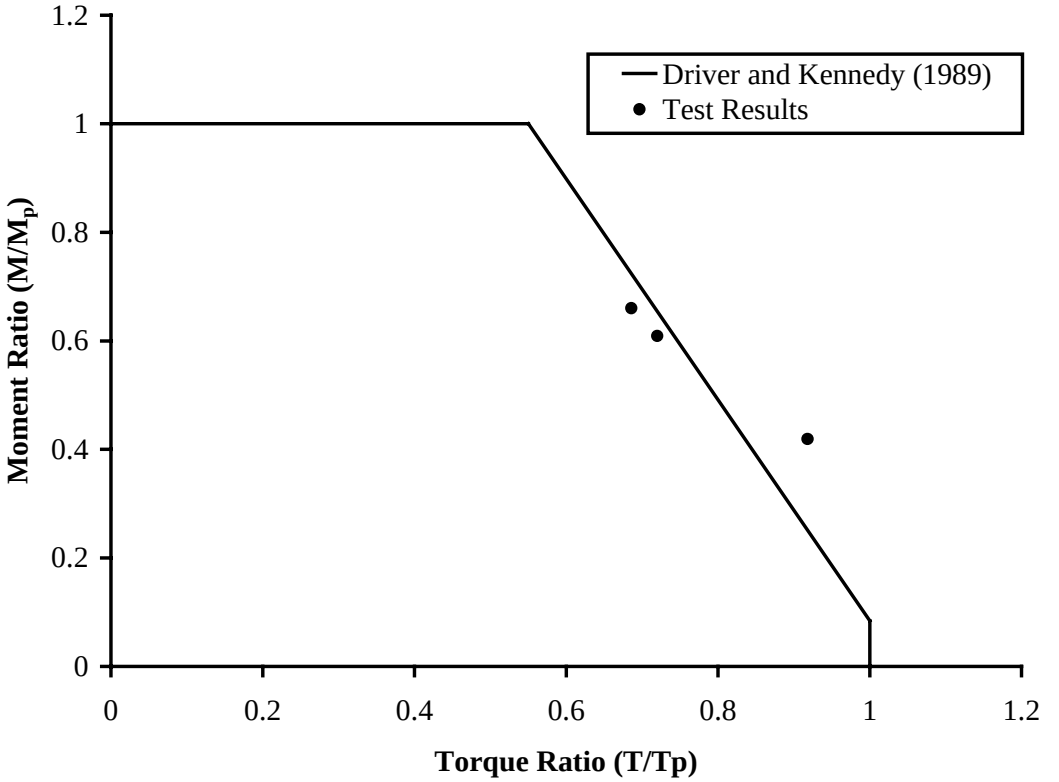

Figure 6.4 Comparison of test results to the Driver and Kennedy (1989) design method for Class 2 sections

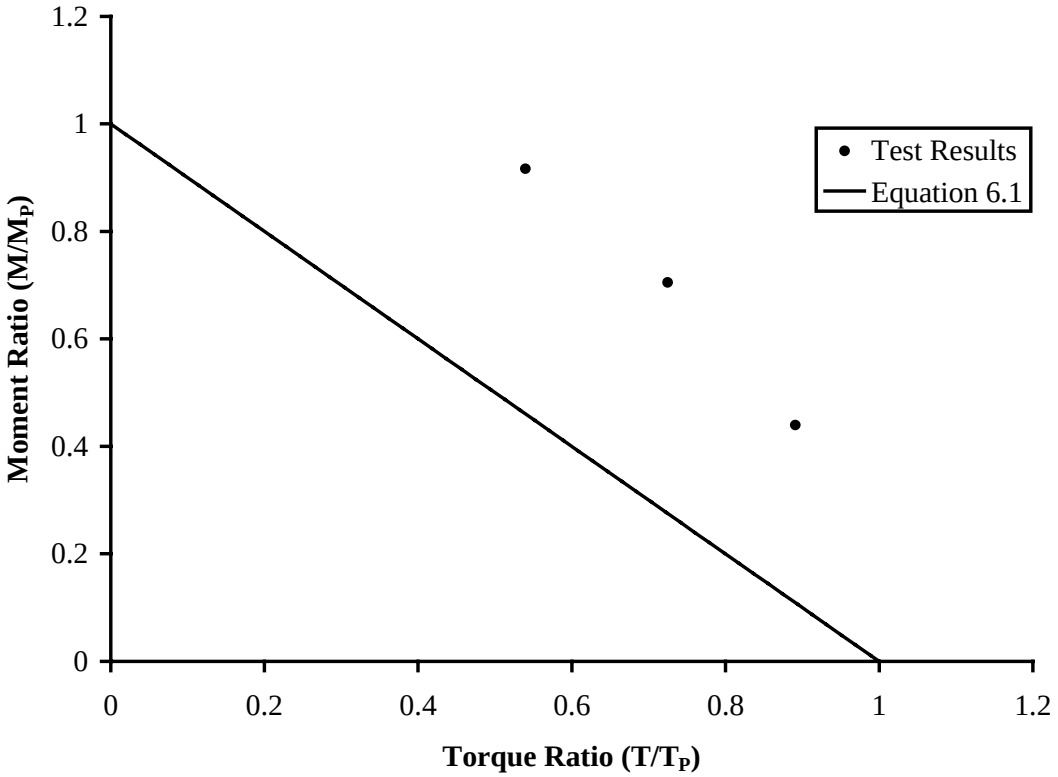

Figure 6.5 Comparison of test results to Pi and Trahair's linear interaction equation Class 1 specimens

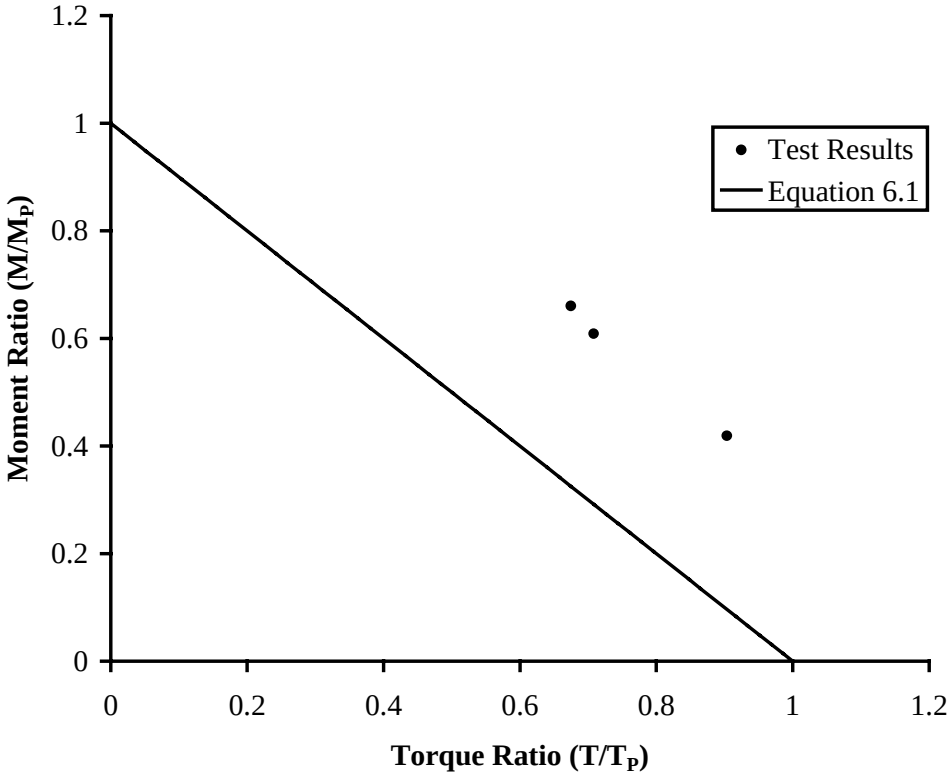

Figure 6.6 Comparison of test results to Pi and Trahair's linear interaction equation Class 2 specimens

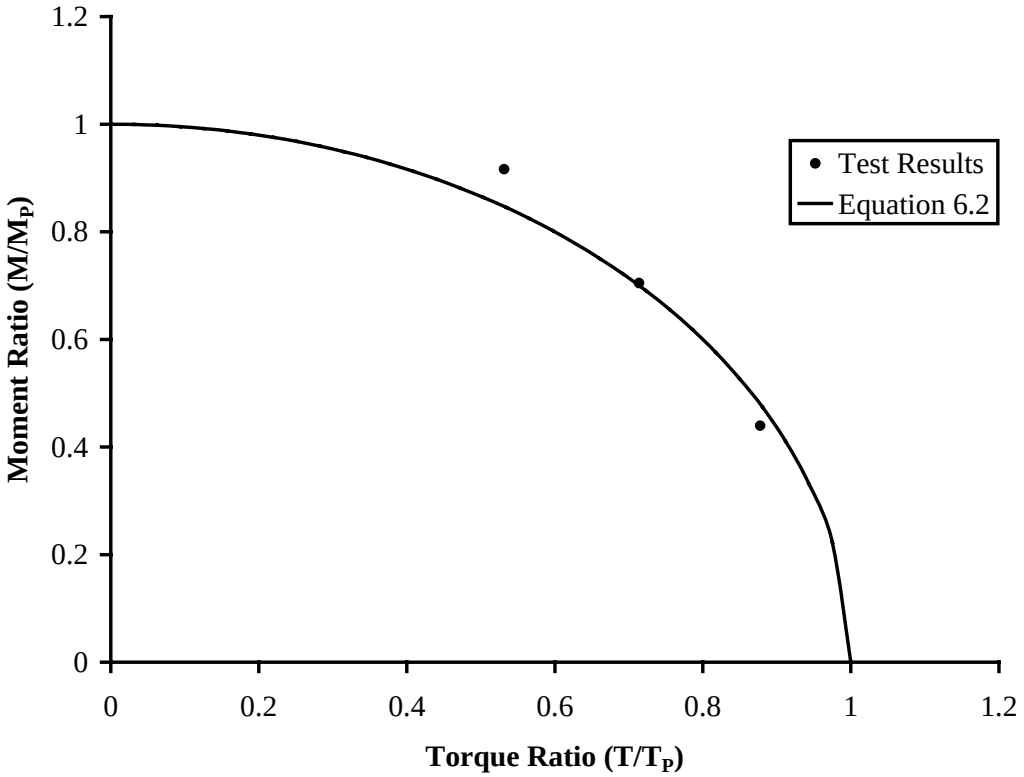

Figure 6.7 Comparison of Class 1 test results to Pi and Trahair's circular interaction equation based on plastic collapse

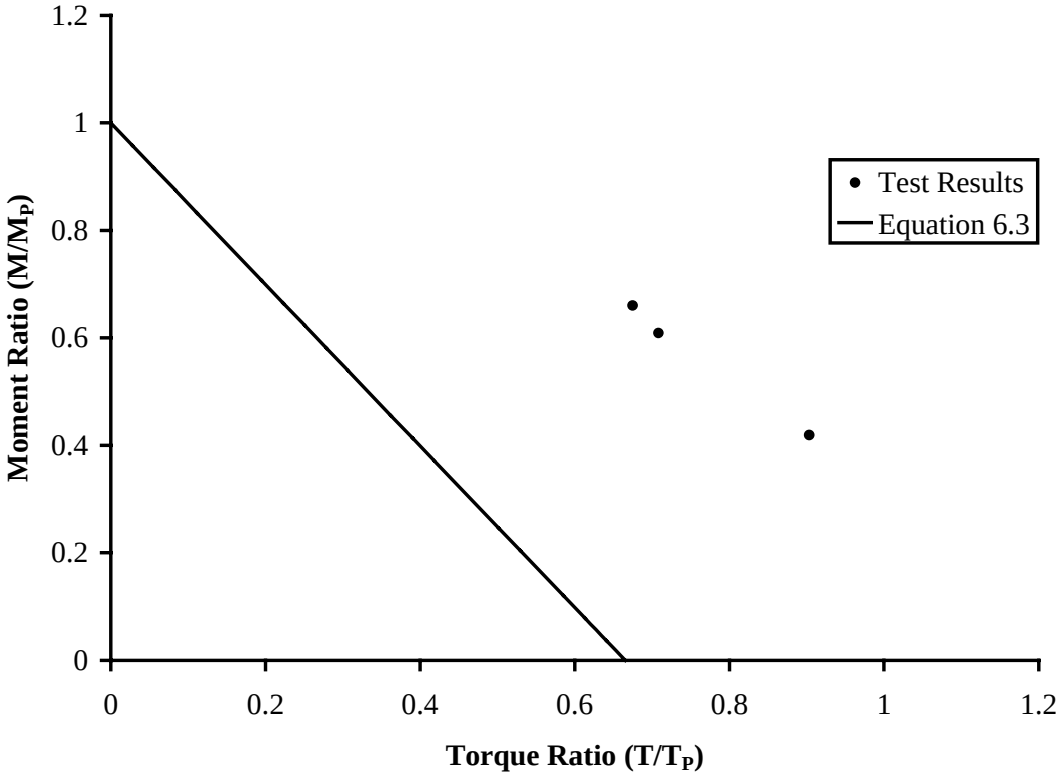

Figure 6.8 Comparison of test results to Pi and Trahair's linear interaction equation based on first hinge torsional design for Class 2 specimens

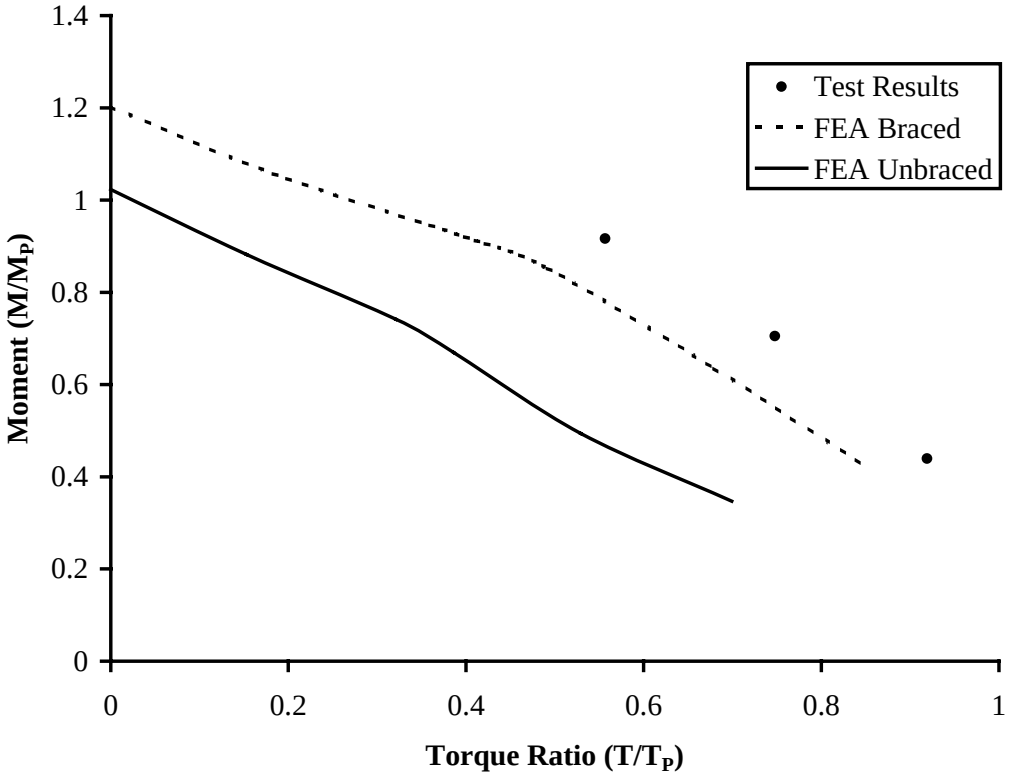

Figure 6.9 Comparison of finite element model to Class 1 test results

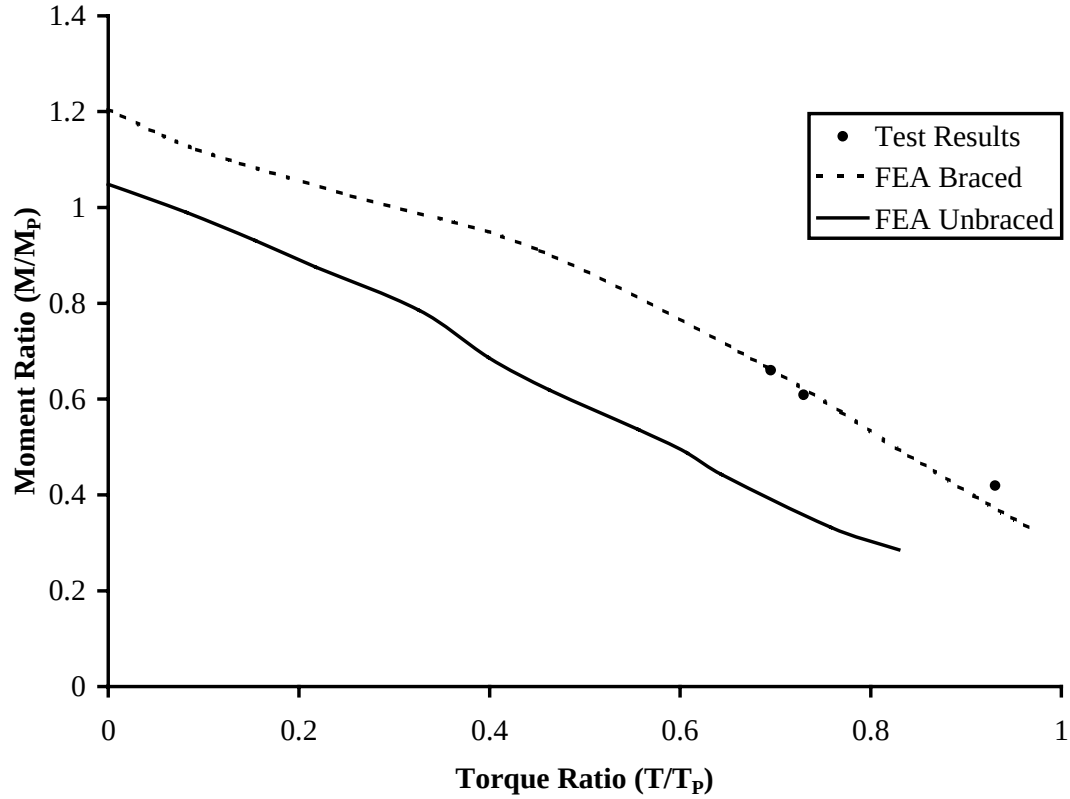

Figure 6.10 Comparison of finite element model to Class 2 test results

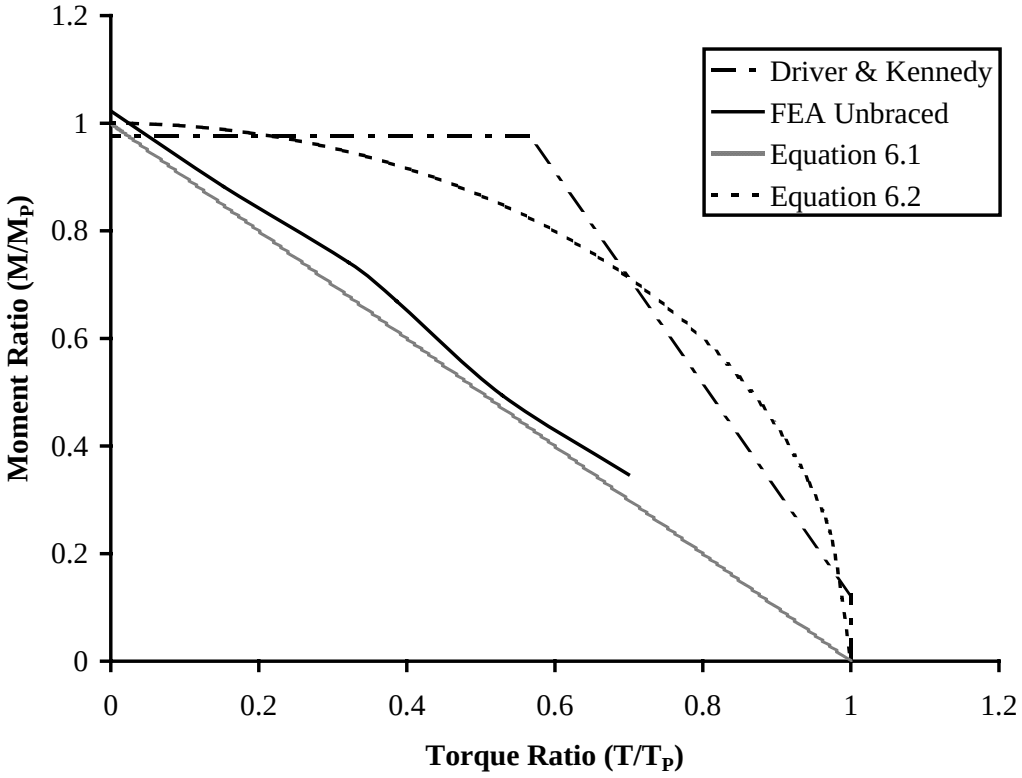

Figure 6.11 Comparison of interaction behavior predicted by the finite element model for the unbraced Class 1 beam to inelastic design curves

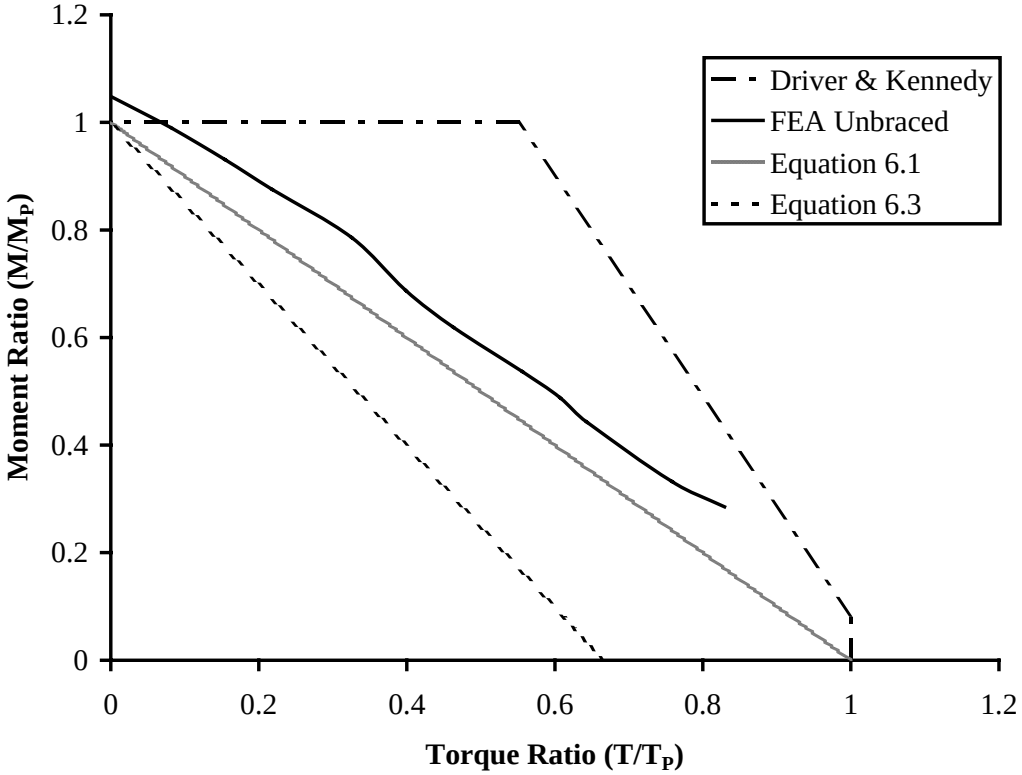

Figure 6.12 Comparison of interaction behavior predicted by the finite element model for the unbraced Class 2 beam to inelastic design curves

7. Conclusions

7.1 Summary and Conclusions

1. No limit states design approach has been adopted by the Canadian steel code to deal with combined bending and torsion.
2. Combined bending and torsion tests were performed on six simply supported I-shaped steel beams with varying moment-to-torque ratios.
3. A finite element model was developed using the finite element software ABAQUS. The initial linear response of the FEA model was in close agreement with the experimental elastic response, but underestimated the ultimate capacity of the tested beams.
4. Moment-torque interaction curves were developed using the FEA model for the tested beams.
5. The test results and finite element curves were compared to existing combined bending and torsion methods. Many of the inelastic design methods do not properly account for the destabilizing effects of torsion, warping stresses, nor bi-axial bending and are potentially non-conservative particularly at high moment-to-torque ratios.
6. A simplified design equation adopted from work done by Pi and Trahair (1993), has been proposed to deal with combined bending and torsion and appears to be a lower bound solution. In addition, the slenderness ratio proposed by Trahair and Bradford (1991) is identified as a potential means to quantify the slenderness of beams subjected to combined bending and torsion. A slenderness limit analogous to the slenderness limit used for members in compression could be established using Trahair and Bradford's ratio.

7.2 Recommendations for Future Research

An exhaustive parametric study fully investigating the influence of end conditions, loading conditions, slenderness and section class is required to confirm that

the proposed equation is a lower bound solution. Experimental programs are costly and finite element analysis has been shown to reasonably predict the response of beams subjected to combined bending and torsion and should be considered as a viable alternative. Such a parametric study would also be useful in establishing a slenderness limit beyond which beams could not be designed for combined bending and torsion.

7.3 Design Recommendations

At low moment-to-torque ratios beams will be highly distorted before they reach their inelastic capacity and designs will be governed by allowable rotations under service loads. At high moment-to-torque ratios interaction effects may cause the ultimate capacity of the beam under factored loads to govern design. The interaction equation proposed by Driver and Kennedy (1989) and referenced in the CSA S16-01 is potentially non-conservative and should not be used for ultimate limit states designs. Equation 6.4 proposed by Pi and Trahair (1993) is more suitable for ultimate limit states designs, but a complete parametric study is required before it can be confidently adopted by steel design codes.

List of References

American Institute of Steel Construction. 2005. Load and resistance factor design specification for structural steel buildings. AISC, Chicago, Illinois.

American Society for Testing and Materials. 2007. Standard Test Methods and Definitions for Mechanical Testing of Steel Products, ASTM A370-07a, ASTM International, West Conshohocken, Pa.

Boulton, N.S. 1962. Plastic twisting and bending of an I-beam in which the warp is Restricted. International Journal of Mechanical Sciences, **4**, 491-502.

Canadian Institute of Steel Construction. 2006. Handbook of steel construction 9th Ed. CISC, Willowdale, Ontario.

Canadian Standards Association. 2001. Limit States Design of Steel Structures, CAN/CSA-S16-01. CSA, Mississauga, Ontario.

Chu, K.H. and Johnson, R.B., 1974. Torsion in Beams with Open Sections. ASCE Journal of the Structural Division, **100**(ST7), 1397-1416

Dinno, K.S. and Merchant, W. 1965. A procedure for calculating the plastic collapse of I-sections under bending and torsion. The Structural Engineer, **43**(7), 219-221.

Driver, R.G., and Kennedy, D.J.L. 1989. Combined flexure and torsion of I-shaped steel beams. Canadian Journal of Civil Engineering, **16**(2): 124-139.

Driver, R.G., and Kennedy, D.J.L. 1987. Combined Flexure and Torsion of I-Shaped Steel Beams. Structural Engineering Report 144. University of Alberta.

Farwell, Jr., C. R. and Galambos, T.V. 1969. Nonuniform torsion of steel beams in inelastic range. ASCE Journal of the Structural Division, **95**(ST12), 2813-2829.

Galambos, T.V. 1968. Structural members and frames. Prentice-Hall International Inc., New York, N.Y.

Heins, C.P. 1975. Bending and torsional design in structural members. Lexington Books, Lexington, Massachusetts.

Heins, C.P., and Seaburg, P.A. 1963. Torsion analysis of rolled steel sections. Bethlehem Steel Corporation, Bethlehem, Pennsylvania.

Hodge, P.G. 1959. Plastic analysis of structures. McGraw-Hill Book Co., New York, NY.

Johnston, B.G. 1982. Design of W-shapes for combined bending and torsion. Engineering Journal of the AISC, **19**, 2nd quarter, 65-85.

Krayterman, B.L., and Krayterman, A. B. 1987. Generalized nonuniform torsion of beams and frames. ASCE Journal of Structural Engineering, **113**(8), 1772-1788.

Lin, P.H. 1977. Simplified design for torsional loading of rolled steel members. Engineering Journal of the AISC, 3rd quarter, 98-107.

Pi, Y.L., and Trahair, N. 1993a. Inelastic bending and torsion of steel I-beams. Research Report No. R683. The University of Sydney.

Pi, Y.L., and Trahair, N.S. 1993b. Inelastic torsion of steel I-beams. Research Report No. R679. The University of Sydney.

Pi, Y.L., and Trahair, N. 1994a. Plastic collapse analysis of torsion. Research Report No. R685. The University of Sydney.

Pi, Y.L., and Trahair, N. 1994b. Torsion and bending design of steel members. Research Report No. R686. The University of Sydney.

Pi, Y.L., and Trahair, N. 1994c. Inelastic bending and torsion of steel I-beams. ASCE Journal of Structural Engineering, **120**(12), 3397-3417.

Pi, Y.L., and Trahair, N. 1995a. Inelastic torsion of steel I-section beams. ASCE Journal of Structural Engineering, **121**(4), 609-620.

Pi, Y.L., and Trahair, N. 1995b. Plastic collapse analysis of torsion. ASCE Journal of Structural Engineering, **121**(10), 1389-1395.

Razzaq, Z. and Galambos, T.V. 1979a. Biaxial bending of beams with or without torsion. ASCE Journal of the Structural Division. **105**(ST 11), 2163-2185.

Razzaq, Z. and Galambos, T.V. 1979b. Biaxial bending tests with or without torsion. ASCE Journal of the Structural Division. **105**(ST 11), 2187-2202.

Salmon, C.G., and Johnson, J.E. 1997. Steel structures design and behavior. Pearson Education Toronto, pp. 371-393.

Trahair, N.S. 1993. Flexural-torsional buckling of structures. E &FN Spon, London.

Trahair, N.S., and Bradford, M.A. 1991. The behaviour and design of steel structures, Revised second edition, Chapman & Hall, London.

Trahair, N. and Pi, Y.L. 1997. Torsion, bending and buckling of steel beams. Engineering Structures, 19(5), 372-377.

Timoshenko, S.P., and Goodier, J.N. 1970. Theory of elasticity, Third edition. McGraw-Hill Book Co., Inc., New York, NY.

Appendix A

Results from Material Tests

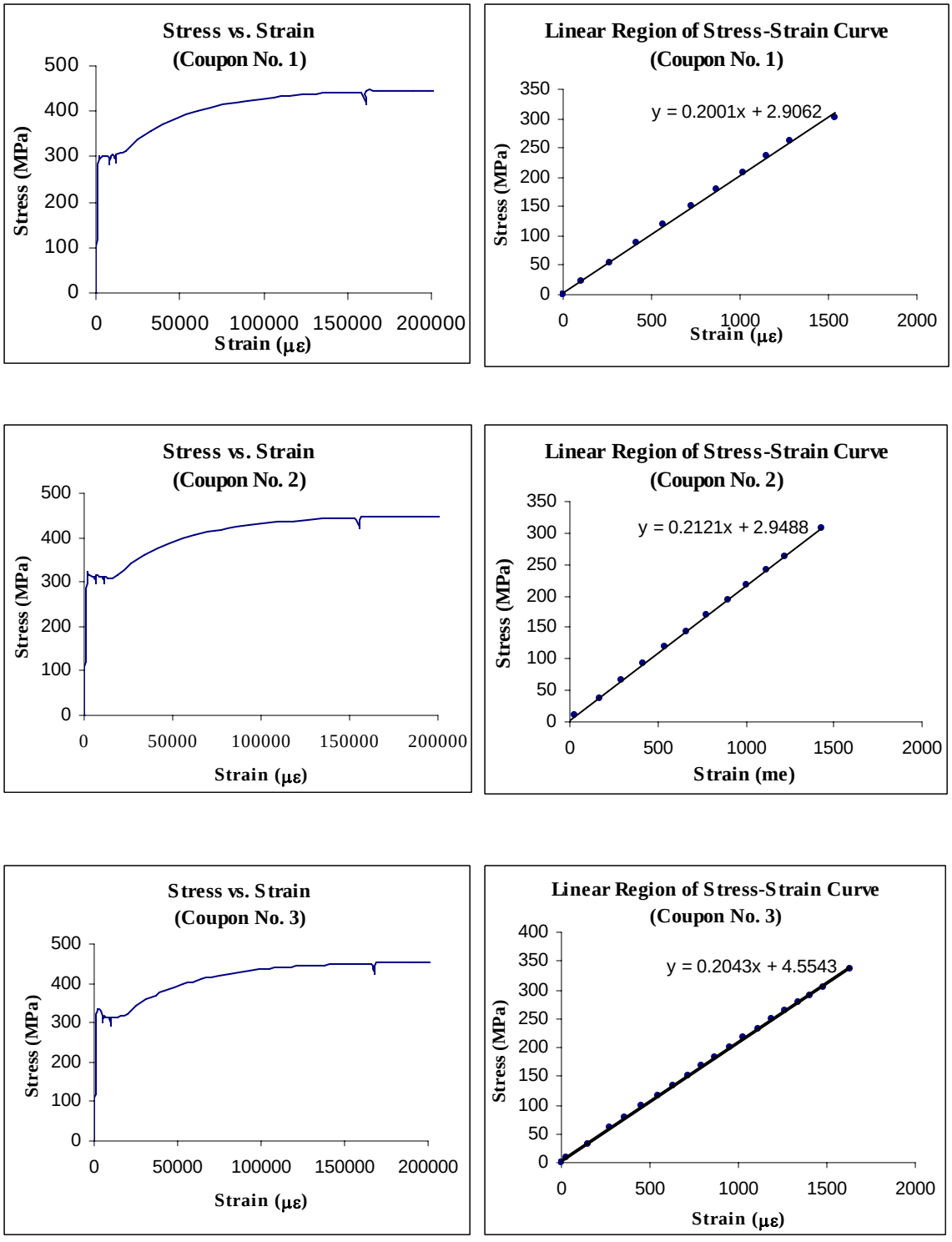

Figure A.1 Stress versus strain curves for the Class 1 coupon tests

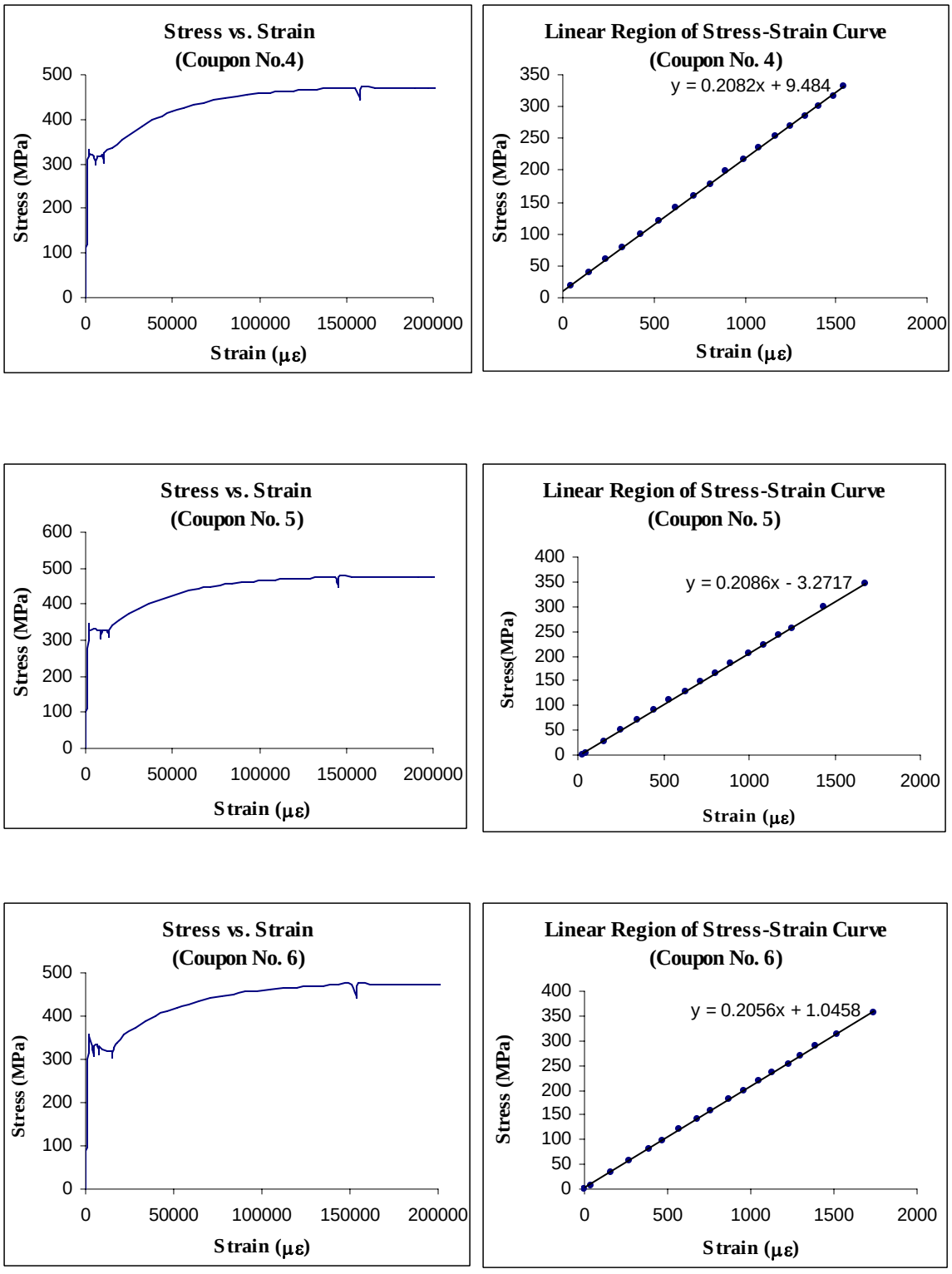

Figure A.2 Stress versus strain curves for the Class 2 coupon tests

Table A.1 Material properties of Class 1 coupons

Coupon No.	Modulus of elasticity (MPa)	Static yield stress (MPa)	Static ultimate stress (MPa)	Strain @ static ultimate stress (με)	Strain @ onset of strain hardening (με)
1	200100	284	416	161000	18000
2	212100	297	421	155000	19000
3	204300	297	423	168000	20000

Table A.2 Material properties of Class 2 coupons

Coupon No.	Modulus of elasticity (MPa)	Static yield stress (MPa)	Static ultimate stress (MPa)	Strain @ static ultimate stress (με)	Strain @ onset of strain hardening (με)
4	208200	300	442	158000	10500
5	208600	306	446	146000	15000
6	205600	307	444	154000	17000

Appendix B

Cross-Sectional Measurements and Properties

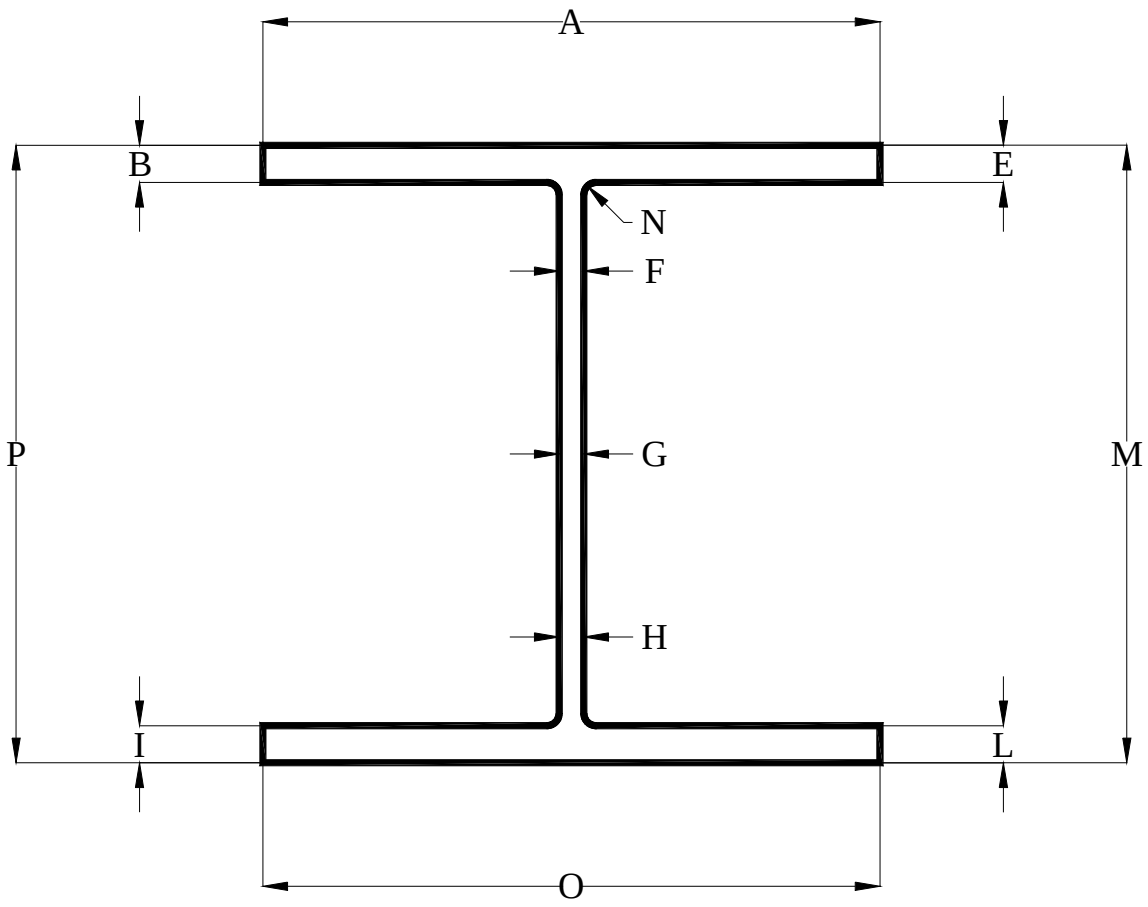

Figure B.1 Cross-section measurement locations

Table B.1 Cross-sectional measurements

Specimen No. & Designation	Location	A (mm)	B (mm)	E (mm)	F (mm)	G (mm)	H (mm)	I (mm)	L (mm)	M (mm)	N (mm)	O (mm)	P (mm)
	I	206	15.4	16.0	8.7	8.8	8.8	15.6	15.6	257	24	208	253
1	II	206	15.2	15.6	8.6	8.6	8.7	15.5	15.8	257		204	252
W250X67	III	206	15.2	15.7	8.6	8.6	8.7	15.6	15.3	256		205	252
	IV	206	15.2	15.6	8.6	8.6	8.7	15.5	15.7	256	23	204	253
	Avg.	206	15.2	15.6	8.6	8.6	8.7	15.6	15.7	256	23	204	253
	I	206	15.2	15.6	8.6	8.6	8.7	15.6	15.8	256	22	204	252
2	II	205	15.3	15.6	8.6	8.6	8.7	15.5	15.8	257		204	253
W250X67	III	206	15.2	15.5	8.6	8.6	8.7	15.5	15.7	256		204	253
	IV	206	15.3	15.7	8.6	8.6	8.7	15.6	15.8	257	23	204	252
	Avg.	205	15.2	15.6	8.6	8.6	8.7	15.6	15.8	257	22.5	204	253
	I	206	15.4	15.6	8.6	8.7	8.8	15.5	16.0	257	23	205	252
3	II	206	15.4	15.5	8.6	8.6	8.7	15.5	15.8	256		204	252
W250X67	III	206	15.3	15.5	8.6	8.6	8.7	15.5	15.9	257		204	252
	IV	206	15.3	15.5	8.5	8.6	8.6	15.5	16.0	257	22	205	252
	Avg.	206	15.3	15.5	8.6	8.6	8.7	15.5	15.9	257	22.5	204	252
	I	258	13.3	13.2	9.6	9.5	9.4	13.3	13.8	252	20	255	256
4	II	257	13.5	13.2				13.6	13.9	252		253	255
W250X73	III	257	13.3	13.2				13.4	13.9	252		254	255
	IV	257	13.5	13.2	9.6	9.5	9.4	13.4	13.9	252	20	254	255
	Avg.	257	13.4	13.2	9.6	9.5	9.4	13.4	13.9	252	20	254	255
	I	256	13.4	13.2	9.7	9.6	9.5	13.6	13.8	253	22	256	253
5	II	256	13.4	13.2				13.4	13.8	252		255	256
W250X73	III	256	13.4	13.2				13.4	13.8	252		254	255
	IV	257	13.4	13.1	9.7	9.6	9.5	13.2	13.7	252	24	254	255
	Avg.	256	13.4	13.2	9.7	9.6	9.5	13.4	13.8	252	23	255	255
	I	259	13.5	13.3	9.7	9.5	9.4	13.6	13.7	253	23	254	254
6	II	257	13.5	13.2	9.9	9.5	9.4	13.5	13.9	253		257	254
W250X73	III	257	13.4	13.1	9.9	9.4	9.4	13.4	13.9	252		256	253
	IV	258	13.4	13.2	9.7	9.5	9.4	13.5	13.9	252	21	256	255
	Avg.	258	13.4	13.2	9.8	9.5	9.4	13.5	13.8	253	22	256	254

Table B.2 Cross-sectional properties

Specimen No. & Designation	M_r (kN×m)	T_{up} (kN×m)	T_{wp} (kN×m)	M_p (kN×m)	M_y (kN×m)	M_{fp} (kN×m)	Z_x ($10^3 mm^3$)	S_x ($10^3 mm^3$)	I_x ($10^6 mm^4$)	I_y ($10^6 mm^4$)
T W250X67	254	9.80	5.41	260	231	48.4	874	778	99.3	22.3
U W250X67	254	9.76	5.40	270	231	48.4	908	779	99.6	22.3
V W250X67	254	9.76	5.41	260	232	48.4	874	781	99.8	22.3
1 W250X73	288	9.86	7.51	288	257	66.4	960	856	104	37.8
2 W250X73	287	9.90	7.51	287	256	66.4	957	854	104	37.8
3 W250X73	292	9.94	7.51	292	258	66.4	974	861	109	37.8

Appendix C

Calculations

C.1 First Yield Design

Limit the combined normal stress due to warping and bending to the yield stress of the material.

The normal stress due to bending is equal to:

$$\sigma_b = \frac{M_x}{S_x}$$

where, M_x is the strong axis bending moment,

and S_x is the elastic section modulus about the strong axis

The normal stress due to warping is equal to:

$$\sigma_w = -EW_n\phi''$$

where, E is the modulus of elasticity (211800MPa for the tested W250x67)

W_n is the normalized unit warping (12258mm^2 for the tested W250x67),

ϕ'' is the second derivative of the angle of twist with respect to the distance z, measured along the length of the member

The charts found in "Torsional Analysis of Structural Steel Members" by Seaburg (Case3 α=0.5) can be used to determine the answer to the following equation for the W250x67 Class 1 beams.

$$\phi'' \times \left(\frac{GJ}{T} \times a \right) = -0.465$$

where, G=77000MPa is shear modulus of elasticity,

J =625x10^3 mm^4 is the torsional constant for the cross-section,

T is the applied torque,

and a is a constant equal to:

$$a = \sqrt{\frac{EC_w}{GJ}} = \sqrt{\frac{211800 \times 324 \times 10^9}{77000 \times 625 \times 10^3}} = 1194mm$$

Solving for ϕ'',

$$\phi'' = -8.09 \times 10^{-15} \times T$$

Therefore,

$$\sigma_w = 8.09 \times 10^{-15} \times T \times 211800 \times 12258$$

$$\sigma_w = 2.1 \times 10^{-5} \times T$$

Solve the following first yield interaction equation:

$\sigma_b + \sigma_w = 1$

Table C.1 Solutions to the first yield interaction equation

1st Yield					
T	**M**	**T/Tp**	**M/Mp**	**σ_b**	**σ_w**
0.00	231.36	0.00	1.00	297	0
0.70	220.00	0.05	0.95	282.41	14.58665
1.93	200.00	0.14	0.86	256.74	40.26059
3.16	180.00	0.22	0.78	231.07	65.93453
4.39	160.00	0.31	0.69	205.39	91.60847
5.62	140.00	0.39	0.61	179.72	117.2824
6.85	120.00	0.48	0.52	154.04	142.9564
8.08	100.00	0.57	0.43	128.37	168.6303
9.31	80.00	0.65	0.35	102.70	194.3042
10.54	60.00	0.74	0.26	77.02	219.9782
11.77	40.00	0.83	0.17	51.35	245.6521
13.00	20.00	0.91	0.09	25.67	271.3261
14.23	0.00	1.00	0.00	0.00	297

C.2 First Yield Design with AISC LRFD Reduction Factor

Multiply the torque calculated using the first yield design by the following reduction factor:

$$\left(\frac{f_y}{f_y - \sigma_b} \right)$$

Table C.2 Solutions to first yield interaction equation with LRFD Reduction Factor

AISC LRFD Reduction Factor						
T	**M**	**T/Tp**	**M/Mp**	**σ_b**	**σ_w**	**(F_y/(F_y - σ_b)**
0.00	231.36	0.00	1.00	297	0	1.00E+99
0.03	220.00	0.00	0.95	282.41	0.716398468	20.36108422
0.26	200.00	0.02	0.86	256.74	5.457626759	7.376940981
0.70	180.00	0.05	0.78	231.07	14.63758397	4.504468197
1.35	160.00	0.09	0.69	205.39	28.25627009	3.242058209
2.22	140.00	0.16	0.61	179.72	46.31368512	2.532348982
3.29	120.00	0.23	0.52	154.04	68.80982907	2.077557178
4.58	100.00	0.32	0.43	128.37	95.74470194	1.761249362
6.08	80.00	0.43	0.35	102.70	127.1183037	1.528530751
7.79	60.00	0.55	0.26	77.02	162.9306344	1.350133926
9.72	40.00	0.68	0.17	51.35	203.181694	1.209026823
11.85	20.00	0.83	0.09	25.67	247.8714826	1.094623941
14.20	0.00	1.00	0.00	0.00	297	1

C.3 Driver and Kennedy

The compression flange of the W250x67 is unbraced and the moment resistance is governed by lateral-torsional buckling.

$$M_r = 1.15M_p \times \left(1 - \frac{0.28M_p}{M_u}\right)$$

$$M_u = \frac{\omega_2 \pi}{L} \times \sqrt{EI_y GJ + \left(\frac{\pi E}{L}\right)^2 I_y C_w}$$

$$M_u = \frac{1.0 \cdot \pi}{4000} \sqrt{211800 \cdot 22.2 \times 10^6 \cdot 77000 \cdot 625 \times 10^3 + \left(\frac{\pi \cdot 211800}{4000}\right)^2 \cdot 22.2 \times 10^6 \cdot 324 \times 10^9}$$

$$M_u = 512 kN \cdot m$$

$$M_r = 1.15 \times 263 \times \left(1 - \frac{0.28 \times 263}{512}\right)$$

$$M_r = 259 kN \cdot m$$

The Driver and Kennedy interaction diagram assumes that no reduction in moment carrying capacity will occur until the uniform plastic torque is exceeded.

Calculate the uniform plastic torque

$$T_{up} = \tau_y \left[bt^2 \left(1 - \frac{t}{3b}\right) + \frac{hw^2}{2} + \frac{w^3}{6} \right]$$

where, τ_y is the shear yield strength of the material,

b and t are the width and thickness of the flanges, respectively,

w is the web thickness,

and *h* is the clear distance between the flanges.

For the tested W250x67 Class 1 section,

$$T_{up} = \frac{297}{\sqrt{3}} \left[205 \times 15.5^2 \left(1 - \frac{15.5}{3 \times 205}\right) + \frac{239 \times 8.6^2}{2} + \frac{8.6^3}{6} \right]$$

$$T_{up} = 9.72 kN \cdot m$$

The Driver and Kennedy interaction diagram for Class 1 sections governed by lateral-torsional buckling assumes that the maximum torque that can be resisted by the beam is equal to the plastic torque capacity of the section.

Calculate the warping plastic torque.

$$T_{wp} = \frac{2 \times M_{fp} \times h}{L}$$

where, h is the height between flange centroids,

L is the span of the beam,

and M_{fp} is the flange plastic moment of the beam equal to:

$$M_{fp} = \frac{f_y \times b^2 \times t}{4}$$

For the tested W250x67 Class 1 section,

$$M_{fp} = \frac{297 \times 205^2 \times 15.5}{4}$$

$$M_{fp} = 48.4 kN \cdot m$$

therefore,

$$T_{wp} = \frac{2 \times 48.4 \times 0.239}{4}$$

$$T_{wp} = 5.79 kN \cdot m$$

Now calculate the combined plastic torque capacity of the section.

$$T_p = T_{wp} + T_{up}$$

$$T_p = 5.79 + 9.72$$

$$T_p = 15.5 kN \cdot m$$

The model assumes no reduction in torque carrying capacity will occur until the moment exceeds the plastic web moment, where the plastic web moment is expressed as:

$$M_{pweb} = f_y \times \frac{wh^2}{4} = 297 \times \frac{8.6 \times 239^2}{4} = 31.9 kN \cdot m$$

Table C.3 Driver and Kennedy interaction equation for W250x67 governed by lateral-torsional buckling

Driver and Kennedy			
T	**M**	**T/T_p**	**M/M_r**
15.52	0	1	0
15.52	31.9255588	1	0.12328049
9.72285509	258.966834	0.56397266	1
0	258.966834	0	1

C.4 Pi and Trahair's Linear Interaction Equation

For a simply supported I-shaped beam centrally braced at the shear center:

$$\left(\frac{PL}{4M_r}\right)+\left(\frac{Pe}{2T_p}\right)=1$$

where, P is the applied vertical load at midspan,

L is the span of the beam,

e is the eccentricity of the point load relative to the shear center of the beam,

M_r is the moment resistance of the beam,

and T_p is the plastic torsion capacity of the beam

For the tested W250x67 Class 1 section - braced,

$$M_r = M_p = Z_x \times f_y$$

$$M_r = 0.885 \times 297$$

$$M_r = 263 kN \cdot m$$

$$T_p = T_{wp} + T_{up}$$

where T_{wp} is the warping plastic torque,

and T_{up} is the uniform plastic torque.

$$T_{wp} = \frac{2 \times M_{fp} \times h}{L}$$

where, h is the height between flange centroids,

L is the span of the beam,

and M_{fp} is the flange plastic moment of the beam equal to:

$$M_{fp} = \frac{f_y \times b^2 \times t}{4}$$

For the tested W250x67 Class 1 section,

$$M_{fp} = \frac{297 \times 205^2 \times 15.5}{4}$$

$$M_{fp} = 48.4 kN \cdot m$$

therefore,

$$T_{wp} = \frac{2 \times 48.4 \times 0.239}{4}$$

$$T_{wp} = 5.79kN \cdot m$$

$$T_{up} = \tau_y \left[bt^2 \left(1 - \frac{t}{3b} \right) + \frac{hw^2}{2} + \frac{w^3}{6} \right]$$

where, τ_y is the shear yield strength of the material,

b and t are the width and thickness of the flanges, respectively,

w is the web thickness,

and *h* is the clear distance between the flanges.

For the tested W250x67 Class 1 section,

$$T_{up} = \frac{297}{\sqrt{3}} \left[205 \times 15.5^2 \left(1 - \frac{15.5}{3 \times 205} \right) + \frac{239 \times 8.6^2}{2} + \frac{8.6^3}{6} \right]$$

$$T_{up} = 9.72kN \cdot m$$

Therefore,

$$T_p = 5.79 + 9.72$$

$$T_p = 15.5kN \cdot m$$

Rewrite the linear interaction equation as follows and solve.

$$\left(\frac{M_{applied}}{M_r} \right) + \left(\frac{T_{applied}}{2T_p} \right) = 1$$

Table C.4 Solutions to Pi and Trahair's linear interaction equation

W250 x 67				
$\mathbf{M_{applied}}$	$\mathbf{T_{applied}}$	$\mathbf{M_{applied}/M_p}$	$\mathbf{T_{applied}/(2T_p)}$	$\mathbf{M_{applied}/M_p + T_{applied}/T_p}$
0	30.97	0.00	1.00	1.00
20	28.62	0.08	0.92	1.00
40	26.26	0.15	0.85	1.00
60	23.91	0.23	0.77	1.00
80	21.55	0.30	0.70	1.00
100	19.20	0.38	0.62	1.00
120	16.84	0.46	0.54	1.00
140	14.49	0.53	0.47	1.00
160	12.13	0.61	0.39	1.00
180	9.77	0.68	0.32	1.00
200	7.42	0.76	0.24	1.00
220	5.06	0.84	0.16	1.00
240	2.71	0.91	0.09	1.00
260	0.35	0.99	0.01	1.00
263	0.00	1.00	0.00	1.00

C.5 Pi and Trahair's Circular Interaction Curve for Plastic Collapse

$$\lambda_{ip}^{\ 2} + \lambda_{tp}^{\ 2} \leq 1$$

where, λ_{ip} is the plastic collapse load factor for in-plane bending, and

λ_{tp} is the plastic collapse load factor for torsion.

The plastic collapse load factor for torsion is equal to the sum of the independent plastic load factors for uniform torsion collapse and warping torsion collapse.

$$\lambda_{tp} = \lambda_{up} + \lambda_{wp}$$

For a beam with a concentrated torque at midspan and pinned torsional restraints the critical applied torque required to cause plastic collapse due to uniform torsion is:

$$T_{upc} = 2 \times T_{up}$$

where, T_{up} is the uniform plastic torque equal to:

$$T_{up} = \tau_y \left[bt^2 \left(1 - \frac{t}{3b} \right) + \frac{hw^2}{2} + \frac{w^3}{6} \right]$$

where, τ_y is the shear yield strength of the material,

b and t are the width and thickness of the flanges, respectively,

w is the web thickness,

and h is the clear distance between the flanges.

For the tested W250x67 Class 1 section,

$$T_{up} = \frac{297}{\sqrt{3}} \left[205 \times 15.5^2 \left(1 - \frac{15.5}{3 \times 205} \right) + \frac{239 \times 8.6^2}{2} + \frac{8.6^3}{6} \right]$$

$$T_{up} = 9.77 kN \cdot m$$

Therefore,

$$T_{upc} = 2 \times 9.77$$

$$T_{upc} = 19.5 kN \cdot m$$

The critical applied torque required to cause warping torsion plastic collapse for a torsionally pinned beam with a concentrated torque at midspan is equal to:

$$T_{wpc} = \frac{4 \times M_{fp} \times h}{L}$$

where, M_{fp} is the flange plastic moment of the beam equal to:

$$M_{fp} = \frac{f_y \times b^2 \times t}{4}$$

For the tested W250x67 Class 1 section,

$$M_{fp} = \frac{297 \times 205^2 \times 15.5}{4}$$

$$M_{fp} = 48.4 kN \cdot m$$

therefore,

$$T_{wpc} = \frac{4 \times 48.4 \times 0.239}{4}$$

$$T_{wpc} = 11.6 kN \cdot m$$

The critical applied bending moment required to cause the bending plastic collapse of a simply supported beam with a concentrated load at midspan is equal to:

$$M_{ipc} = M_p$$

For the tested W250x67 Class 1 section,

$$M_{ipc} = Z_x \times f_y$$

$$M_{ipc} = 0.885 \times 297$$

$$M_{ipc} = 263 kN \cdot m$$

For,

$$\lambda_{up} = \frac{T_{applied}}{T_{upc}},\ \lambda_{wp} = \frac{T_{applied}}{T_{wpc}}, \text{ and } \lambda_{tp} = \lambda_{up} + \lambda_{wp} \leq 1$$

and

$$\lambda_{ip} = \frac{M_{applied}}{M_{ipc}}$$

Solve the circular plastic collapse interaction curve.

$$\lambda_{ip}^{\ 2} + \lambda_{tp}^{\ 2} = 1$$

Table C.5 Solutions to Pi and Trahair's plastic collapse circular interaction curve

W250 X 67						
T (kNxm)	**M (kNxm)**	**(T/T_p)**	**(M/M_p)**	**λ_{tp}**	**λ_{ip}**	**$\lambda_{ip}^2+\lambda_{tp}^2$**
0.00	263.00	0.00	1.00	0.00	1.00	1.00
5.00	259.41	0.16	0.99	0.16	0.99	1.00
10.00	248.32	0.33	0.94	0.33	0.94	1.00
15.00	228.64	0.49	0.87	0.49	0.87	1.00
20.00	197.83	0.66	0.75	0.66	0.75	1.00
25.00	149.15	0.82	0.57	0.82	0.57	1.00
30.00	39.97	0.99	0.15	0.99	0.15	1.00
30.35	0.00	1.00	0.00	1.00	0.00	1.00